CMS Draft Analysis Note

2024/11/11
Archive Hash: untracked
Archive Date: 2024/11/11

Search for W_R boson decaying into a heavy neutral lepton in a $\tau_h\tau_l$ + jets final state

Youngwan Kim*[,1], Sihyun Jeon[2], John Leslie Almond[1], and Un-ki Yang[1]

[1] Seoul National University
[2] Boston University
*Primary author

Abstract

A search is presented for a right-handed W boson (W_R) and a heavy neutrino (N), in a final state consisting of a lepton (e or μ) from a leptonic tau (τ_l) accompanied by a hadronic tau (τ_h) and two quarks. The search is performed with the CMS experiment at the CERN LHC using a data sample of proton-proton collisions at a center-of-mass energy of 13 TeV corresponding to an integrated luminosity of 138 fb^{-1}.

0 Notes

0.1 v5:9-Sep-2024

- Details of JECs are included.
- Add new plots and event selections for the fake control region.

0.2 v4:9-Sep-2024

- Tau object and systematic definitions are made more clear.
- Nonprompt hadronic tau data-driven estimation method is updated.
- Included major systematic sources and made input to corresponding section of the AN.

0.3 v3:7-AUG-2024

- Extended and fixed content in previously edited sections.

0.4 v2:30-JAN-2023

- Updated sections 1, 2

0.5 v1:10-JAN-2023

Initiation of AN-23-001.

Contents

1 Introduction

Several experimental results have provided a solid observation for parity violation in the standard model (SM) weak interactions, which is inexplicable in the bounds of SM itself. Various extensions of the SM have been introduced to spell out such unaccountable observations, and one of them is the Left-right symmetric model (LRSM) [1–4] which extends the SM electroweak sector by a right-handed SU(2) group. Such an extension can explain the observed parity violation by allowing a spontaneous symmetry breaking in a scale of TeV order.

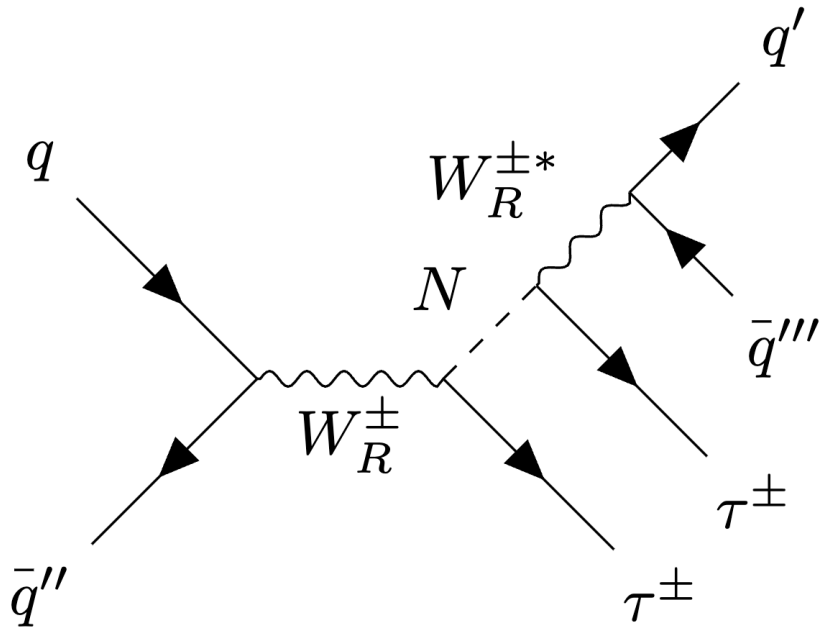

Figure 1: Feynman diagram for the production of N from a W_R decay.

In this study, the production of the right-handed W boson (W_R) subsequently decaying into a tau lepton (τ_{pri}) and a heavy neutral lepton N is the process of interest. The N again decays into an off-shell W_R and a tau lepton (τ_{sec}) with the same flavor as the first lepton: the virtual W_R decays hadronically, essentially a three-body decay. The Feynman diagram for such a process is depicted in Fig.1. Here, the channel of interest will be the one where τ_{pri} decays hadronically and τ_{sec} leptonically, leading to a light lepton and a hadronic tau (τ_h) with jets from the off-shell W_R as the final state.

Several studies have been performed in CMS targeting the same channel of interest with the same model hypothesis. The most recent study has excluded W_R masses below 3.52 (2.75) TeV at 95% confidence level, assuming the N mass is 0.8 (0.2) times the mass of the W_R boson using the 2016 data corresponding to an integrated luminosity of 35.9 fb^{-1} [5]. This analysis mainly targets to improve the limits on the phase space where the mass of W_R is way larger than the mass of N which was not fully excluded in the mentioned previous study. The mass hypothesis is set to range from 1 TeV to 6.5 TeV and 100 GeV to $m_{W_R} - 100$ GeV respectively for W_R and N. Also an assumption that the coupling strength of W_R with the SM particles g_R, is the same as the SM coupling constant g_L.

2 Dataset

2.1 Data Samples

This analysis uses proton-proton (pp) collisions in the LHC, recorded by the CMS detector at $\sqrt{s} = 13\,\text{TeV}$ during Run-II, with an integrated luminosity of $137.4\,\text{fb}^{-1}$. The data collected in 2016 is split into two eras with different conditions, mainly due to the APV readout chip condition alteration between those eras. The dataset produced in 2016 before such modification is denoted as "preVFP" and for the vice versa condition as "postVFP", corresponding to an integrated luminosity of $19.50\,\text{fb}^{-1}$ and $16.81\,\text{fb}^{-1}$ respectively, resulting in $36.31\,\text{fb}^{-1}$ in total in 2016. Luminosity information for each era with the run information is shown in Table 1 alongside the tau dataset used in this analysis, aiming for the desired $e\tau_h$ and $\mu\tau_h$ channel of interest of this search. The following golden JSON files were used to select the lumi sections when all subdetectors were operational during recording :

- 2016 : `Cert_271036-284044_13TeV_Legacy2016_Collisions16_JSON.txt`
- 2017 : `Cert_294927-306462_13TeV_UL2017_Collisions17_GoldenJSON.txt`
- 2018 : `Cert_314472-325175_13TeV_Legacy2018_Collisions18_JSON.txt`

Table 1: Tau Dataset

Dataset Name	Run Range
2016preVFP	**19.50fb^{-1}**
/Tau/Run2016B-ver2_HIPM_UL2016_MiniAODv2-v1/MINIAOD	273150 – 275376
/Tau/Run2016C-HIPM_UL2016_MiniAODv2-v1/MINIAOD	275656 – 276283
/Tau/Run2016D-HIPM_UL2016_MiniAODv2-v1/MINIAOD	276315 – 276811
/Tau/Run2016E-HIPM_UL2016_MiniAODv2-v1/MINIAOD	276831 – 277420
/Tau/Run2016F-HIPM_UL2016_MiniAODv2-v1/MINIAOD	277932 – 278770
2016postVFP	**16.81fb^{-1}**
/Tau/Run2016F-UL2016_MiniAODv2-v1/MINIAOD	278769 – 278808
/Tau/Run2016G-UL2016_MiniAODv2-v1/MINIAOD	278820 – 280385
/Tau/Run2016H-UL2016_MiniAODv2-v1/MINIAOD	281613 – 284044
2017	**41.48fb^{-1}**
/Tau/Run2017B-UL2017_MiniAODv2-v1/MINIAOD	297047 – 299329
/Tau/Run2017C-UL2017_MiniAODv2-v1/MINIAOD	299368 – 302029
/Tau/Run2017D-UL2017_MiniAODv2-v1/MINIAOD	302031 – 302663
/Tau/Run2017E-UL2017_MiniAODv2-v1/MINIAOD	303824 – 304797
/Tau/Run2017F-UL2017_MiniAODv2-v1/MINIAOD	305040 – 306460
2018	**59.83fb^{-1}**
/Tau/Run2018A-UL2018_MiniAODv2-v1/MINIAOD	315257 – 316995
/Tau/Run2018B-UL2018_MiniAODv2-v1/MINIAOD	317080 – 319310
/Tau/Run2018C-UL2018_MiniAODv2-v1/MINIAOD	319337 – 320065
/Tau/Run2018D-UL2018_MiniAODv2-v2/MINIAOD	320500 – 325175

2.2 Signal Samples

The signal samples are generated using MADGRAPH at leading order (LO) [6] for the $\tau\tau$ channel process. The LRSM model `EffLRSM_NLO` [7] was included for the generation in MADGRAPH as an external model, with different W_R and N mass values as input parameters. Samples were generated with m_{W_R} ranging from 1 TeV to 6.5 TeV, and m_N from 100 GeV to $m_{W_R} - 100\,\text{GeV}$ with

an increment of 500 GeV and 100 GeV respectively. Fig.2 shows the calculated cross section of each generated samples in the (m_{W_R}, m_N) plane. The sample names and the corresponding values of cross sections can be found in Appendix A.1.

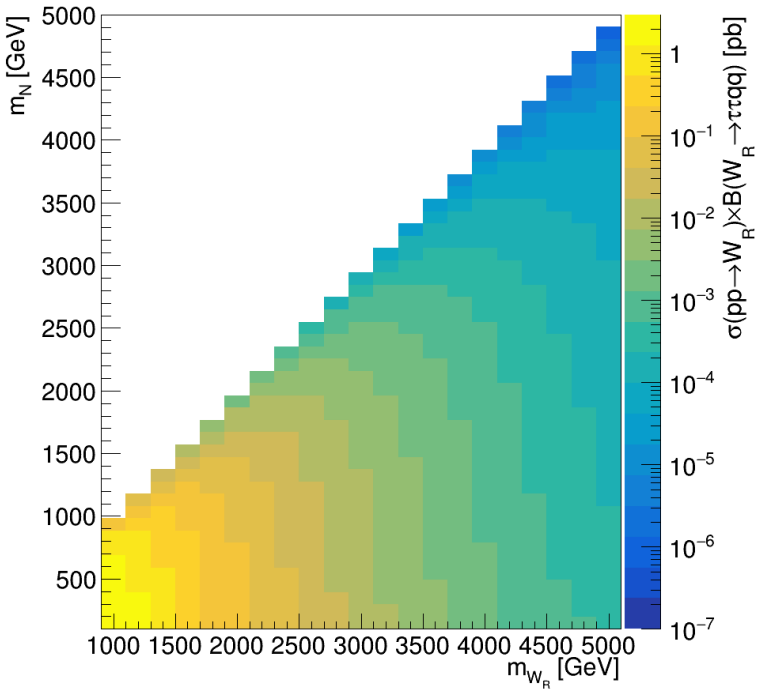

Figure 2: Signal sample cross sections in pb, of produced $pp \to \tau N \to \tau\tau jj$ in the (m_{W_R}, m_N) plane.

An additional LHE level filter was used to filter out events where both taus decay hadronically, thus only allowing two leptonic taus or a leptonic tau with a hadronic tau as the LHE level final state taus. PYTHIA 8.2 [8] was used to simulate parton showering and fragmentation, where the PYTHIA parameters having direct effect with underlying events are tuned with the CP5 tune [9]. NNPDF 3.1 [10–12] is used for the parton density function (PDF). After generator-level simulations, the events go through GEANT4 [13] to simulate the CMS detector properly. All samples were produced up to the MINIAODSIM level, which follows the CMS Run2 ultra legacy campaigns per era, listed in Table 2.

Table 2: Run2 ultra legacy (UL) MINIAODSIM production campaigns for each eras.

Era	MINIAOD Campaign
2016preVFP	`RunIISummer20UL16MiniAODAPVv2-106X_mcRun2_asymptotic_preVFP_v11-v1`
2016postVFP	`RunIISummer20UL16MiniAODv2-106X_mcRun2_asymptotic_v17-v1`
2017	`RunIISummer20UL17MiniAODv2-106X_mc2017_realistic_v9-v1`
2018	`RunIISummer20UL18MiniAODv2-106X_upgrade2018_realistic_v16_L1v1-v1`

Some of the generator-level kinematic distributions, such as the transverse momentum (p_T), pseudorapidity (η) and invariant masses were studied and plotted in Fig.3–5 for the scenario $m_{W_R} = 2$ TeV with $m_N = 100$ GeV, $m_{W_R}/2$ and $m_{W_R} - 100$ GeV as a validation of the sample production process. Plots for other mass points, i.e., $m_{W_R} = 1, 4$ TeV are shown in Appendix A.2. Only the $\tau\tau$ events were selected among all of the available $\ell\ell$ channels, thus having a preselection requiring exactly two τ leptons where the primary (secondary) τ from $W_R(N)$

will be denoted as $\tau_{pri}(\tau_{sec})$ within the "resolved" topology described in the below list. Being able to distinguish between the primary and secondary lepton in the generator level helps to reconstruct the sum of $\tau_{\text{pri}}\tau_{\text{sec}}jj$ and $\tau_{\text{sec}}jj$ which will act as a proxy of W_R and N respectively.

- At least 2 AK4 jets (j), which are cleaned using leptons and taus.
- $\min\Delta R(\tau, j) > 0.4$ for all τ and jets.

Otherwise, events failing the resolved selection but having at least one AK8 jet (J) and $\Delta R(\tau, J) < 0.8$ for any τ, are included in the "boosted" signal region. Further description of the signal and control region cuts will be dealt with in Section 6.

Table 3: Selection efficiency for selected signal sample mass scenarios. $\tau\tau$ denotes the preselection of selecting exactly two final state τ leptons. The resolved and boosted regions are selected after the preselection. All efficiencies listed are calculated by comparing the number of events with no selections.

Mass Points		Selection Efficiency		
m_{W_R} (GeV)	m_N (GeV)	$\tau_\mu\tau_h$	Resolved	Boosted
1000	100	7.58%	0.03%	7.38%
1000	200	7.70%	0.12%	7.35%
1000	500	9.07%	1.09%	7.40%
1000	900	5.98%	1.83%	3.26%
2000	100	12.02%	0.02%	11.90%
2000	400	12.97%	0.34%	12.42%
2000	1000	15.19%	2.71%	11.93%
2000	1900	10.51%	4.09%	5.34%
4000	100	12.97%	0.04%	12.76%
4000	800	16.70%	0.93%	15.37%
4000	2000	18.24%	3.89%	13.80%
4000	3900	14.22%	6.43%	6.53%

The selection efficiency for the $\tau\tau$ preselection with both the resolved and boosted region is shown in Table 3. Among the selected $\tau\tau$ events, the rate of $\tau_{\text{e}}\tau_h$ and $\tau_{\text{e}}\tau_h$ channels are also calculated.

2.3 Background samples

An overview of simulated background samples used in this analysis is in Table 4. Legends in the plots shown in this analysis note group the background samples as :

- Nonprompt : will be defined in Section 7.2.
- Top : t+X, $t\bar{t}$+X
- Others : V+X, VV+X, VVV+X

3 Analysis Strategy

3.1 Triggers

This analysis targets a final state which consists of a hadronic tau accompanied by a nearly back-to-back light lepton, which has two nearby AK4 jets or a single AK8 jet. This differ-

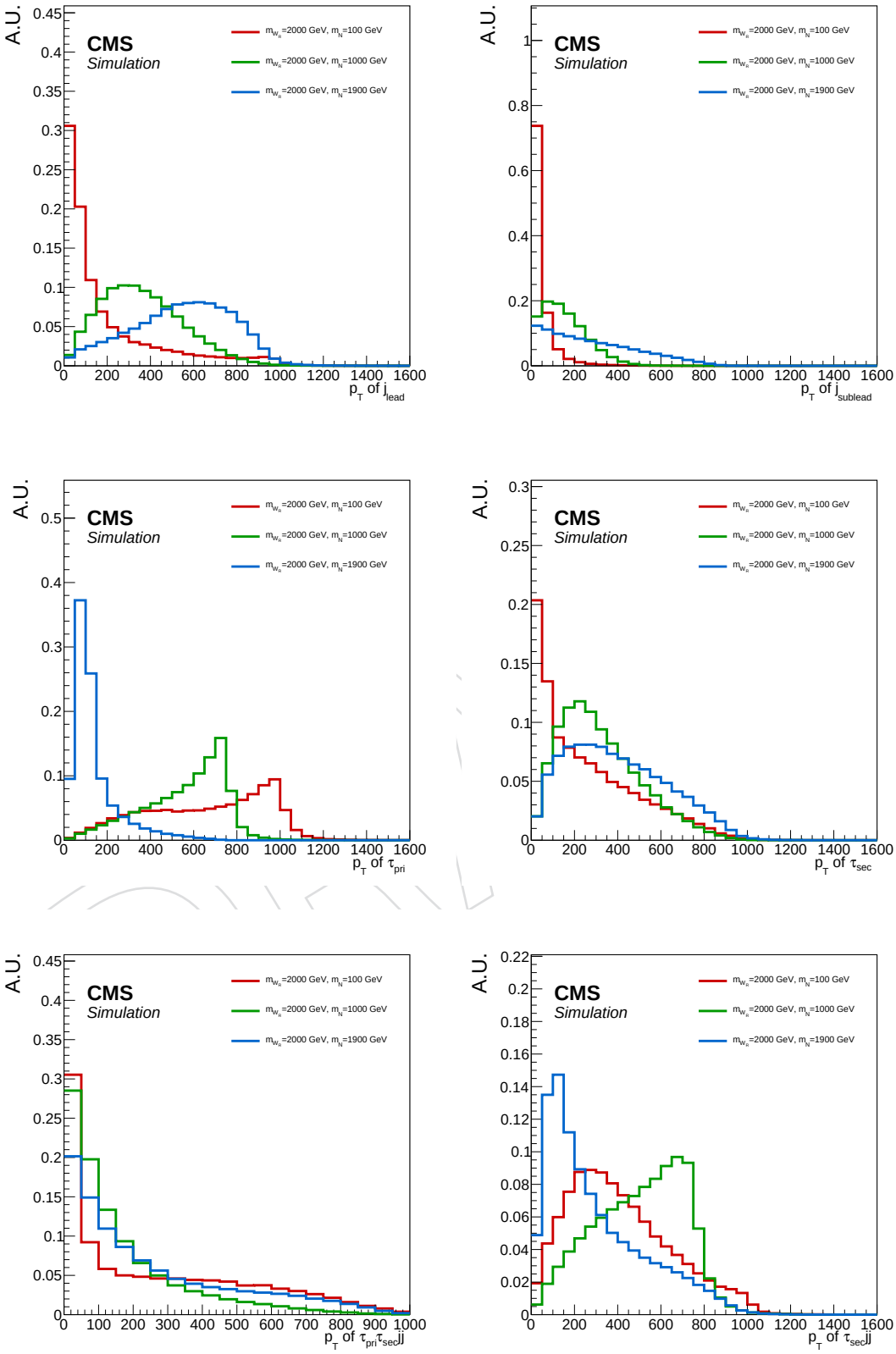

Figure 3: The p_T distributions of the (sub)leading jet, primary and secondary τ, and N, W_R normalized by the number of events produced with different m_N but fixed $m_{W_R} = 2$ TeV.

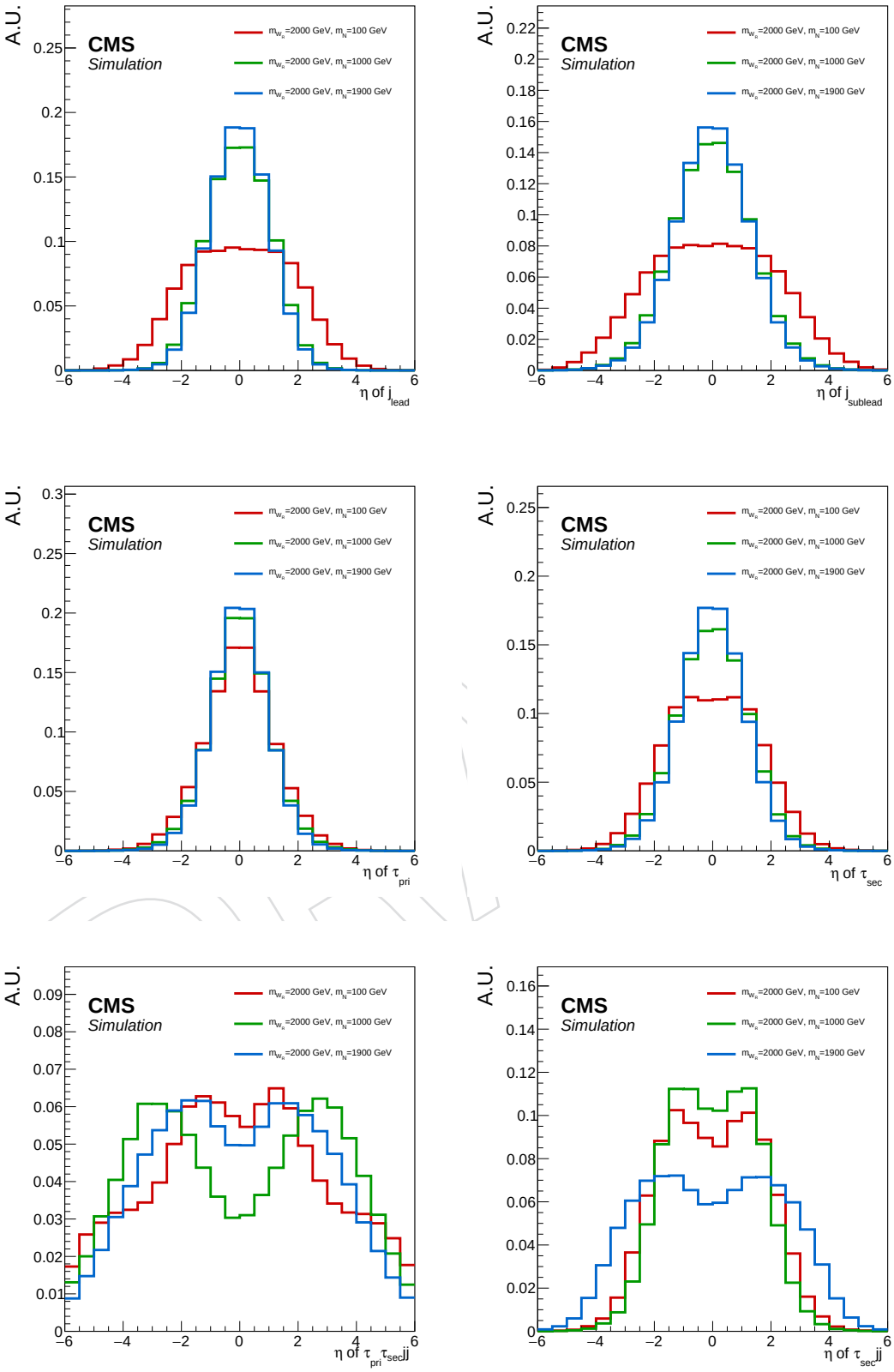

Figure 4: The η distributions of (sub)leading jet, primary and secondary τ, and N, W_R normalized by the number of events produced with different m_N but fixed $m_{W_R} = 2$ TeV.

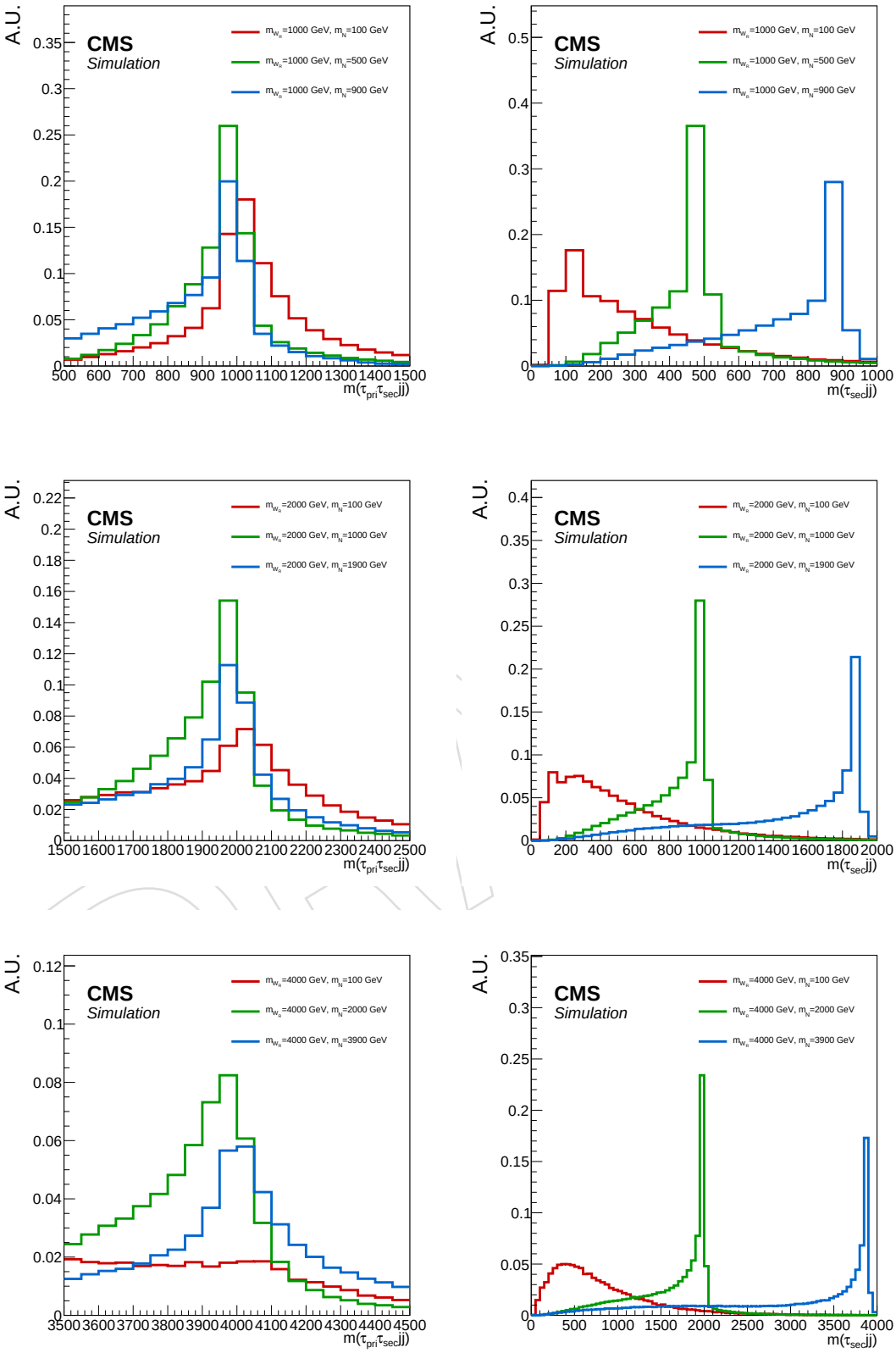

Figure 5: The invariant mass distribution of W_R and N for $m_{W_R} = 1, 2$ and 4 TeV.

Table 4: Background samples used in this analysis. All samples were produced up to the MINIAODSIM level for campaigns corresponding to each era listed in Table 2

.

Sample		σ (pb)
$t\bar{t}$+X	TTToHadronic_TuneCP5_13TeV-powheg-pythia8	377.96
	TTTo2L2Nu_TuneCP5_13TeV-powheg-pythia8	365.34
	TTToSemiLeptonic_TuneCP5_13TeV-powheg-pythia8	88.29
t+X	ST_t-channel_antitop_5f_InclusiveDecays_TuneCP5_13TeV-powheg-pythia8	80.0
	ST_t-channel_top_5f_InclusiveDecays_TuneCP5_13TeV-powheg-pythia8	134.2
	ST_tW_antitop_5f_inclusiveDecays TuneCP5_13TeV-powheg-pythia8	39.65
	ST_tW_top_5f_inclusiveDecays_TuneCP5_13TeV-powheg-pythia8	39.65
V+X	WJetsToLNu_TuneCP5_13TeV-madgraphMLM-pythia8	61526.7
	DYJetsToLL_M-50_TuneCP5_13TeV-madgraphMLM-pythia8	6077.2
VV+X	WW_TuneCP5_13TeV-pythia8	118.7
	WZ_TuneCP5_13TeV-pythia8	51.1
	ZZ_TuneCP5_13TeV-pythia8	16.91
VVV+X	WWW_4F_TuneCP5_13TeV-amcatnlo-pythia8	0.2086
	WWZ_4F_TuneCP5_13TeV-amcatnlo-pythia8	0.1651
	WZZ_TuneCP5_13TeV-amcatnlo-pythia8	0.05565
	ZZZ_TuneCP5_13TeV-amcatnlo-pythia8	0.01398

ence of jet topologies near the light lepton occurs from how boosted or resolved the secondary W_R decaying from N is. If the secondary W_R is boosted enough which is the case where $m(W_R) \gg m(N)$,the leptons and two AK4 jets would collimate, thus resulting in a single AK8 jet with a light lepton inside it. In the other case where $m(W_R) \simeq m(N)$, will result in a well seperated system of two AK4 jets with a light lepton nearby. This analysis mainly focuses on the improvement in the phase space where $m(W_R) \gg m(N)$ which will have a highly non-isolated light lepton, thus triggering on the hadronic tau would be a suitable strategy. The single hadronic tau triggers used in this analysis are summarized in Table 5.

Table 5: Single tau triggers used for each Run II era.

Year	HLT Path Name
2016	HLT_VLooseIsoPFTau140_Trk50_eta2p1_v*
2017	HLT_MediumChargedIsoPFTau180HighPtRelaxedIso_Trk50_eta2p1_v*
2018	HLT_MediumChargedIsoPFTau180HighPtRelaxedIso_Trk50_eta2p1_v*

4 Object Definition and Identification

The CMS global event reconstruction, utilizing the particle-flow (PF) algorithm, seeks to identify and reconstruct each particle in an event by integrating data from the various CMS subdetectors [14]. By determining particle types such as photons, electrons, muons, as well as charged and neutral hadrons, the direction and energy of the particle objects can be accurately measured.

4.1 Muons

4.1.1 Reconstruction

Muons are reconstructed by starting from a track in the muon system, which is matched with another track in the tracker. Additional information regarding muon reconstruction algorithms is described in detail in [15]. The reconstruction of high-p_{T} muons which are the main focus of this analysis are unreliable using a single reconstruction algorithm as in such high p_{T} region momentum resolution of trackers and muon systems are low. Thus, the so-called 'cocktail' (TuneP) algorithm is introduced to compensate for the inefficiency of reconstructing high-p_T muons.[16]

4.1.2 Identification

High-p_T muons used in this analysis are identified by the following :

- The muon is reconstructed as a global muon.
- At least one muon chamber hit is included in the global muon track fit.
- At least two muon stations have muon segments.
- The p_T relative error, σ_{p_T}/p_T of the muon best track is less than 0.3.
- Muon tracks must have at least one pixel hit.
- At least six tracker layer hits are required in the reconstruction.
- The transverse impact parameter, with respect to the primary vertex, must be less than 2mm, and the longitudinal distance of the track must be less than 5mm.

The last requirement is included to exclude muons from cosmic rays and decays-in-flights, which usually have longer impact parameters than the muons that are in our interest. Also, to reject muons rooting from jets.

4.1.3 Corrections

Additional momentum corrections are applied to the reconstructed muons. The momentum is corrected using the Rochester correction for muons with $p_T \leq 200\,\mathrm{GeV}$. [17] In the case of muons with $p_T \geq 200\,\mathrm{GeV}$, the generalized-endpoint (GE) method [18, 19] is used, which corrects the position and width of the dimuon mass peak from $\mathrm{Z}^0 \to \mu\mu$ processes in simulations and data to make better agreement.

4.1.4 Selection

Muons are classified into two selection categories: tight and loose. These categories are designed to reconstruct both resolved and boosted signal events optimally. Tight leptons are used to identify isolated leptons similar to those expected in resolved signals. On the other hand, loose leptons, resembling non-isolated leptons in boosted signals, must be within a wide

cone jet to help reconstruct a merged jet consisting of quarks and a lepton. The detailed cuts for both selections are shown in Table 6.

Table 6: Summary table of muon selections

Requirement	Loose	Tight
$\|\eta\|$	< 2.4	< 2.4
p_T	$> 53\,\text{GeV}$	$> 53\,\text{GeV}$
ID	HighPt	HighPt
Isolation	-	Relative Tracker Isolation < 0.1

4.2 Electrons

4.2.1 Reconstruction

Electrons are reconstructed from ECAL clusters matched to GSF tracks that require a shower shape consistent with an electromagnetic interaction. Accounting for the imperfect measurement of electron energy in data, a correction is applied, obtained using $Z^0 \rightarrow ee$ events. A scale factor is applied to electrons in the data to correct this mid-measurement according to the recipe provided by the Egamma POG. A correction to the MC must also be applied to correct the differences in resolution by smearing the energy of electrons. Smearing, scaling, and reconstruction efficiency scale factors were provided by the POG.

4.2.2 Identification

Reconstructed electrons must meet the criteria of the HEEP identification. This involves the electron having a high-quality, isolated track spatially correlated with an isolated ECAL energy deposit. Moreover, the shape of the ECAL energy deposit shower must match that of a genuine electromagnetic shower. A scale factor from the EGamma POG was applied to account for discrepancies in electron identification efficiencies between data and simulation. [20]

4.2.3 Selection

Identical to the case of muons, there are again loose and tight selections to recover boosted and resolved signals, respectively. Tight electrons are required to pass the HEEP identification, while for the loose case the centrally defined Egamma POG cut based loose identification [21] without the relISoWithEA criterion is required. The selections are summarized in Table 7.

Table 7: Summary table of electron selections

Requirement	Loose	Tight
$\|\eta\|$	< 2.4	< 2.4
p_T	$> 53\,\text{GeV}$	$> 53\,\text{GeV}$
ID	Cut Based Loose without relIsoWithEA	HEEPv7

4.3 Taus

4.3.1 Reconstruction

Taus themselves are not a stable particle. Thus, they decay either hadronically or leptonically. In CMS, hadronically decaying taus are reconstructed using the hadron-plus-strip (HPS) algorithm [22], which searches for tracks of at least one charged hadron and strips originating from neutral pions, which usually decay into two photons. These photons are likely to produce a

pair of oppositely charged electrons, which will curve in opposite directions due to the uniform magnetic field inside the CMS, thus making a strip-like trail of hits in the ECAL. Seeded by PF jets with $\Delta R = 0.4$, the mentioned signatures are found and used to reconstruct hadronic taus using the HPS algorithm.

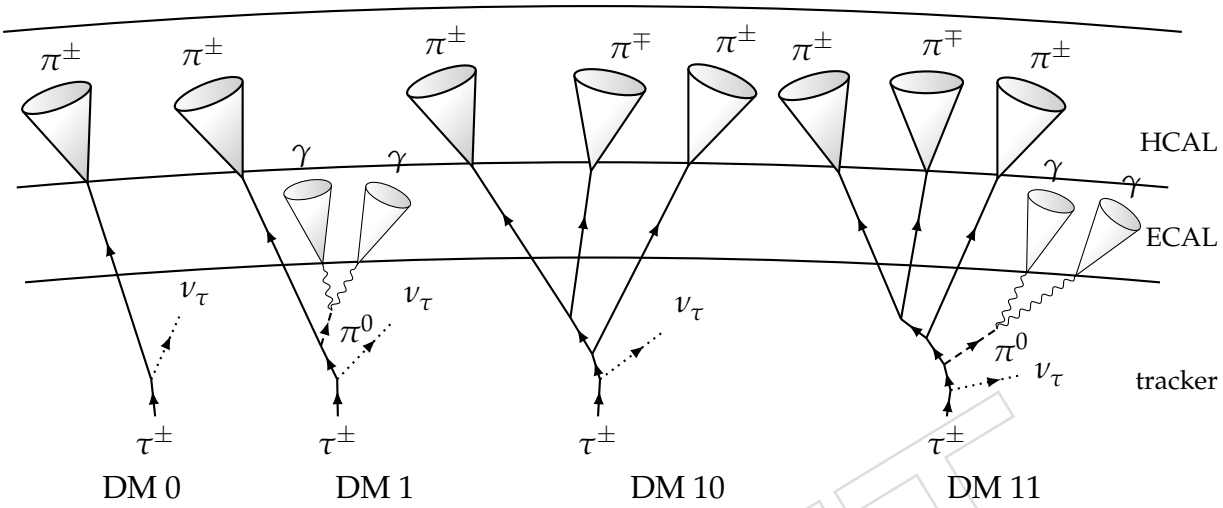

Figure 6: Decay modes (DM) of hadronic taus identified in CMS

The decay modes (DM) are defined as in Eq. 1, which is classified by the number of charged hadrons (n_{Prong}) and strips (n_{Strip}).

$$\text{DM} = 5 \times (n_{\text{Prong}} - 1) + n_{\text{Strip}} \tag{1}$$

4.3.2 Identification

Previously, multi-variate driven discriminators were used to distinguish genuine taus from jets or leptons. Now, DeepTau [23], a newly developed deep neural network driven discriminator, is used to differentiate taus from other objects. It classifies tau leptons compared to jets, muons, and electrons, generating three outputs to differentiate tau leptons from these particles, helping to lower the chances of incorrectly identifying electrons and muons as tau leptons. In this analysis, v2.1 is used.

4.3.3 Selection

Taus selected for the analysis are summarized in Table 8 labeled as "Tight". Besides that, there is one other set of selections labeled as "Fake", which are used to measure the jet to hadronic tau nonprompt contribution, with an orthogonal loose selection for the DeepTau vsJet working points. Both selection first requires `NewDecayMode` to be true in order to identify hadronic taus with the DeepTau algorithm and then requires decay modes 0,1,10 and 11 only by excluding 2-prong cases. For the DeepTau working points, in the case of tight ID, vsJet, vsEl and vsMu working points are selected all as `Tight` while for fake ID only the vsJet working point is selected to pass `VVVLoose` but not `Tight`. Nonprompt hadronic taus will be explained in detail in Section 7.2.

Table 8: Summary table of tau selections

Requirement	Fake	Tight
$\|\eta\|$	< 2.1	< 2.1
$\|dZ\|$	< 0.2	< 0.2
NewDecayMode	True	True
DecayMode	0,1,10,11	0,1,10,11
DeepTau vsJet	VVVLoose and !Tight	Tight
DeepTau vsEl	Tight	Tight
DeepTau vsMu	Tight	Tight

4.4 Jets

4.4.1 Reconstruction

Jets are reconstructed by clustering particle flow (PF) candidates using the anti-k_T algorithm [24] for each event. These jets are categorized by a distance parameter $R = \sqrt{(\Delta\eta)^2 + (\Delta\phi)^2}$, of either 0.4 (AK4) or 0.8 (AK8). Two different methods are utilized for each AK4 and AK8 jet to mitigate the pileup (PU) effect stemming from multiple interactions in the same bunch crossing. For the AK4 jets, charged hadron subtraction (CHS) removes charged particles originating from non-primary vertices. For the AK8 jets, the pileup per particle identification (PUPPI) algorithm [25] is used to weigh the PF candidates before jet clustering.

4.4.2 Identification

The AK4 jets are required to pass the official JetMET POG "tight jet ID with lepton veto" ID. The requirements for this ID can be listed as follows:

- The neutral hadron and electromagnetic (EM) fractions must be less than 90%.
- At least two constituents in the jet.
- Muon energy fraction must be less than 80%.
- At least one charged hadron in the jet, while the charged hadronic fraction is greater than 0.
- The charged EM fraction must be less than 90% (2016) or 80% (2017,2018).

The AK8 jets are required to pass the official JetMET POG "tight" jet ID, which must pass the following conditions :

- The neutral hadron and EM fractions must be less than 90%.
- At least two constituents in the jet.
- At least one charged hadron in the jet, and the charged hadronic fraction must be greater than 0.
- The charged EM fraction must be less than 99% for 2016 only.

4.4.3 Lepton Subjet Fraction (LSF)

The so-called isolation for a reconstructed object, which is calculated as the ratio of the p_{T} sum of objects within a cone of a certain radius around it to the p_{T} of the object itself, is not an ideal variable to identify signal objects in highly boosted topologies [26]. This is because cutting on isolation in such situations rejects backgrounds but at the cost of significant signal loss.

In cases where the event has boosted topologies, the lepton subjet fraction (LSF) can be utilized

as a better measure. It is calculated similarly to traditional isolation and involves clustering objects in an event into fatjets using the anti-kT algorithm with a radius parameter of R = 0.8. Then, the exclusive kT algorithm is used to cluster the constituents of each fat jet into n-subjets, where the specific final state topology determines n. Finally, the LSF_n quantity is calculated as follows:

$$\mathrm{LSF}_n = \frac{p_{\mathrm{T}}^{\ell}}{p_{\mathrm{T}}^{\mathrm{sj}}} \tag{2}$$

where $p_{\mathrm{T}}^{\mathrm{sj}}$ is the p_{T} of the subjet containing the lepton in concern, and p_{T}^{ℓ} the p_{T} of that lepton itself. LSF values close to 1 indicate that the lepton is more isolated. A benchmark test using SUSY models was performed in [26], which showed that the signal final state leptons have LSF values peaking near 1, while the background leptons dominating from $\mathrm{b\bar{b}}$ decays peaking around 0.2.

A significance test for the cut value of LSF_3 was done to determine the optimal choice shown in detail in Appendix B.2.

4.4.4 Selection

The kinematics of the jet system differ significantly by the boost, thus having different jet topologies in the resolved and boosted regions. When the system is not boosted enough, one would expect the two AK4 jets from the signal W decay to be resolved, thus giving a two AK4 jet signal. Meanwhile, if there is enough boost to the system, those two AK4 jets are likely to be collimated, thus resulting in a single AK8 jet. The selections required for both AK4 and AK8 jets are summarized in Table 9.

Table 9: Summary table of jet selections

Requirement	AK4	AK8
$\lvert\eta\rvert$	< 2.4	< 2.4
p_{T}	$> 40\,\mathrm{GeV}$	$> 200\,\mathrm{GeV}$
ID	Tight	Tight with Lepton Veto
LSF	-	> 0.6

4.5 Missing Transverse Energy

The missing transverse energy (MET) is defined as the magnitude of negative 4-vector sum of all visible particles. Type 1 correction which takes account of jet energy corrections is applied. Changes of jet p_{T} due to jet energy scale and resolution are also propagated into MET too. In this analysis, the PUPPI missing transverse energy (MET) reconstruction [27] is used, which utilizes a local shape variable used to distinguish between the collinear arrangement of particles resulting from the hadronization of quarks and gluons produced through QCD mechanisms, and the soft, diffuse radiation originating from pileup. MET filters recommended by the JetMET POG are also applied in order to relieve instrumental effects from the detector which is summarized in Table 10.

Table 10: Summary of the MET filters used in this analysis.

path	dataset	2016	2017	2018
Flag_goodVertices	data & MC	✓	✓	✓
Flag_globalSuperTightHalo2016Filter	data & MC	✓	✓	✓
Flag_HBHENoiseFilter	data & MC	✓	✓	✓
Flag_HBHENoiseIsoFilter	data & MC	✓	✓	✓
Flag_EcalDeadCellTriggerPrimitiveFilter	data & MC	✓	✓	✓
Flag_BadPFMuonFilter	data & MC	✓	✓	✓
Flag_BadPFMuonDzFilter	data & MC	✓	✓	✓
Flag_eeBadScFilter	data	✓	✓	✓
Flag_ecalBadCalibFilterV2	data & MC	–	✓	✓
Flag_hfNoisyHitsFilter	data & MC	✓	✓	✓

5 Corrections

Several corrections are given to the simulated samples to describe the data sufficiently.

5.1 Electron and muon ID scale factor

Both muon and electron ID scale factors are taken from relevant POGs. [28]

5.2 Hadronic tau ID and energy scale

The energies of actual hadronic tau candidates can differ between data and simulation and across decay modes. To correct this discrepancy, Tau POG provides an energy scale measured from Z boson decays in the $\mu\tau_h$ channel, which only depends on the decay mode. Such correction is then applied to the hadronic tau 4-vectors by directly scaling them. Not only for the hadronic taus but such correction is also propagated to the missing transverse energy. Additionally, the identification efficiency of genuine hadronic taus can differ between data and simulation. This is also relieved by applying scale factors measured by the Tau POG binned by the hadronic tau p_{T}.

5.3 Prefire reweighting

The ageing of ECAL crystals disturbed the timing of two consecutive bunches, which led to the firing of L1. This eventually affected the data in 2016 and 2017. Such an effect is taken into account in simulated samples by weighting the events.

5.4 Pileup reweighting

In order to match the pileup conditions in simulation with data, simulated samples are reweighted to account for pileup.

5.5 Trigger scale factor

The single hadronic tau trigger scale factors are given flat between 0.87 and 1.08 by the year, as recommended by Tau POG. [29]

5.6 Jet energy scale and resolution correction

The jet energy and resolution corrections are applied using the JetMET POG recommendation. [30] The correction versions per era, period, and type of samples are given in Table 11.

Table 11: Jet energy correction (JEC) tags used in different eras for MC/data.

	Global tags	Era	JEC file tags
MC	106X_mcRun2_asymptotic_preVFP_v11	UL2016_preVFP	Summer19UL16APV_V7_MC
	106X_mcRun2_asymptotic_v17	UL2016_postVFP	Summer19UL16_V7_MC
	106X_mc2017_realistic_v10	UL2017	Summer19UL17_V6_MC
	106X_upgrade2018_realistic_v15_L1v1	UL2018	Summer19UL18_V5_MC
Data	106X_dataRun2_v35	UL2016_preVFP_B UL2016_preVFP_C UL2016_preVFP_D	Summer19UL16APV_RunBCD_V7_DATA
		UL2016_preVFP_E UL2016_preVFP_F	Summer19UL16APV_RunEF_V7_DATA
		UL2016_F UL2016_G UL2016_H	Summer19UL_RunFGH_V7_DATA
	106X_dataRun2_v33	UL2017_B	Summer19UL18_RunB_V6_DATA
		UL2017_C	Summer19UL18_RunC_V6_DATA
		UL2017_D	Summer19UL18_RunD_V6_DATA
		UL2017_E	Summer19UL18_RunE_V6_DATA
		UL2017_F	Summer19UL18_RunF_V6_DATA
		UL2018_A	Summer19UL18_RunA_V5_DATA
		UL2018_B	Summer19UL18_RunB_V5_DATA
		UL2018_C	Summer19UL18_RunC_V5_DATA
		UL2018_D	Summer19UL18_RunD_V5_DATA

6 Event Selection

Events are split into two categories, targeting boosted and resolved final states. Among the events that pass the single tau trigger mentioned in Section 3.1 and having at least one hadronic tau that passes the hadronic tau requirement in Section 4.3 with p_T larger than the corresponding trigger safe p_T cut for each era, the preselection region is divided into two orthogonal regions :

- Resolved preselection:
  - At least two AK4 jets.
  - One "tight" lepton with $p_T > 53\,\text{GeV}$.
- Boosted preselection:
  - Fails resolved preselection.
  - At least one AK8 jet.
  - One "loose" lepton.

Preselected events are further classified into boosted and resolved signal and control regions as follows:

1. Resolved regions:
   - Passes the resolved preselection.
     - **Fake Control Region**
       - MET $< 100\,\text{GeV}$ and $m(\tau_h jj) < 500\,\text{GeV}$
   - ΔR between any pair of the leptons, leading hadronic tau and the two leading AK4 jets are greater than 0.4.
   - The leading lepton, which passes the ΔR criteria and the Tight ID, is selected and denoted as ℓ_{Tight}.
     - **Resolved Signal Region**

- MET $> 100\,\text{GeV}$ and $m(\tau_h \ell_{\text{Tight}} jj) > 900\,\text{GeV}$
- **Resolved QCD Tau Fake Measurement Region**
  - MET $< 100\,\text{GeV}$ and $m(\tau_h \ell_{\text{Tight}} jj) > 900\,\text{GeV}$

2. Boosted regions:
   - Passes the boosted region preselection.
     - **Fake Control Region**
       - MET $< 100\,\text{GeV}$ and $m(\tau_h J) < 500\,\text{GeV}$
   - At least one AK8 jet with LSF requirement satisfies $\Delta\phi(\ell_{\text{Loose}}) > 2.0$, and if so the leading AK8 jet (J) is selected for analysis.
   - At least one loose lepton satisfies $\Delta R(\ell_{\text{Loose}}, J) < 0.8$ and if so, the leading lepton is selected.
     - **Boosted Signal Region**
       - MET $> 100\,\text{GeV}$ and $m(\tau_h J) > 900\,\text{GeV}$
     - **Boosted QCD Tau Fake Measurement Region**
       - MET $< 100\,\text{GeV}$ and $m(\tau_h J) > 900\,\text{GeV}$

All regions are then again divided into electron or muon channels depending on the flavour of the lepton selected. The mass cuts are optimized to maximize signal significance in the signal region, described in detail in Appendix B.1. Fig. **??** shows a diagram summarizing all the signal and control regions.

6.1 Signal Efficiency

Signal efficiencies for signal samples are shown in Appendix A.3

6.2 Preselection

6.2.1 Yields

Table 12: Yields for each background group and data in the fake control region summarized into a table for each Run2 UL eras

	2016preVFP	2016postVFP	2017	2018
Fakes	324.30±6.50	304.78±6.26	124.45±4.75	214.12±6.11
Top	32.13±1.18	33.80±1.17	21.78±1.02	24.87±1.01
Others	12.23±2.88	10.31±2.54	10.44±4.81	10.76±5.48
Total	368.66±7.21	348.89±6.86	156.67±6.84	249.75±8.27
Data	376	381	155	268
Data/Prediction	1.01	1.09	0.99	1.07

6.2.2 Plots

The MET and $m_{\text{Eff.}}$ distributions are shown in Fig. 7 – 10 and Fig. 11 – 14 for each Run2 UL eras.

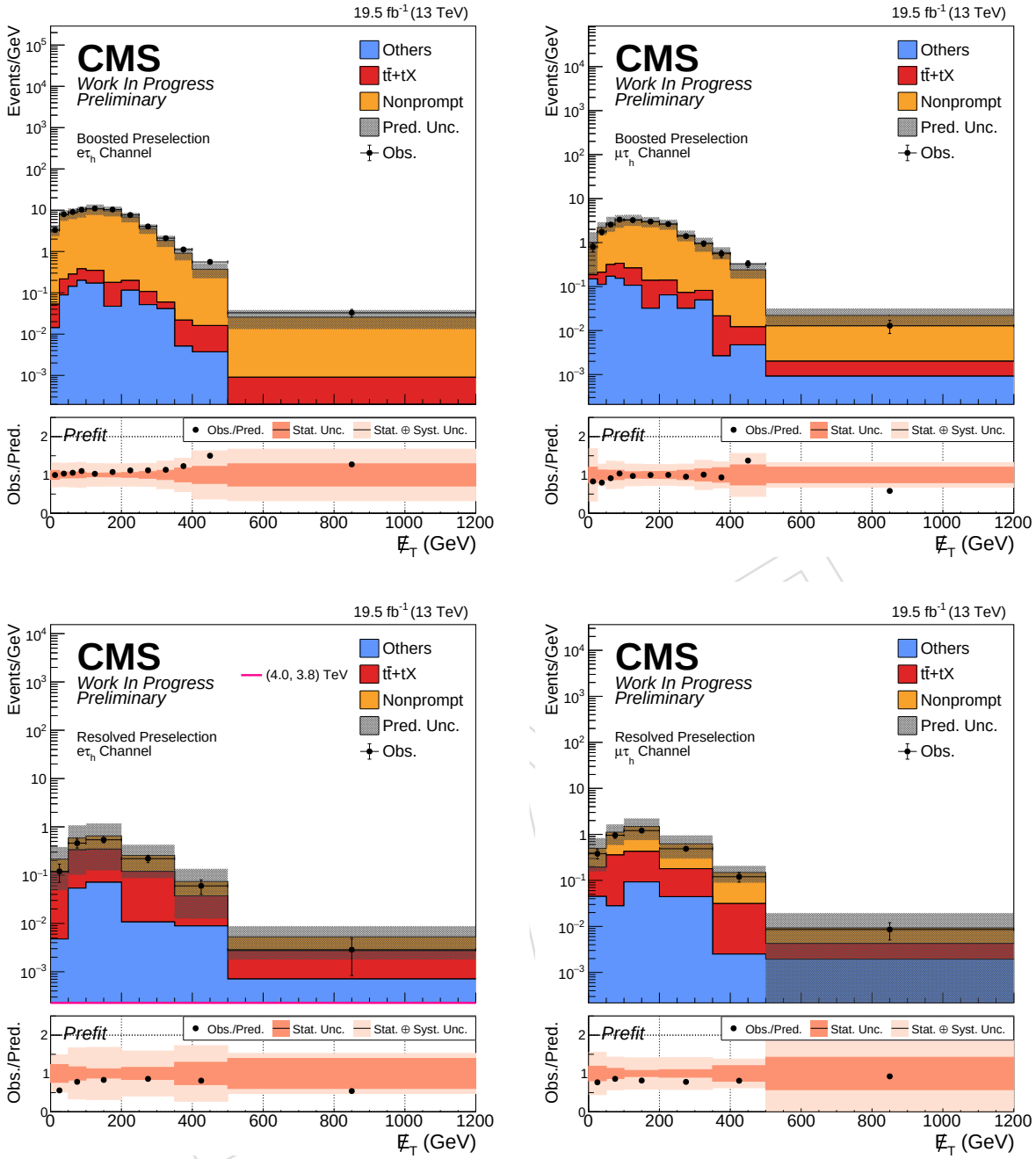

Figure 7: MET distribution shown for the electron (muon) channel in the left (right) column, and for the boosted (resolved) channel in the upper (lower) column for the 2016preVFP era.

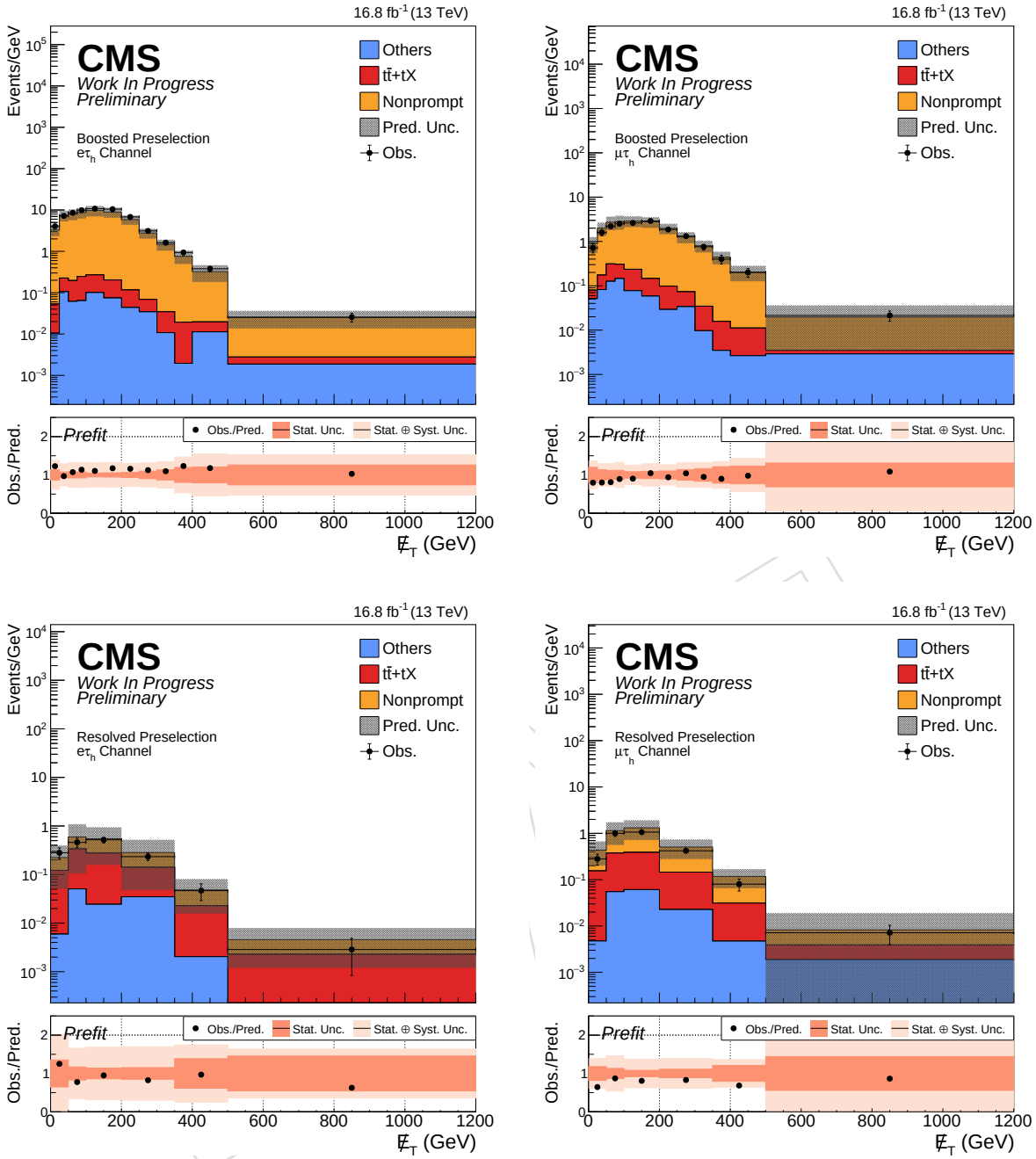

Figure 8: MET distribution shown for the electron (muon) channel in the left (right) column, and for the boosted (resolved) channel in the upper (lower) column for the 2016postVFP era.

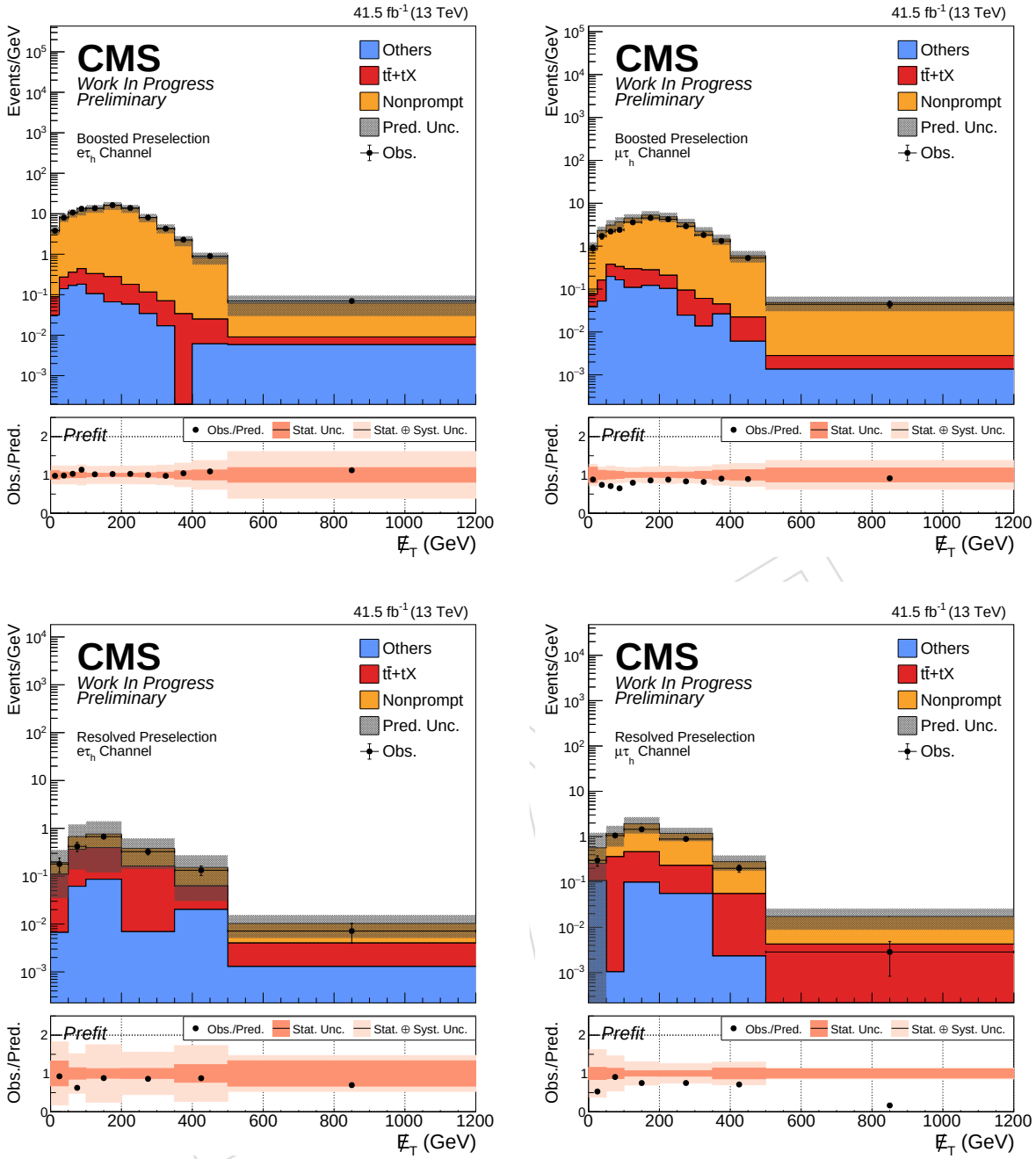

Figure 9: MET distribution shown for the electron (muon) channel in the left (right) column, and for the boosted (resolved) channel in the upper (lower) column for the 2017 era.

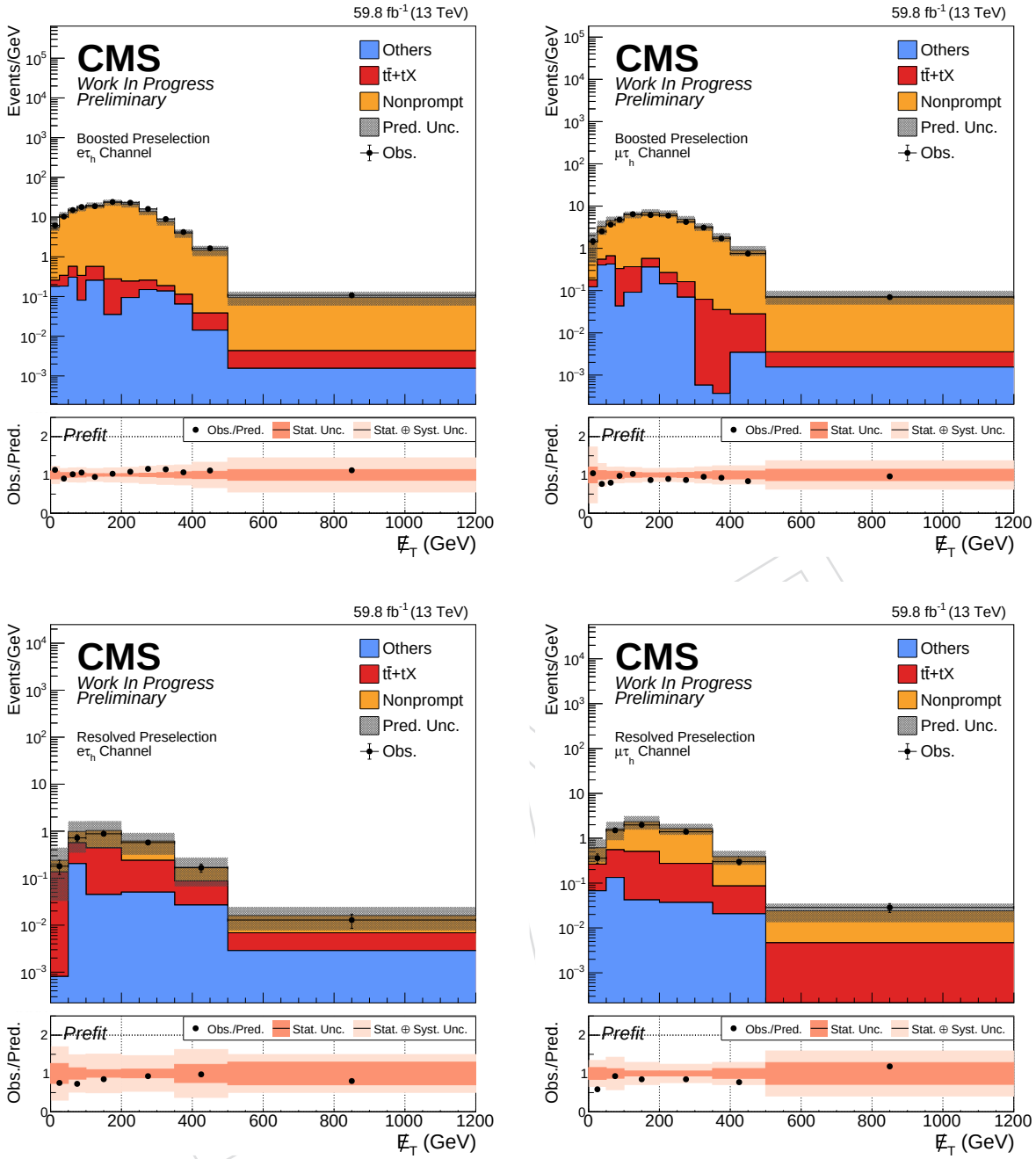

Figure 10: MET distribution shown for the electron (muon) channel in the left (right) column, and for the boosted (resolved) channel in the upper (lower) column for the 2018 era.

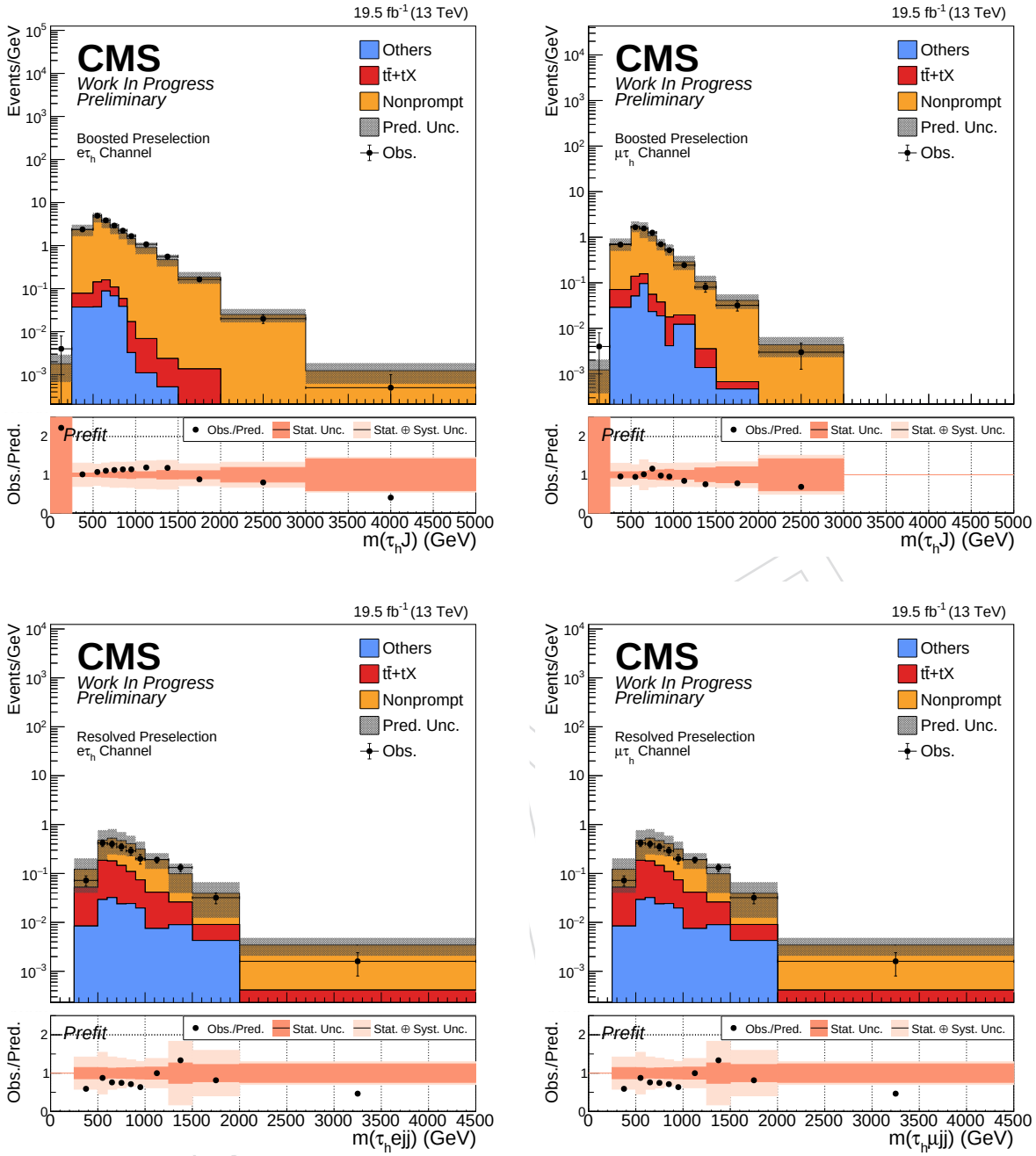

Figure 11: $m(\tau_h J)$ and $m(\tau_h \ell jj)$ distributions shown for the electron (muon) channel in the left (right) column, and for the boosted (resolved) channel in the upper (lower) column for the 2016preVFP era.

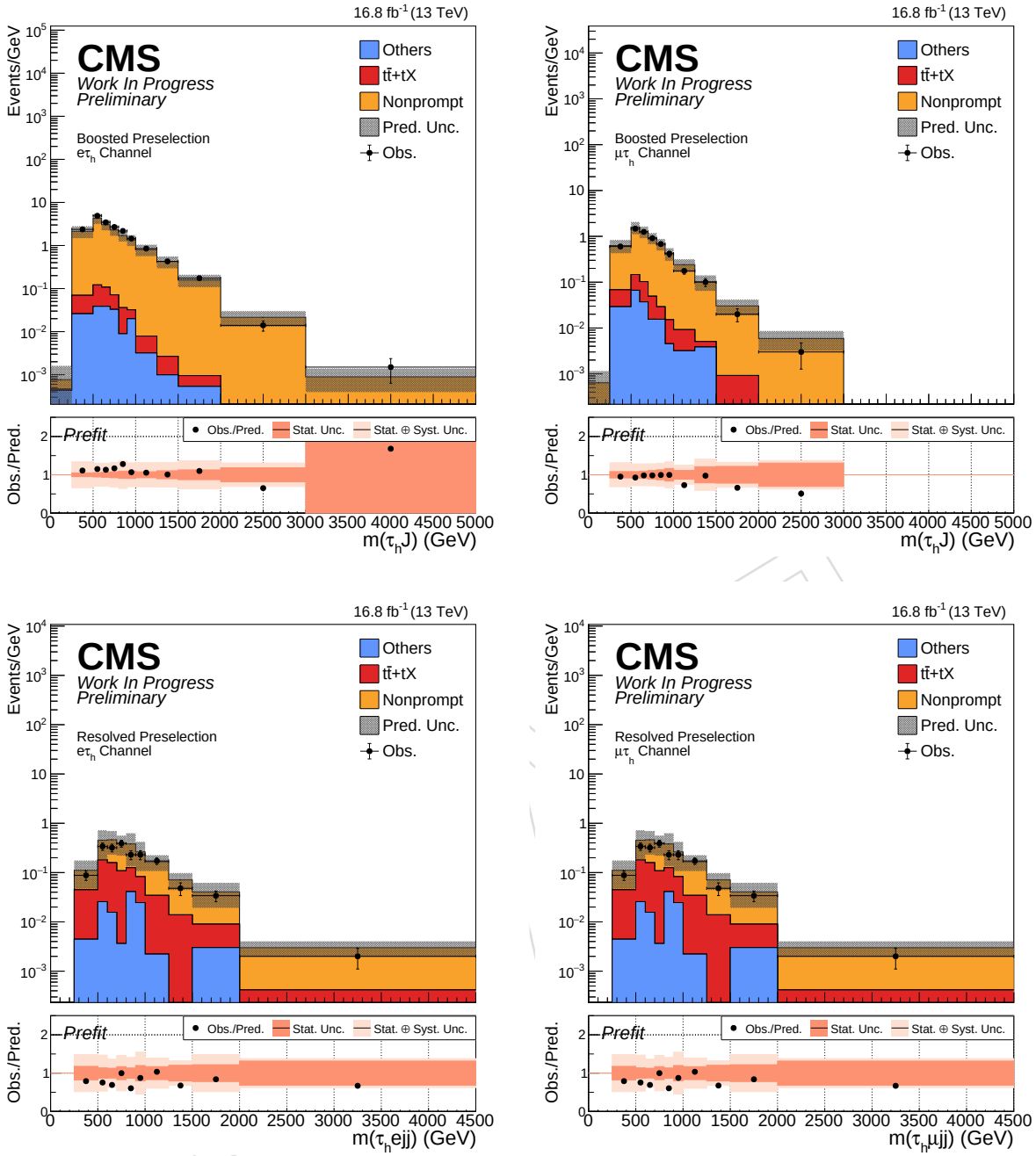

Figure 12: $m(\tau_h J)$ and $m(\tau_h \ell jj)$ distributions shown for the electron (muon) channel in the left (right) column, and for the boosted (resolved) channel in the upper (lower) column for the 2016postVFP era.

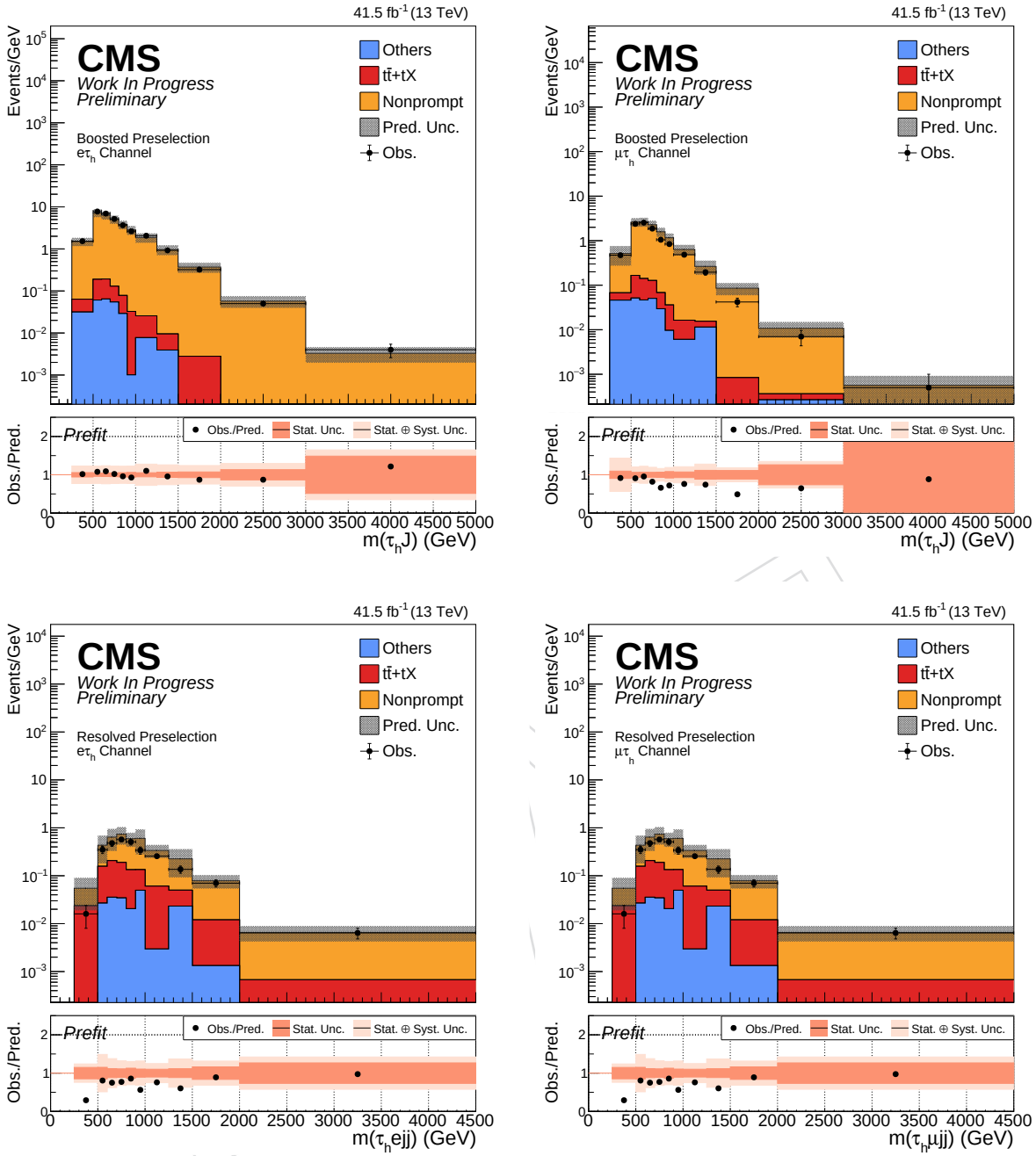

Figure 13: $m(\tau_h J)$ and $m(\tau_h \ell jj)$ distributions shown for the electron (muon) channel in the left (right) column, and for the boosted (resolved) channel in the upper (lower) column for the 2017 era.

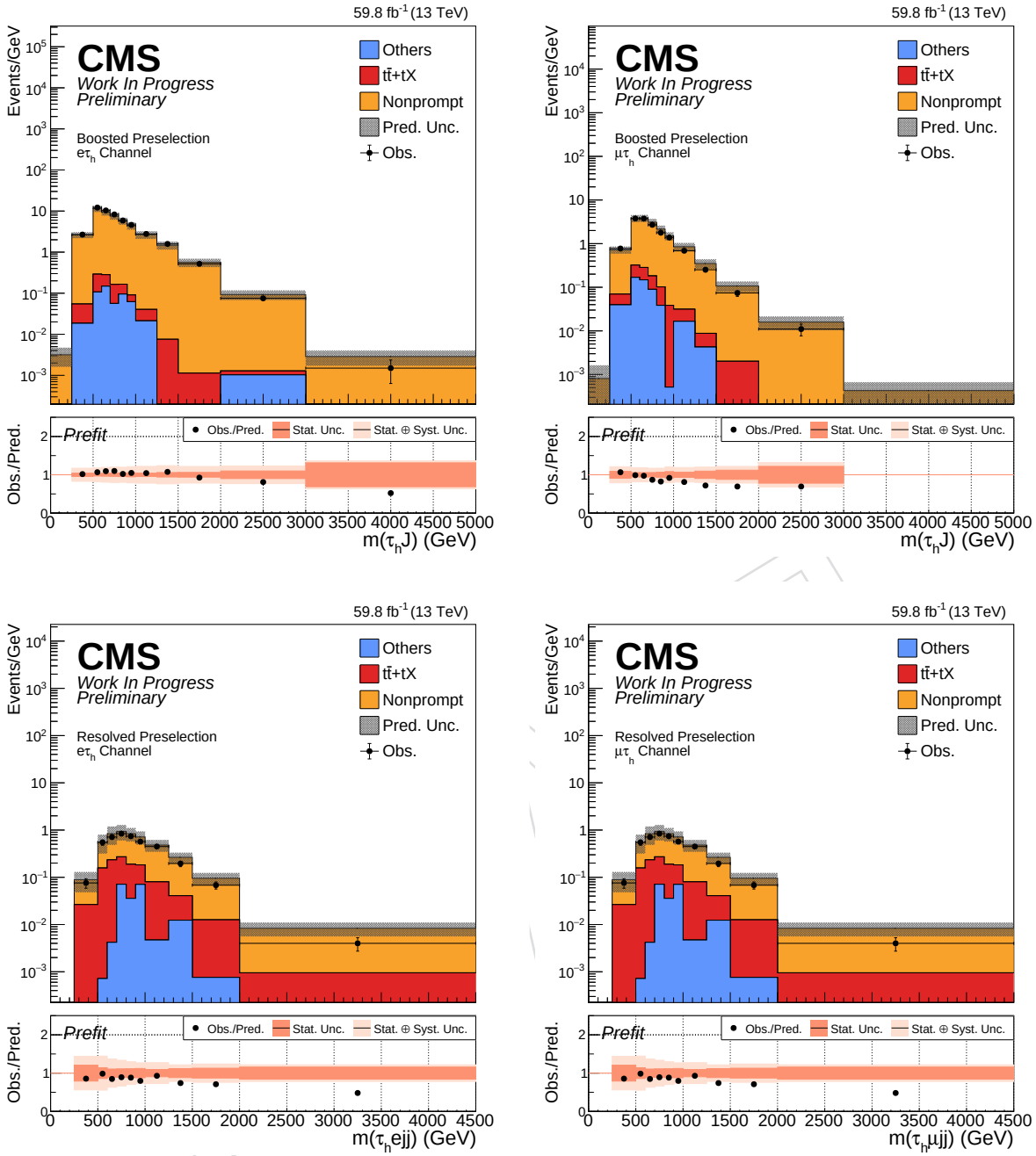

Figure 14: $m(\tau_h J)$ and $m(\tau_h \ell jj)$ distributions shown for the electron (muon) channel in the left (right) column, and for the boosted (resolved) channel in the upper (lower) column for the 2018 era.

6.3 Control Region

6.3.1 Yields

6.3.2 Plots

The $m(\tau_h J)$ and $m(\tau_h \ell jj)$ distribution are shown in Fig 15 for the fake control region. The backgrounds grouped in the legend are following the naming convention defined in Section 2.3.

Table 13: Yields for each background group and data in the fake control region summarized into a table for each Run2 UL eras

	2016preVFP	2016postVFP	2017	2018
Fakes	324.30±6.50	304.78±6.26	124.45±4.75	214.12±6.11
Top	32.13±1.18	33.80±1.17	21.78±1.02	24.87±1.01
Others	12.23±2.88	10.31±2.54	10.44±4.81	10.76±5.48
Total	368.66±7.21	348.89±6.86	156.67±6.84	249.75±8.27
Data	376	381	155	268
Data/Prediction	1.01	1.09	0.99	1.07

6.4 Signal Region

6.4.1 Yields

Yields for each selection steps up to the signal regions are shown as a cutflow table in Table 14 – 21

Table 14: Cutflow for each background group and data which is blinded after the preselection level in the resolved electron channel for Run2 UL era 2017.

	Preselection	$\Delta R > 0.4$	$m_{\mathrm{Eff}} > 900\,\mathrm{GeV}$	MET$> 100\,\mathrm{GeV}$
Fakes	105.97±4.57	100.59±4.45	52.89±3.29	44.72±3.07
Top	118.95±2.39	113.98±2.35	43.29±1.47	34.75±1.31
Others	134.49±61.22	99.19±50.06	90.96±49.94	87.83±49.87
Total	359.42±61.44	313.77±50.31	187.14±50.07	167.31±49.98
Data	171.00	164.00	77.00	66.00
Data/Prediction	0.64	–	–	–

Table 15: Cutflow for each background group and data which is blinded after the preselection level in the resolved muon channel for Run2 UL era 2018.

	Preselection	$\Delta R > 0.4$	$m_{\mathrm{Eff}} > 900\,\mathrm{GeV}$	MET$> 100\,\mathrm{GeV}$
Fakes	513.67±9.89	494.91±9.72	258.67±7.07	233.53±6.83
Top	177.12±2.87	170.08±2.82	62.69±1.77	49.27±1.58
Others	34.59±9.66	27.95±8.58	12.27±5.55	11.84±5.54
Total	725.39±14.12	692.94±13.27	333.62±9.16	294.65±8.94
Data	565	–	–	–
Data/Prediction	0.78	–	–	–

Table 16: Cutflow for each background group and data which is blinded after the preselection level in the boosted electron channel for Run2 UL era 2017.

	Preselection	Fatjet	$\Delta R(e, J) < 0.8$	$m_{\mathrm{Eff}} > 900\,\mathrm{GeV}$	MET$> 100\,\mathrm{GeV}$
Fakes	5740.80±31.62	408.46±8.45	405.85±8.43	91.67±4.03	72.46±3.64
Top	118.57±2.58	33.74±1.34	33.41±1.33	3.58±0.48	3.33±0.45
Boson	195.50±58.45	20.40±6.60	20.40±6.60	2.04±1.42	1.09±1.06
Total	6054.87±66.51	462.60±10.81	459.66±10.79	97.29±4.30	76.88±3.82
Data	6222	–	–	–	
Data/Prediction	1.03	–	–	–	

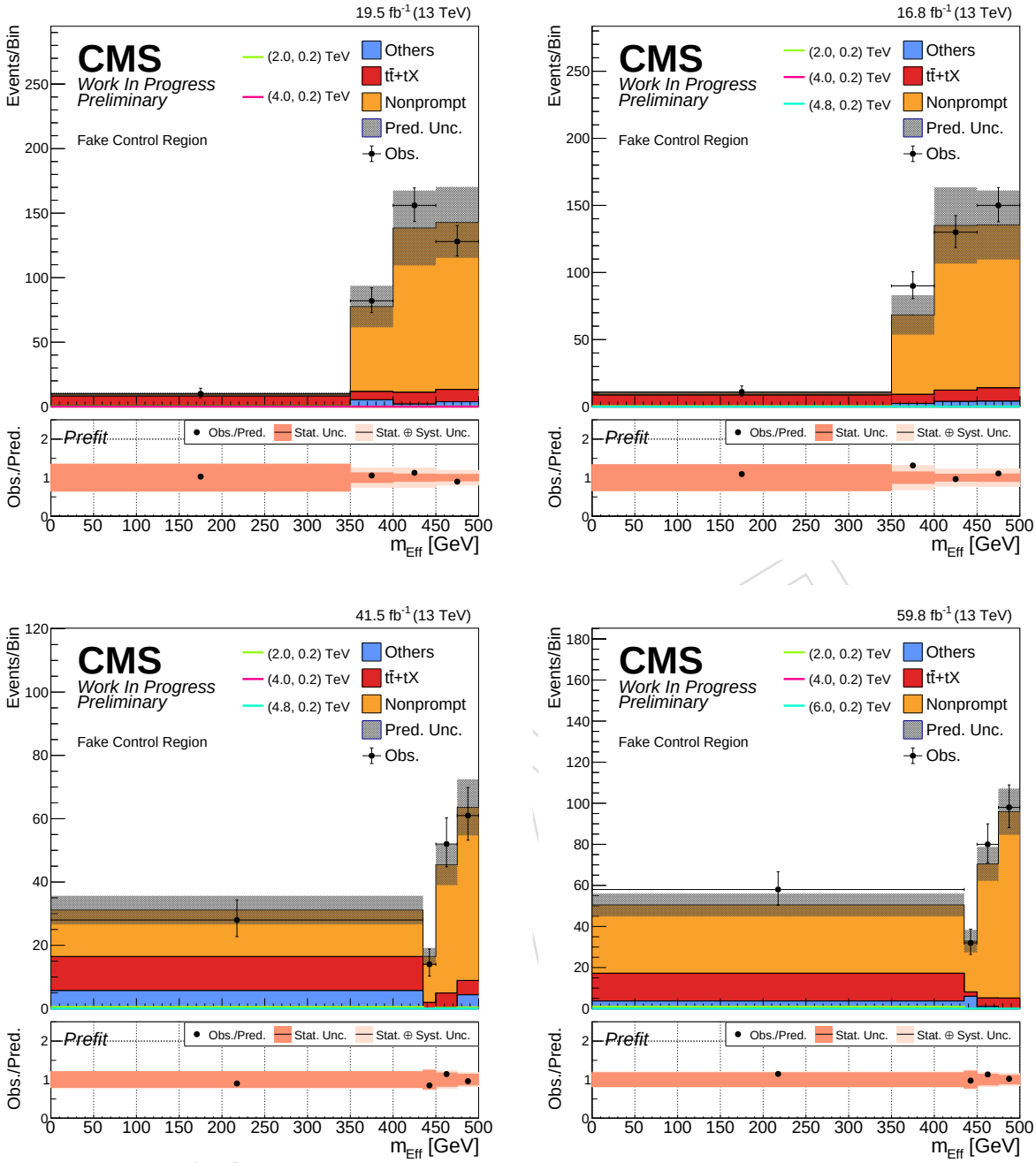

Figure 15: $m(\tau_h J)$ and $m(\tau_h \ell jj)$ in the fake control region for each UL era.

6.4.2 Plots

The $m(\tau_h J)$ and $m(\tau_h \ell jj)$ distribution for boosted and resolved signal regions, respectively, are shown in Fig 16–18. The signal samples shown in the plots are scaled to match 1% of the corresponding era luminosity. The backgrounds grouped in the legend are following the naming convention defined in Section 2.3. Observed data is blinded.

Table 17: Cutflow for each background group and data which is blinded after the preselection level in the boosted muon channel for Run2 UL era 2017.

	Preselection	Fatjet	$\Delta R(\mu, J) < 0.8$	$m_{\text{Eff}} > 900\,\text{GeV}$	MET$> 100\,\text{GeV}$
Fakes	1279.83±15.48	118.34±4.70	115.85±4.65	17.76±1.92	14.50±1.74
Top	118.59±2.63	30.42±1.28	29.95±1.27	4.03±0.47	3.27±0.44
Others	325.36±96.72	85.26±49.58	85.26±49.58	1.52±0.68	0.63±0.44
Total	1723.77±97.99	234.03±49.82	231.06±49.81	23.32±2.09	18.39±1.85
Data	1186	–	–	–	–
Data/Prediction	0.68	–	–		–

Table 18: Cutflow for each background group and data which is blinded after the preselection level in the resolved electron channel for Run2 UL era 2018.

	Preselection	$\Delta R > 0.4$	$m_{\text{Eff}} > 900\,\text{GeV}$	MET$> 100\,\text{GeV}$
$(m_{W_R}, m_N) = (2.0, 0.2)$ TeV	14446.23±535.23	14092.22±528.67	12471.02±497.31	11140.59±469.92
$(m_{W_R}, m_N) = (2.0, 1.8)$ TeV	40377.02±901.28	38497.18±880.09	37827.95±872.31	33478.06±820.61
$(m_{W_R}, m_N) = (6.5, 0.2)$ TeV	7784.53±396.91	7564.33±391.29	4382.06±298.02	3890.16±280.53
$(m_{W_R}, m_N) = (6.5, 6.3)$ TeV	98502.27±1404.89	96750.64±1392.39	96731.04±1392.25	94923.17±1379.22
Fakes	160.49±5.30	152.83±5.17	77.64±3.69	67.53±3.50
Top	105.46±2.17	102.24±2.13	38.12±1.37	29.97±1.23
Others	28.32±8.14	27.96±8.13	17.59±6.15	13.98±5.36
Total	294.28±9.95	283.04±9.87	133.35±7.30	111.49±6.52
Data	253	–	–	
Data/Prediction	0.86	–	–	

Table 19: Cutflow for each background group and data which is blinded after the preselection level in the resolved muon channel for Run2 UL era 2018.

	Preselection	$\Delta R > 0.4$	$m_{\text{Eff}} > 900\,\text{GeV}$	MET$> 100\,\text{GeV}$
$(m_{W_R}, m_N) = (2.0, 0.2)$ TeV	21760.66±663.37	21086.30±653.17	18688.75±614.95	16574.33±579.43
$(m_{W_R}, m_N) = (2.0, 1.8)$ TeV	51354.22±1029.57	49011.69±1005.59	47771.21±992.70	42910.60±940.48
$(m_{W_R}, m_N) = (6.5, 0.2)$ TeV	11553.28±487.17	11039.32±476.17	6333.66±360.09	5714.54±342.41
$(m_{W_R}, m_N) = (6.5, 6.3)$ TeV	125476.38±1607.81	122564.66±1588.87	122521.58±1588.58	120247.96±1574.05
Fakes	513.67±9.89	494.91±9.72	258.67±7.07	233.53±6.83
Top	129.83±2.44	125.42±2.40	45.02±1.50	33.39±1.30
Others	23.01±7.67	19.56±7.02	8.71±4.37	8.31±4.36
Total	666.52±12.75	639.89±12.23	312.39±8.45	275.23±8.20
Data	565	–	–	
Data/Prediction	0.85	–	–	

Table 20: Cutflow for each background group and data which is blinded after the preselection level in the boosted electron channel for Run2 UL era 2018.

	Preselection	Fatjet	$\Delta R(e, J) < 0.8$	$m_{\text{Eff}} > 900\,\text{GeV}$	MET$> 100\,\text{GeV}$
$(m_{W_R}, m_N) = (2.0, 0.2)$ TeV	63597.69±1162.07	25693.37±734.30	25648.71±733.62	21931.52±678.40	19268.94±636.07
$(m_{W_R}, m_N) = (2.0, 1.8)$ TeV	17109.65±626.31	2548.79±236.19	2304.91±222.65	1131.96±155.96	1048.01±150.18
$(m_{W_R}, m_N) = (6.5, 0.2)$ TeV	31476.81±826.09	10669.63±478.64	10615.47±477.04	8565.86±428.85	8013.52±414.90
$(m_{W_R}, m_N) = (6.5, 6.3)$ TeV	33986.20±873.24	4317.70±305.87	3884.79±287.54	3005.59±253.34	2962.56±251.51
Fakes	5740.80±31.62	408.46±8.45	405.85±8.43	91.67±4.03	72.46±3.64
Top	118.57±2.58	33.74±1.34	33.41±1.33	3.58±0.48	3.33±0.45
Others	195.50±58.45	20.40±6.60	20.40±6.60	2.04±1.42	1.09±1.06
Total	6054.87±66.51	462.60±10.81	459.66±10.79	97.29±4.30	76.88±3.82
Data	6222	–	–	–	
Data/Prediction	1.03	–	–	–	

Table 21: Cutflow for each background group and data which is blinded after the preselection level in the boosted muon channel for Run2 UL era 2018.

	Preselection	Fatjet	$\Delta R(\mu, J) < 0.8$	$m_{\text{Eff}} > 900\,\text{GeV}$	MET$> 100\,\text{GeV}$
$(m_{W_R}, m_N) = (2.0, 0.2)\,\text{TeV}$	62562.06±1148.44	27931.98±767.34	27791.59±765.11	25446.83±732.22	23167.98±698.82
$(m_{W_R}, m_N) = (2.0, 1.8)\,\text{TeV}$	12136.50±511.48	1699.65±190.34	1570.83±182.89	825.92±132.55	783.17±129.05
$(m_{W_R}, m_N) = (6.5, 0.2)\,\text{TeV}$	53460.24±1077.06	20868.50±667.63	20841.46±667.09	18466.44±628.04	17537.55±612.14
$(m_{W_R}, m_N) = (6.5, 6.3)\,\text{TeV}$	28185.76±787.05	3248.06±264.21	2812.28±245.32	2518.49±232.36	2457.71±229.68
Fakes	1802.13±17.61	156.41±5.22	151.56±5.14	21.51±1.91	20.40±1.89
Top	129.72±2.79	33.97±1.33	33.61±1.32	4.65±0.52	3.63±0.46
Others	126.93±52.93	18.75±6.82	18.74±6.82	3.22±3.18	3.21±3.18
Total	2058.78±55.85	209.13±8.69	203.90±8.64	29.37±3.75	27.24±3.73
Data	1815	–	–	–	
Data/Prediction	0.88	–	–	–	

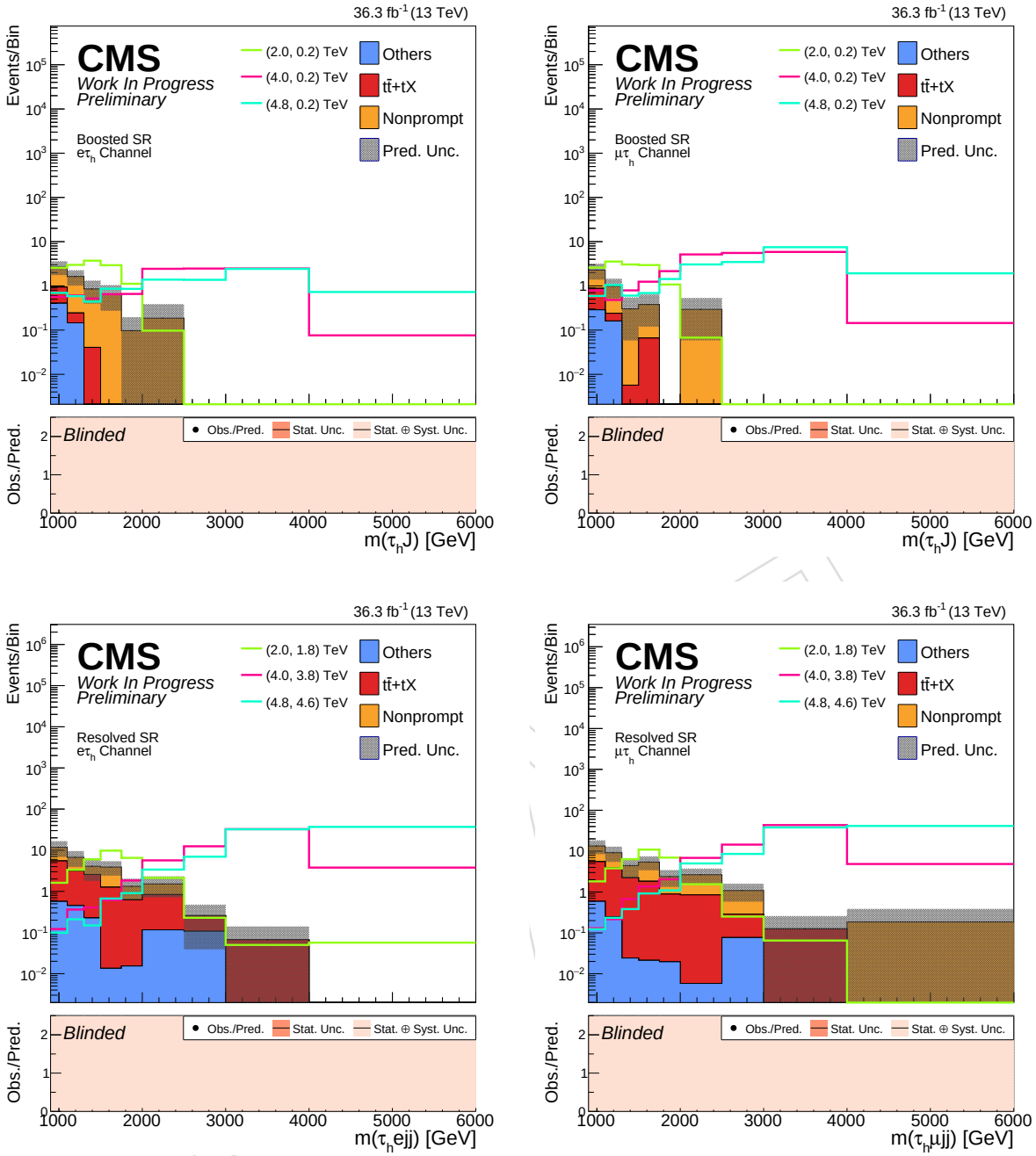

Figure 16: $m(\tau_h J)$ and $m(\tau_h \ell jj)$ in the signal region for 2016preVFP and 2016postVFP combined. Results for the electron (muon) channel are shown in the left (right) column, and for the boosted (resolved) channel in the upper (lower) column. Data points are blinded.

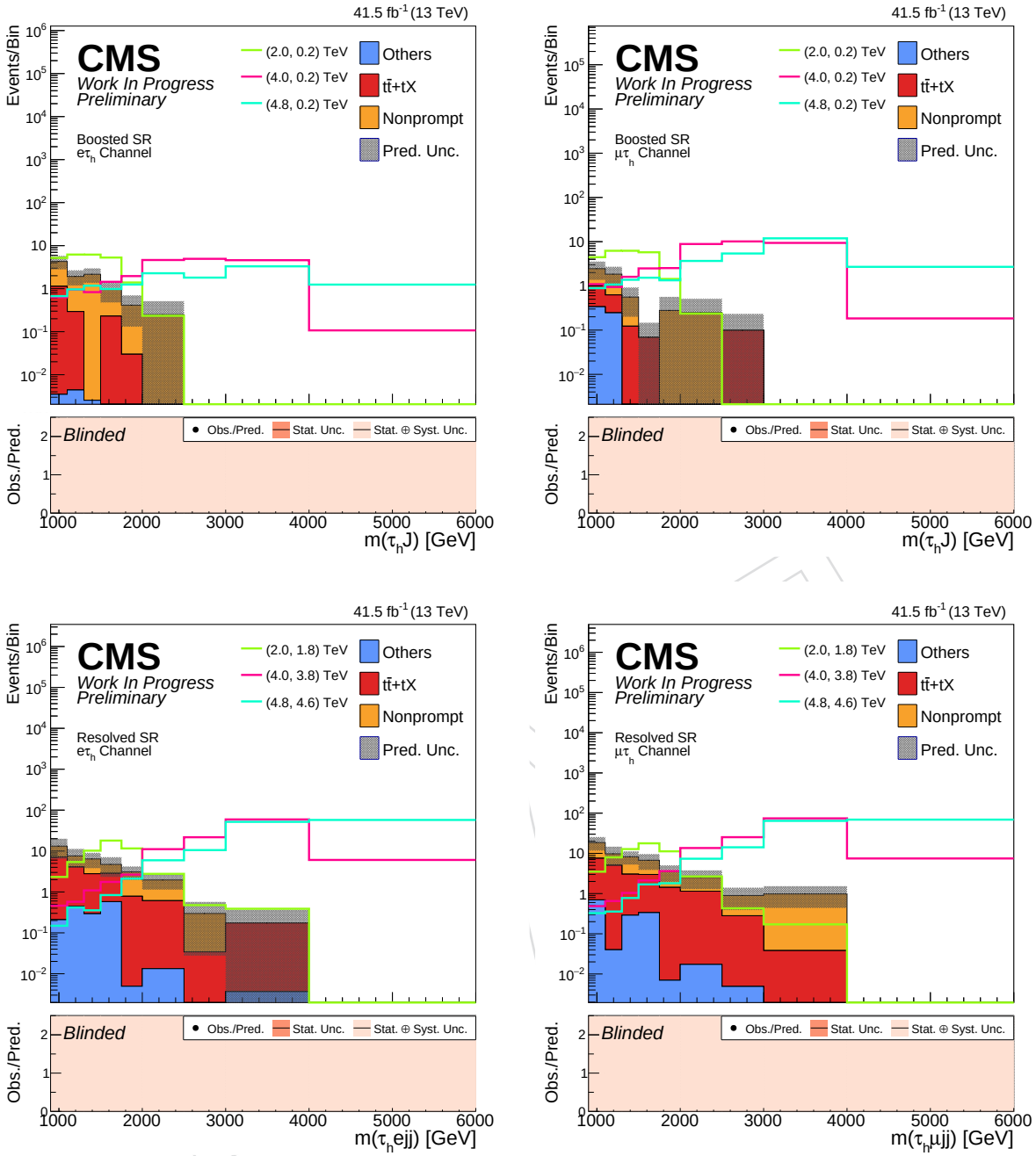

Figure 17: $m(\tau_h J)$ and $m(\tau_h \ell jj)$ in the signal region for 2017. Results for the electron (muon) channel are shown in the left (right) column, and for the boosted (resolved) channel in the upper (lower) column. Data points are blinded.

7 Background Estimation

7.1 Prompt Backgrounds

Backgrounds with a correctly identified real hadronic tau are directly taken from simulations listed in Table 4. The dominant background is the top pair and single top production. Boson production associated with jets is also a contributing factor, but it is highly suppressed.

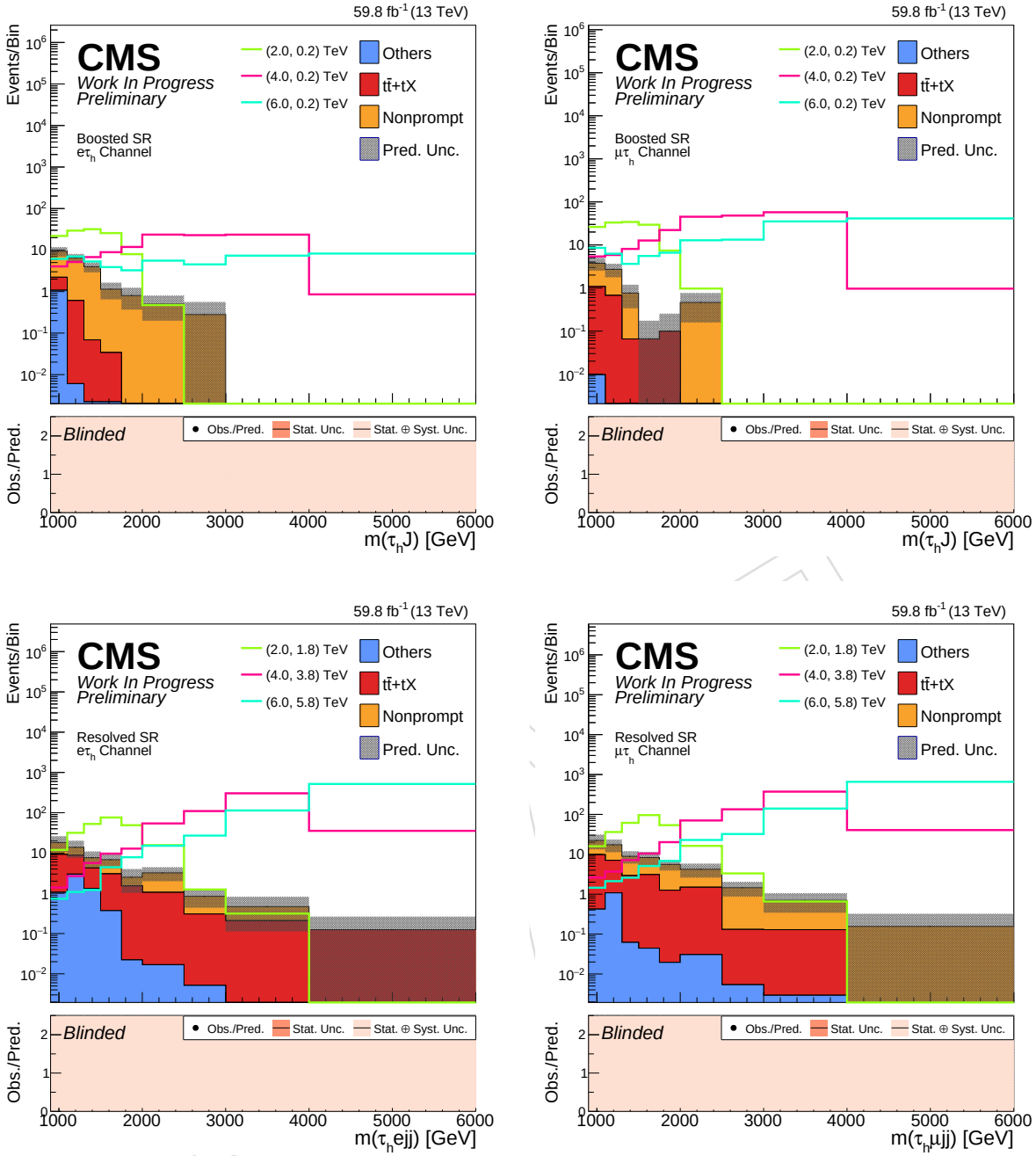

Figure 18: $m(\tau_h J)$ and $m(\tau_h \ell jj)$ in the signal region for 2018. Results for the electron (muon) channel are shown in the left (right) column, and for the boosted (resolved) channel in the upper (lower) column. Data points are blinded.

7.2 Nonprompt Backgrounds with jet $\rightarrow \tau_h$ misidentification

7.2.1 Fake Factor Method

The most dominant background originates from events having jets being misidentified as τ_h, mostly from QCD multijet events and an additional contribution from top pair events. Due to the inaccuracy of the simulation of such backgrounds, a data-driven method is utilized to measure such misidentification rates.

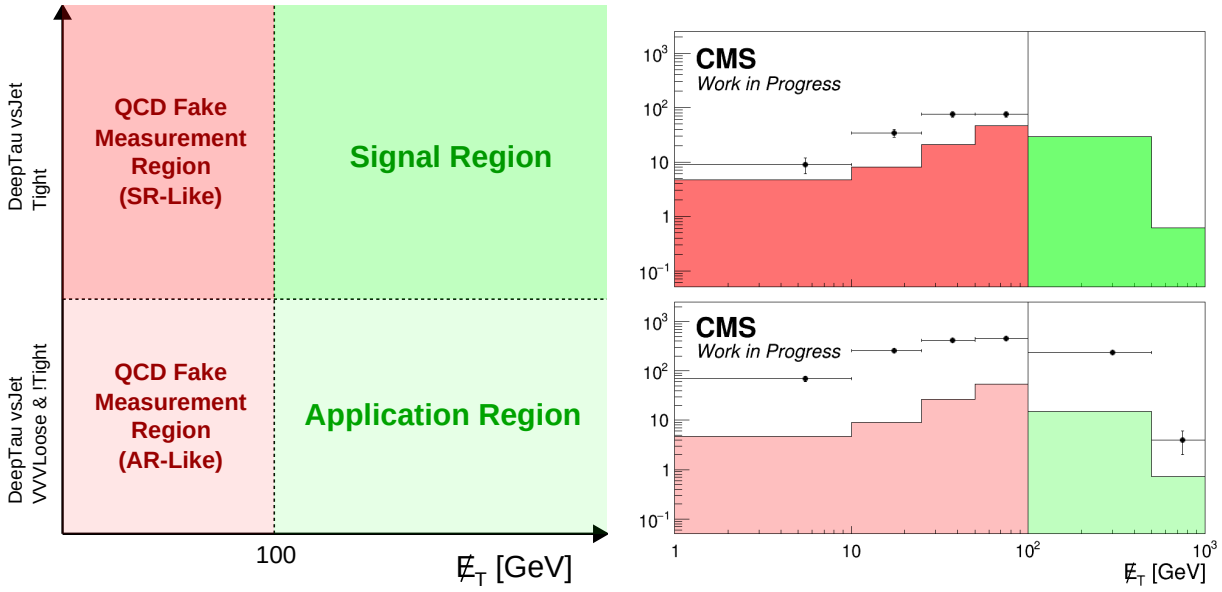

Figure 19: The left figure shows a schematic diagram depicting the QCD fake rate measurement region and its associated orthogonal regions cut by changing the DeepTau vsJet working point. The other figure shows the missing transverse energy distribution for each region, which is cut by the signal region cut value of 100 GeV, where the prompt backgrounds are shown as a filled histogram and data as points with the signal region blinded.

First is to measure the "fake factor", which will be denoted as FF_b where $b = \mathrm{QCD}, \mathrm{TT}$ which represents the fake background source (QCD, top pair). It is defined as the ratio of number of events with a jet passing the `VVVLoose` but not `Tight` DeepTau ID working point as a denominator and the numerator as the number of events with a jet passing the `Tight` working point as a function of the p_T and decay mode (DM) of the hadronic tau using the data for each era. To determine such factors for a particular background source, one needs to construct a sound measurement region (MR) which is orthogonal to the signal region and has the dominant contribution of the background source of interest. As described in Section 6, a QCD MR is defined by inverting the transverse momentum selection, shown in Fig. 19. FF_QCD can be then calculated in such QCD MR as :

$$\mathrm{FF}_\mathrm{QCD}(p_\mathrm{T}^{\tau_h}, \mathrm{DM}) = \frac{N_\mathrm{Data}^\mathrm{Tight}(p_\mathrm{T}^{\tau_h}, \mathrm{DM}) - N_\mathrm{Prompt\,MC}^\mathrm{Tight}(p_\mathrm{T}^{\tau_h}, \mathrm{DM})}{N_\mathrm{Data}^\mathrm{VVVLoose\,\cap\,!Tight}(p_\mathrm{T}^{\tau_h}, \mathrm{DM}) - N_\mathrm{Prompt\,MC}^\mathrm{VVVLoose\,\cap\,!Tight}(p_\mathrm{T}^{\tau_h}, \mathrm{DM})} \tag{3}$$

Note that while deriving FF_QCD, prompt contributions are subtracted to properly extract only the QCD-like fake contribution. The derived FF_QCD values as a function of hadronic tau p_T can be seen in Fig. **??**, while for individual eras plotted separately are shown in Fig. 67 – 69.

Meanwhile, for top pair contributions, no suitable measurement region was available thus, only simulation labeled as $\mathrm{t\bar{t}}$+X in Table 4 was used in the measurement of FF_TT which can be expressed as :

$$\mathrm{FF}_\mathrm{TT}(p_\mathrm{T}^{\tau_h}, \mathrm{DM}) = \frac{N_\mathrm{Nonprompt\,TT\,MC}^\mathrm{Tight}(p_\mathrm{T}^{\tau_h}, \mathrm{DM})}{N_\mathrm{Nonprompt\,TT\,MC}^\mathrm{VVVLoose\,\cap\,!Tight}(p_\mathrm{T}^{\tau_h}, \mathrm{DM})} \tag{4}$$

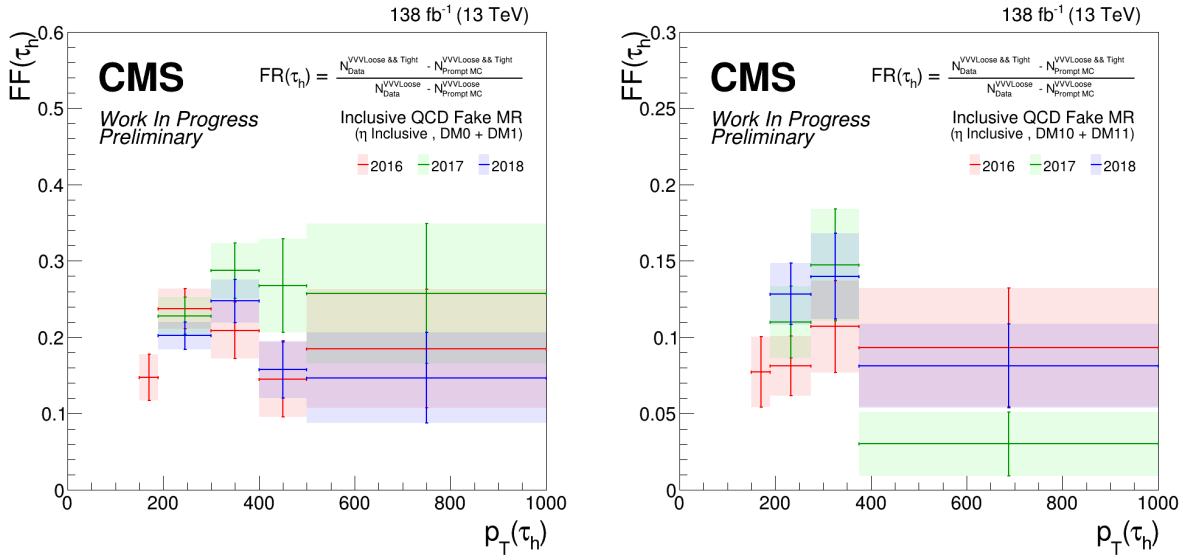

Figure 20: $\mathrm{FF}_{\mathrm{QCD}}$ derived in terms of hadronic tau p_{T} for all UL eras shown in the left (right) side as a single plot for 1 prong (3 prong) decay modes.

The derived $\mathrm{FF}_{\mathrm{TT}}$ for each UL era as a function of the hadronic tau p_{T} for each decay mode are shown in Fig. 64 – 66, while inclusively shown in Fig. 21 in terms of eras.

The FF_b values are subsequently used for each event as a weighted sum in what is known as the application region (AR). The AR is distinct from the signal region, requiring the hadronic tau to pass the `VVVLoose` but fail the `Tight` DeepTau2017v2p1VSjet working point. The weights assigned to each FF component are referred to as fractions denoted as f_b, indicating the probability of the event corresponding to a specific background process. The entire fake factor would then be expressed as Eq. 5 :

$$\mathrm{FF} = \sum_{b \in \{\mathrm{QCD,TT}\}} f_b \mathrm{FF}_b = f_{\mathrm{QCD}} \mathrm{FF}_{\mathrm{QCD}} + f_{\mathrm{TT}} \mathrm{FF}_{\mathrm{TT}} \tag{5}$$

Such f_b for each background source b is derived in the AR by simply calculating the non-normalized ratio f'_b :

$$f'_b = \frac{N_b^{\mathrm{AR}}}{N_{\mathrm{Data}}^{\mathrm{AR}}} \tag{6}$$

Where N_b^{AR} is the number of nonprompt MC events in the AR with a source of b. For backgrounds which are non-QCD, N_b^{AR} is simply the nonprompt MC events, while for QCD, it is calculated as,

$$N_{\mathrm{QCD}} = \max\left(0, N_{\mathrm{Data}}^{\mathrm{AR}} - N_{\mathrm{Prompt\,MC}}^{\mathrm{AR}} - N_{\mathrm{TT}}^{\mathrm{AR}}\right) \tag{7}$$

Where $N_{\mathrm{Prompt\,MC}}^{\mathrm{AR}}$ is the number of prompt MC events in the AR. In order to make f_b normalized, i.e $\sum_b f_b = 1$ one could normalize f'_b as

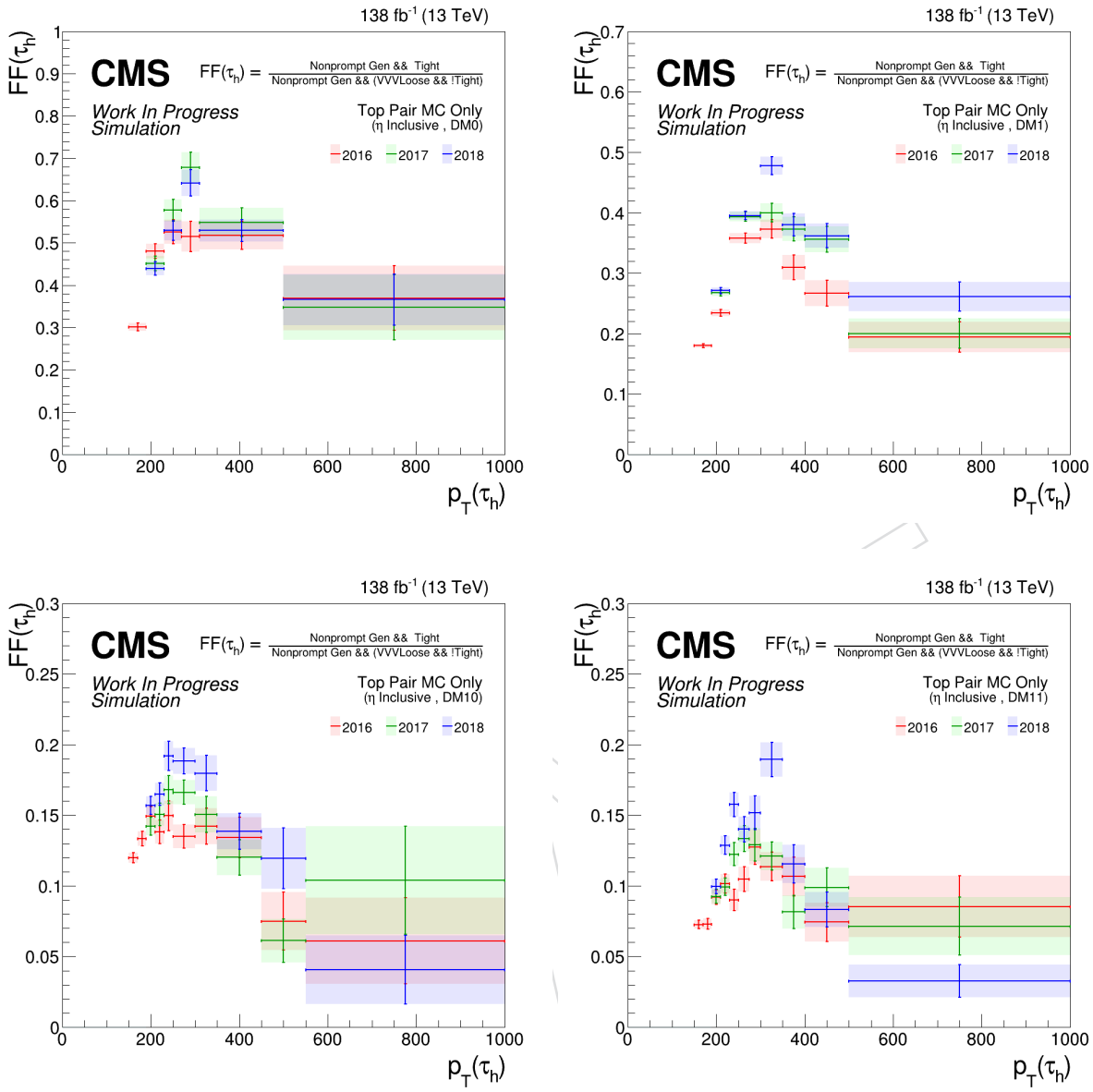

Figure 21: $\mathrm{FF_{TT}}$ derived in terms of hadronic tau p_T for all UL eras shown in a single plot for each decay mode.

$$f_b \equiv \frac{1}{\sum_b f'_b} \times f'_b \tag{8}$$

f_b could be parameterized with any variable of interest, and in this analysis p_T of the hadronic tau and m_Eff is used which is shown in Fig. 23 – 25 and Fig. 71 – 73 respectively.

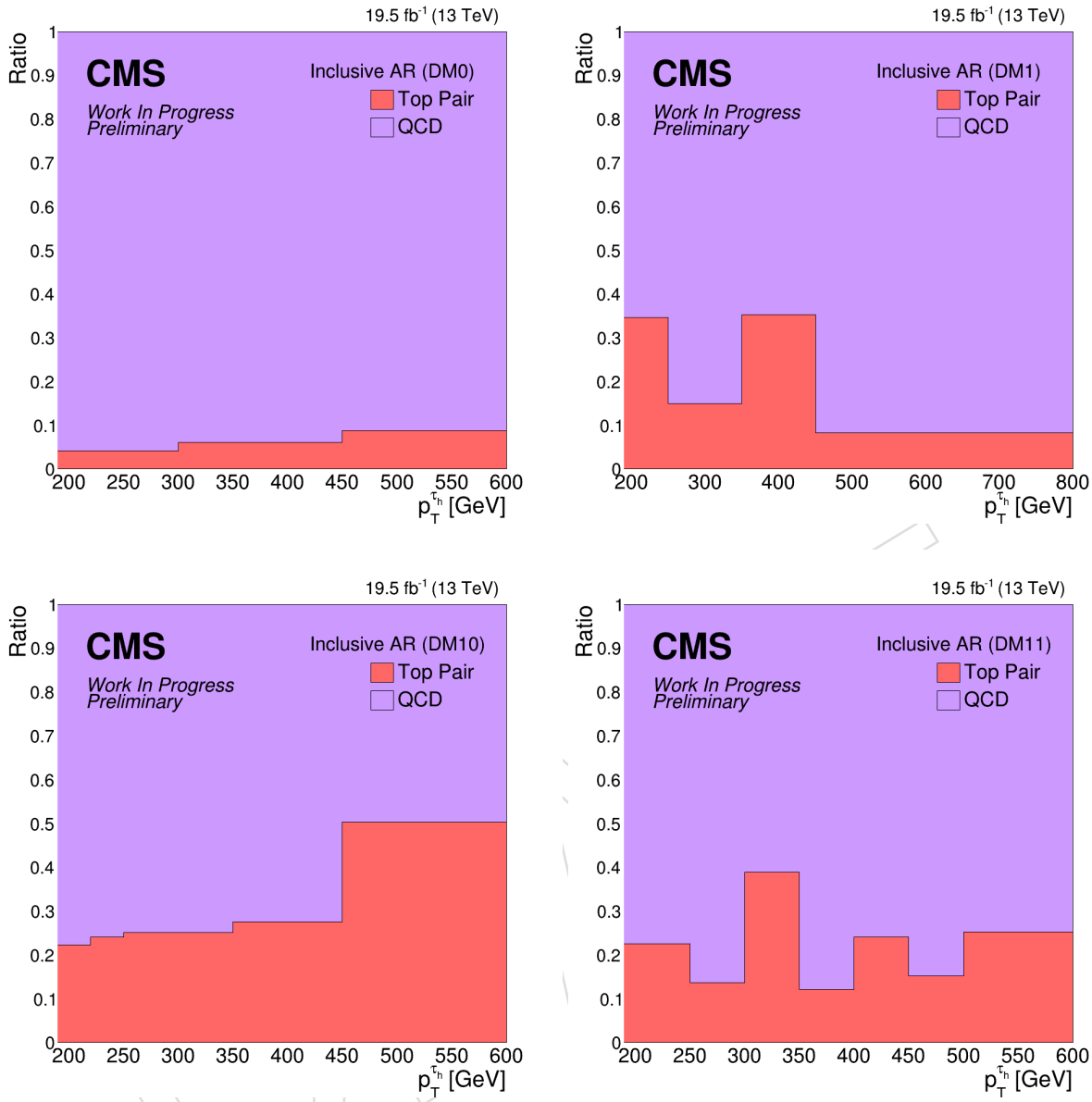

Figure 22: Fractions of the hadronic tau misidentification backgrounds as a function of hadronic tau p_{T}, divided by the hadronic tau decay modes used in this analysis in the Run2 UL 2016pre-VFP era.

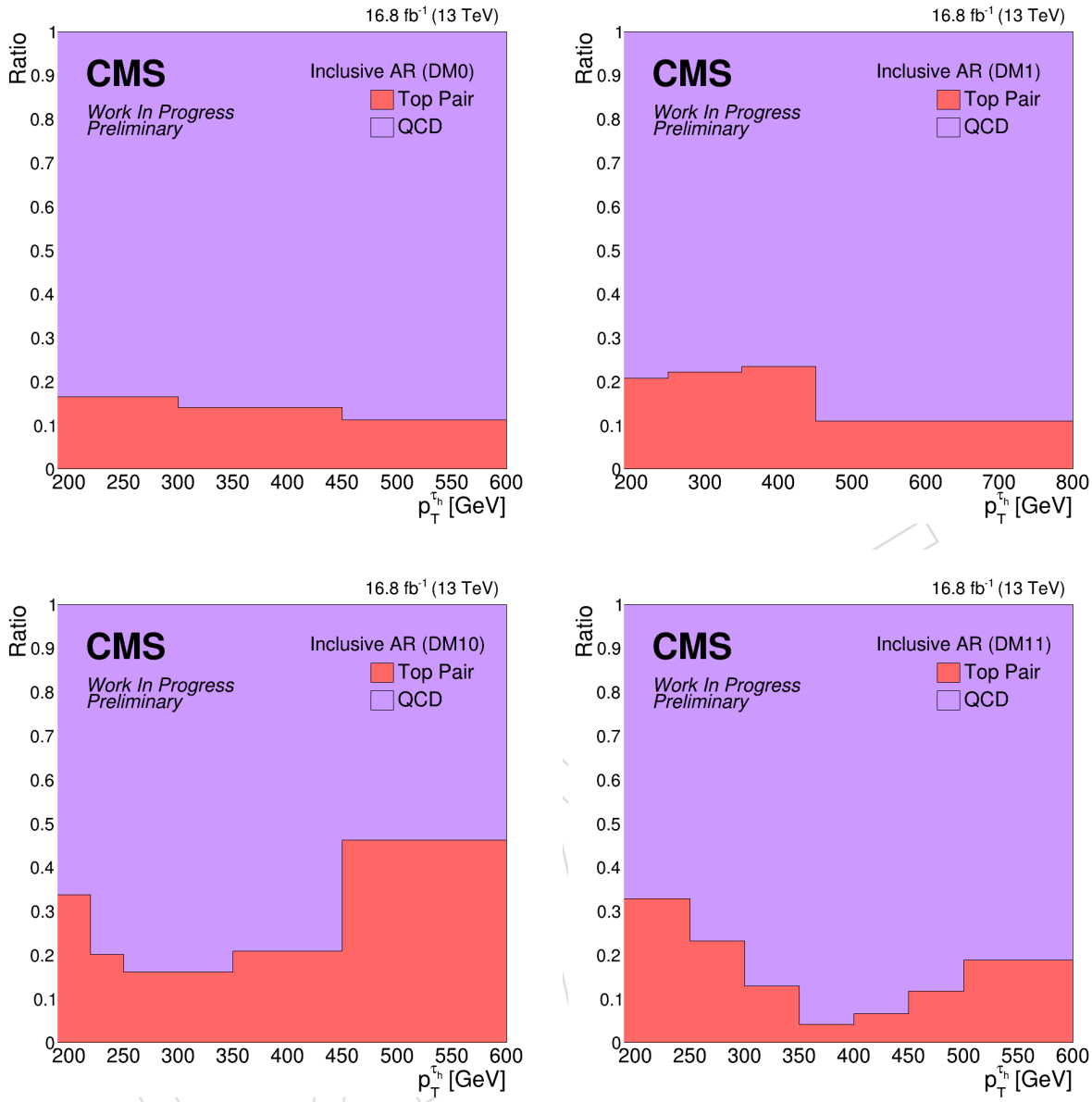

Figure 23: Fractions of the hadronic tau misidentification backgrounds as a function of hadronic tau p_T, divided by the hadronic tau decay modes used in this analysis in the Run2 UL 2016postVFP era.

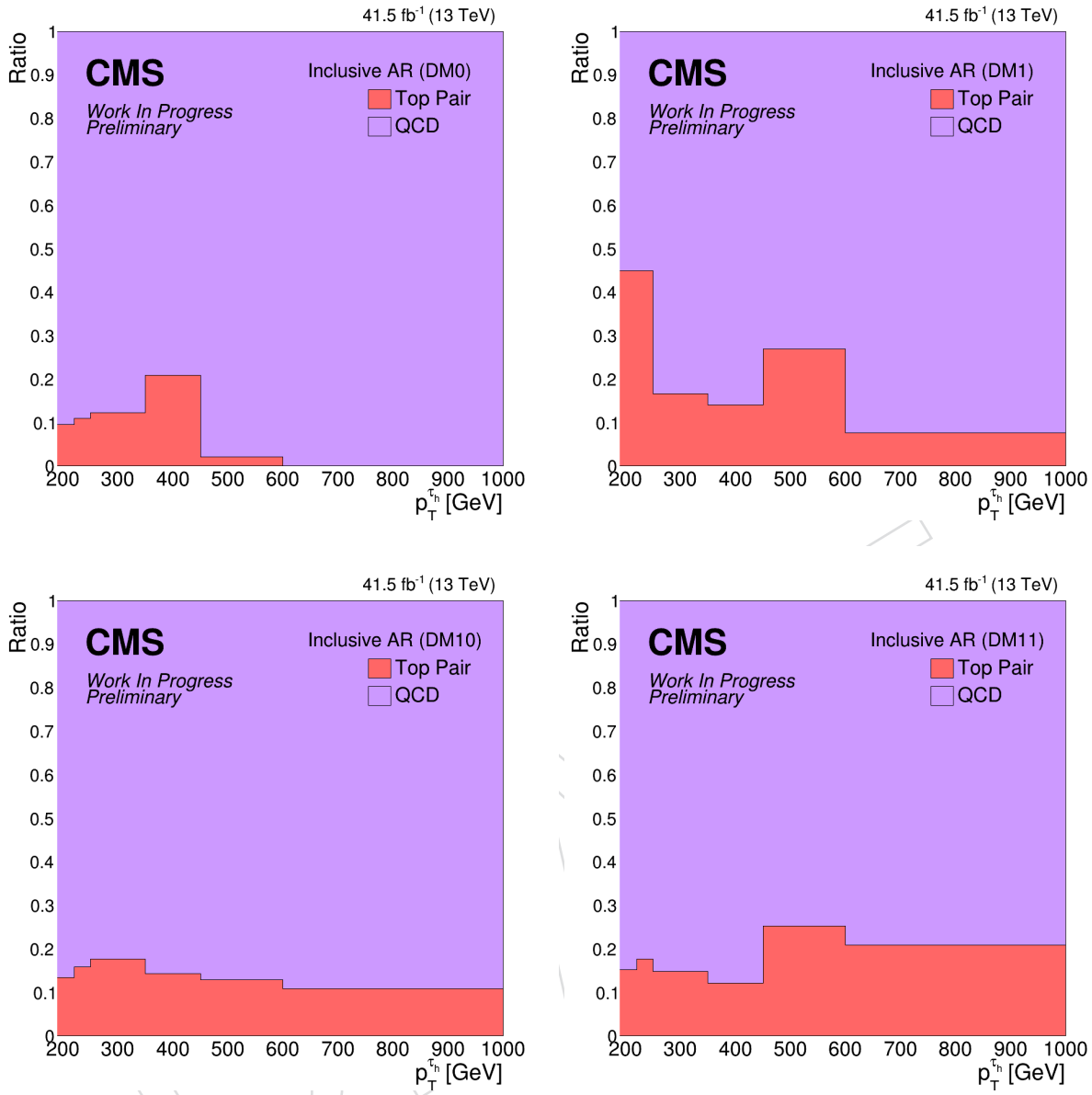

Figure 24: Fractions of the hadronic tau misidentification backgrounds as a function of hadronic tau p_{T}, divided by the hadronic tau decay modes used in this analysis in the Run2 UL 2017 era.

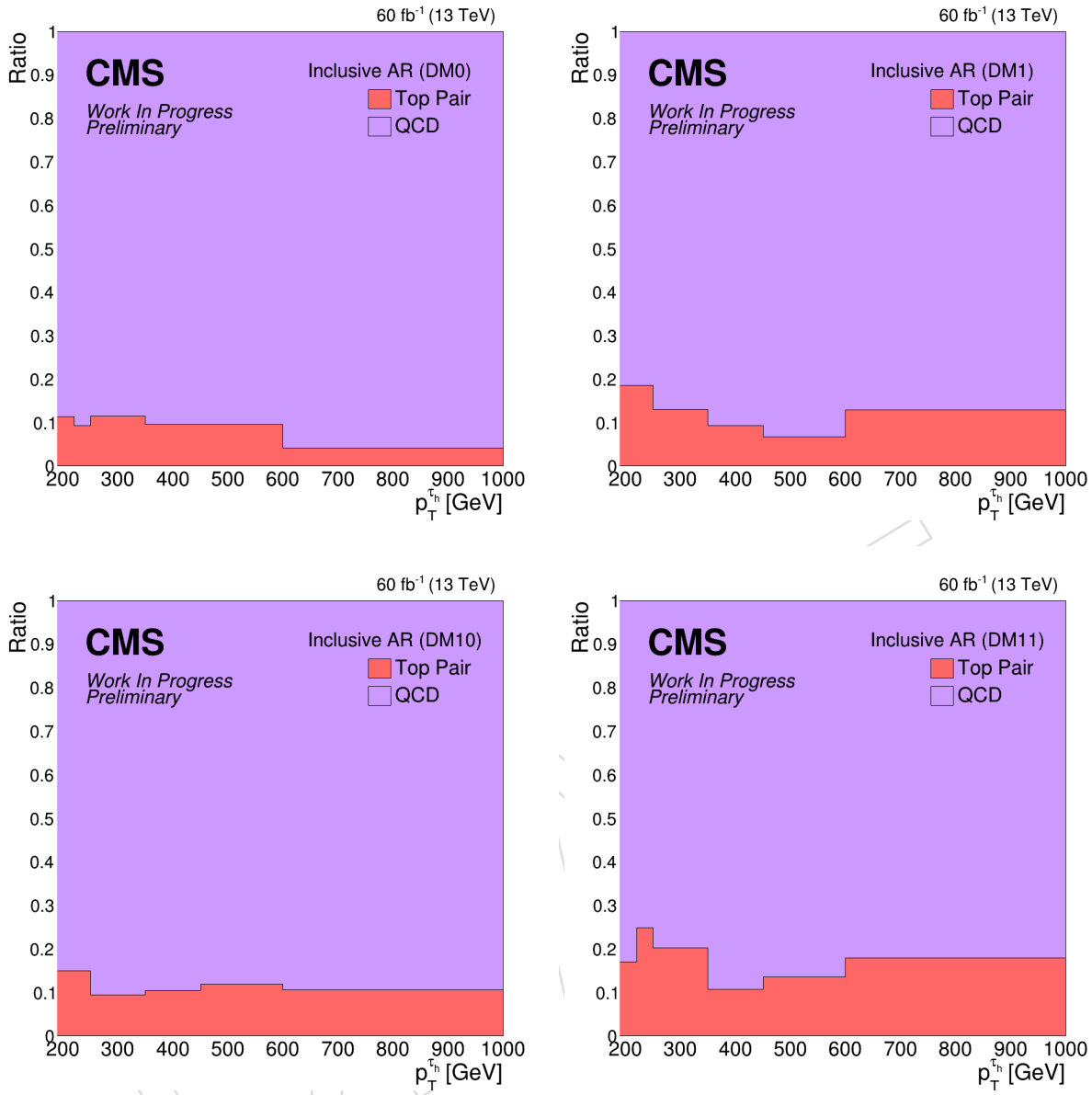

Figure 25: Fractions of the hadronic tau misidentification backgrounds as a function of hadronic tau p_T, divided by the hadronic tau decay modes used in this analysis in the Run2 UL 2018 era.

7.2.2 Closure Validation

Validation of the fake method can be checked in the closure region for each fake factor source. As FF_{QCD} is derived in the designated QCD Fake MR, itself could be used as a closure region, while for FF_{TT}, which did not have a particular MR but used simulation only to estimate, the. Fig 26 – 28 shows the overall closure agreement in the QCD fake MR. Upon these, a 30% normalization uncertainty for data driven nonprompt contributions is given.

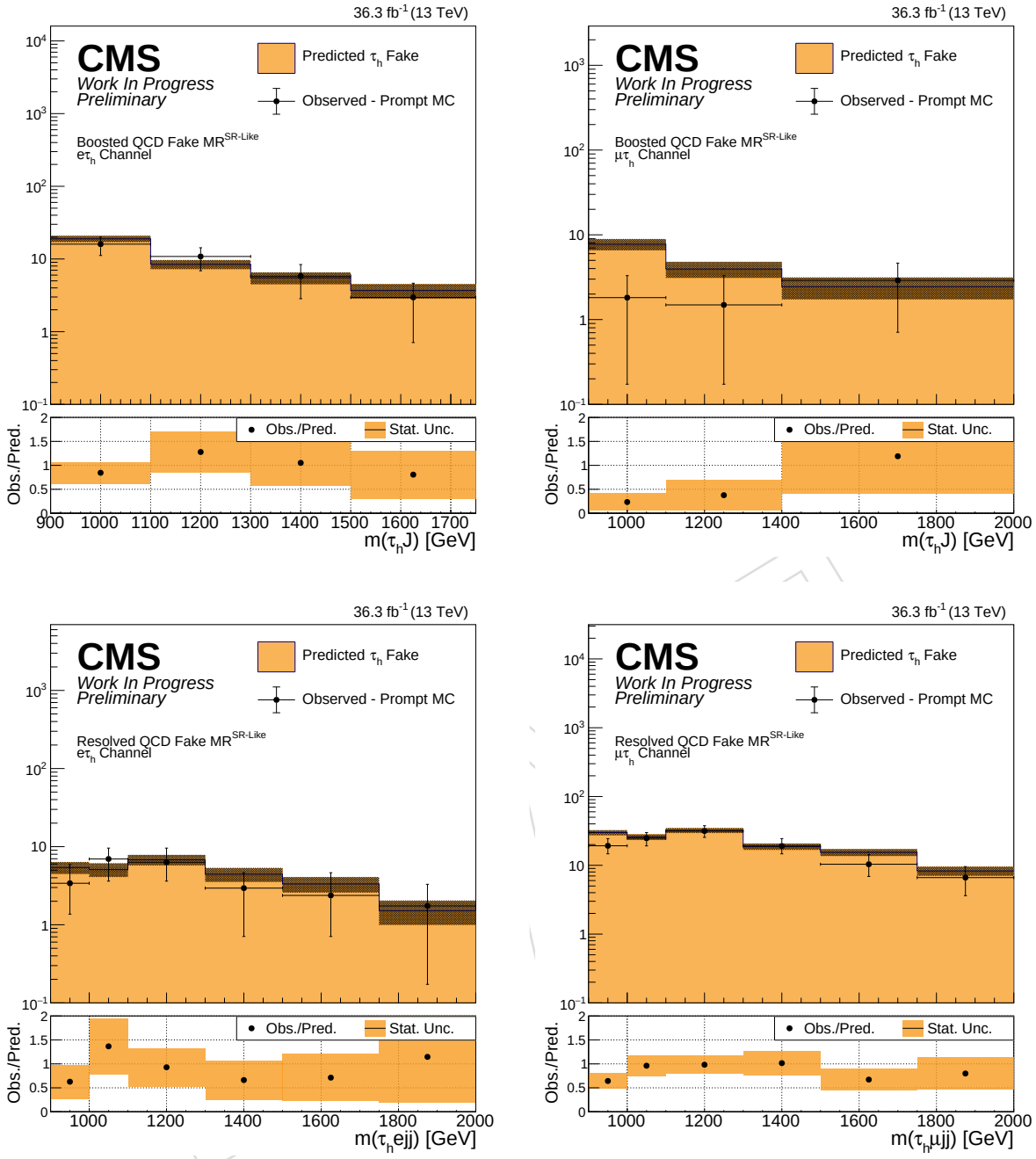

Figure 26: Closure plots in the QCD Fake MR for 2016preVFP and 2016postVFP data merged for the electron (muon) channel in the left (right) column, boosted (resolved) channel in the upper (lower) column.

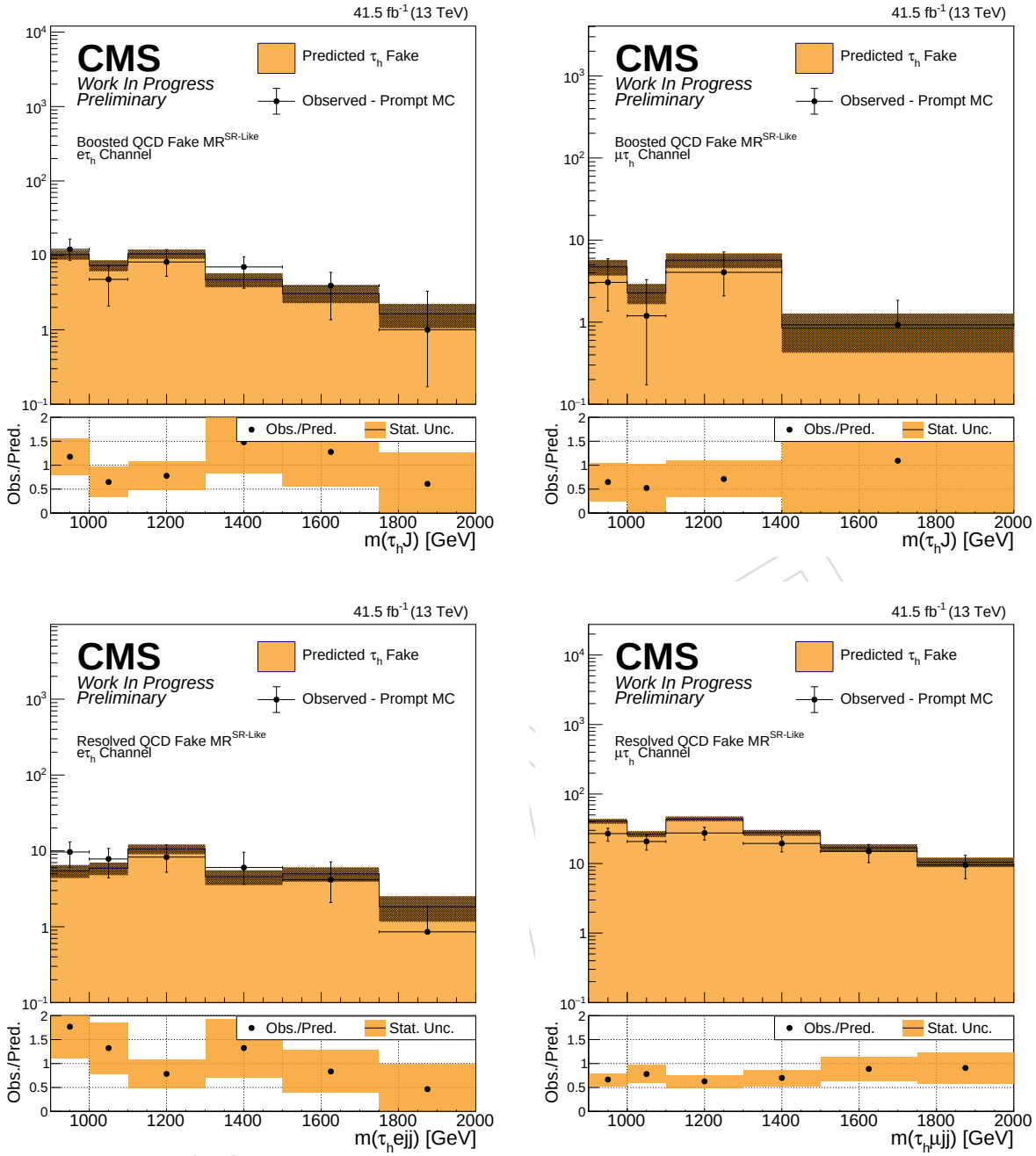

Figure 27: Closure plots in the QCD Fake MR for 2017 data for the electron (muon) channel in the left (right) column, boosted (resolved) channel in the upper (lower) column.

8 Systematic Uncertainties

Several systematic uncertainties are considered in this analysis, which is also summarized in Table 22.

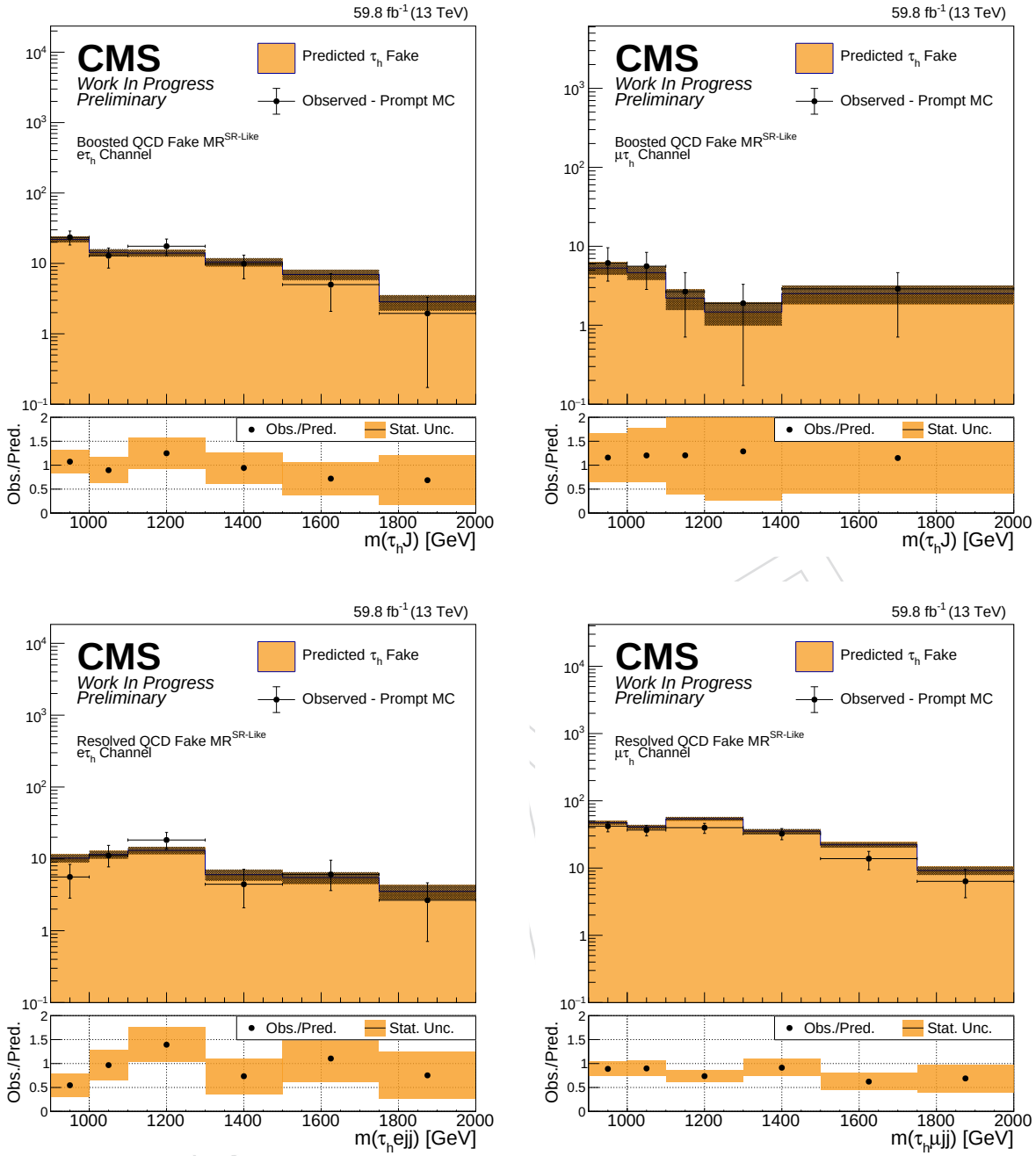

Figure 28: Closure plots in the QCD Fake MR for 2018 data for the electron (muon) channel in the left (right) column, boosted (resolved) channel in the upper (lower) column.

8.1 Object reconstruction uncertainties

8.1.1 Hadronic Taus

- **Tau ID uncertainty** The propagation of the uncertainty in the hadronic tau identification follows the recommendation of the Tau POG. In the case of high p_T hadronic taus with $p_T > 140\,\text{GeV}$, a different uncertainty scheme is applied, which also follows the POG recommendation.
- **Tau energy scale (TES)** The energy scale of a genuine hadronic tau is corrected by the decay mode and era, which ranges between 0.7% to 1.2%, following the recom-

Table 22: Summarized table of systematic uncertainties that are taken account to in this analysis. For each uncertainty sources, the type, magnitude, processes that it applies to, and era correlation are shown.

Uncertainty source		Type	Magnitude	Processes	Era correlation
Luminosity		norm.	$1-2.5\%$	All Simulations	
Hadronic Tau	ID.	shape	–	All Simulations	
	Trigger	norm.	$8-11\%$	All Simulations	
	Energy Scale	shape	–	All Simulations	
	FF Stat.	shape	–	Nonprompts	
	FF Norm.	norm.	30%	Nonprompts	
Jet	Energy Scale	shape	–	All Simulations	
Theory	PDF	shape.	–	Signals	
	μ_R, μ_F	shape	–	Signals	

mendation of the Tau POG.

8.1.2 Jets

- **Jet energy scale (JES)** The merged uncertainty scheme recommended by the JetMET POG is used, which takes into account a series of JES uncertainties. Jets in simulations are also smeared to agree with the jet energy resolution in data. Uncertainties stemming from such smearing are included as a shape uncertainty.

8.2 Theoretical Uncertainties

- μ_R **and** μ_F **scale uncertainty**: Renormalization and factorization scale uncertainties are derived by enveloping over all possible combinations of variations of $\mu_R = 0.5, 1.0, 2.0$ and $\mu_F = 0.5, 1.0, 2.0$ with the two extreme combinations $(\mu_R, \mu_F) = 0.5, 2.0$ and $2.0, 0.5$ removed.
- **PDF uncertainty**: Following the recommendations of the PDF4LHC collaboration [31], uncertainties in the PDFs are calculated bin-by-bin from the uncertainty in the correction by varying PDF member sets.

8.3 Background estimation uncertainties

- **Tau fake factor statistical uncertainty**: The statistical uncertainty from the fake estimation method is introduced as a shape uncertainty for the data-driven fake estimations.
- **Normalization uncertainty**: From the closure validation, a flat normalization uncertainty of 30% will only be given for the data-driven fake estimations.

8.4 Other uncertainties

- **Integrated luminosity**: Following the Lumi POG recommendations, luminosity uncertainty is given era by era.
- **Tau trigger scale factor**: For the single tau trigger used in this analysis, TAU POG provided the uncertainty between 8 to 1% depending on the year with no dependency on other variables.

- **MC statistics**: A bin-by-bin statistical uncertainty is considered to take into account the limited statistics available in our MC samples. The Barlow-Beeston approach uses a single nuisance parameter in each bin to scale the sum of the process yields.

8.5 Impacts

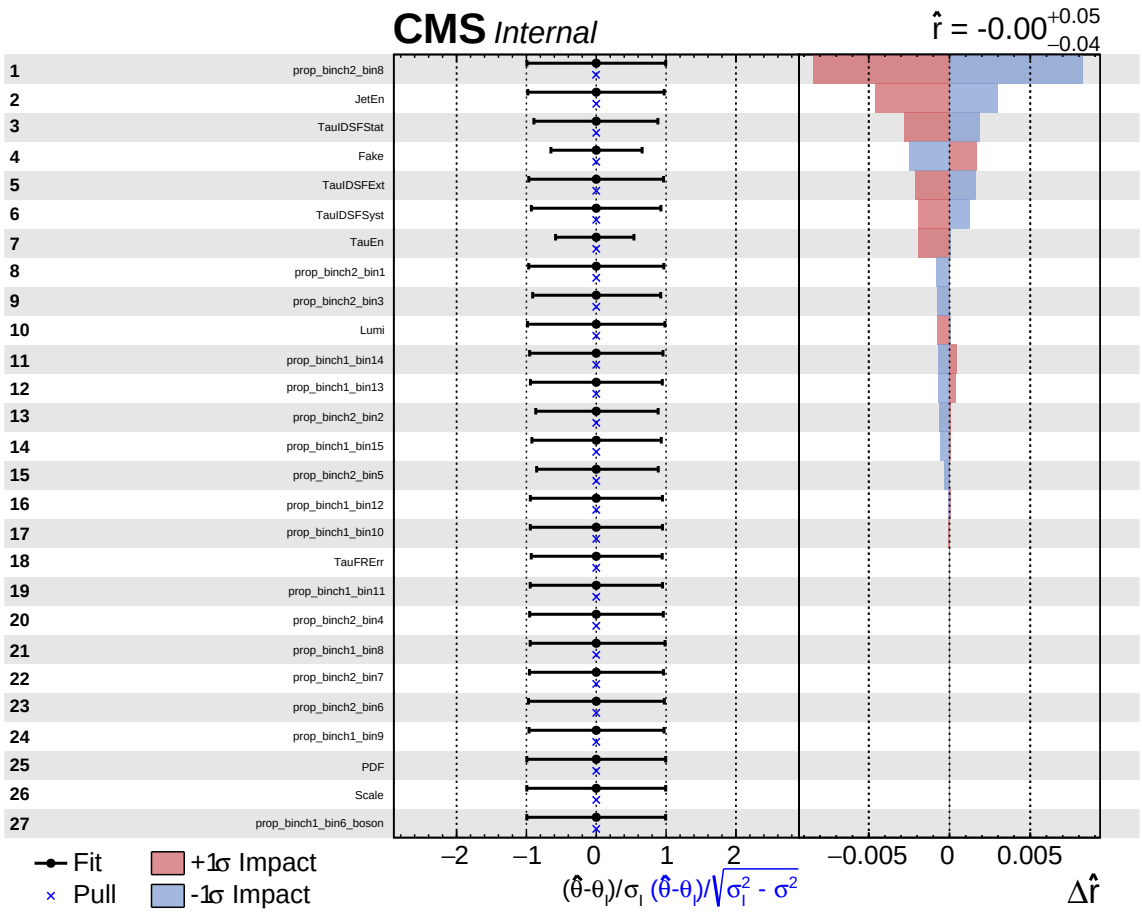

Figure 29: Pull and impacts for systematic sources from the background only fitting using the Asimov dataset for 2018 prediction.

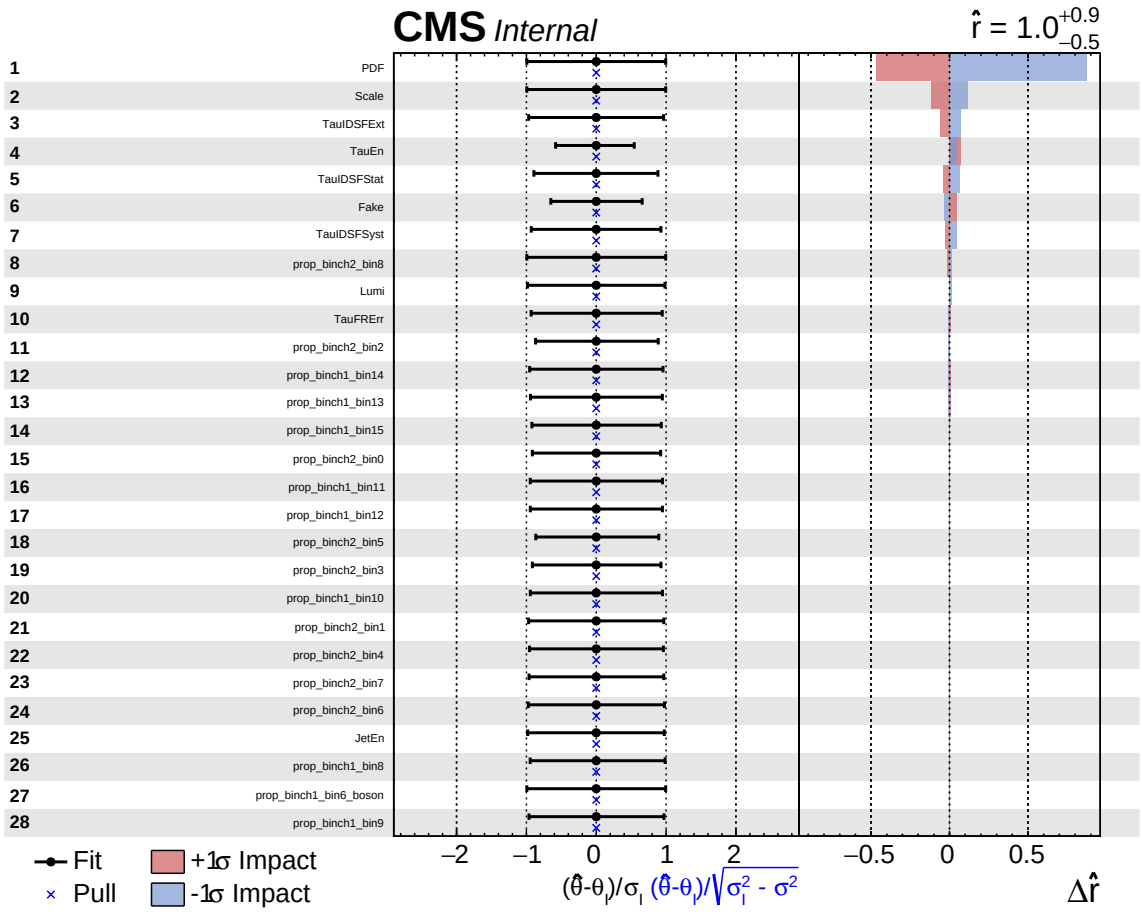

Figure 30: Pull and impacts for systematic sources with injecting a signal of $m(W_R) = 4.5\,\text{TeV}, m(N) = 4.0\,\text{TeV}$ with setting the signal strength r to 1.0 using Asimov dataset for 2018 prediction.

9 Results

The expected and upper limit of signal strength is calculated with Combine [32] in each year. Limits are calculated using the binned shape method with the reconstructed W_R mass as the input where the signal strength is floating as a free parameter while the systematic uncertainties described in Section 8 are introduced as nuisance parameters.

9.1 Expected Limits

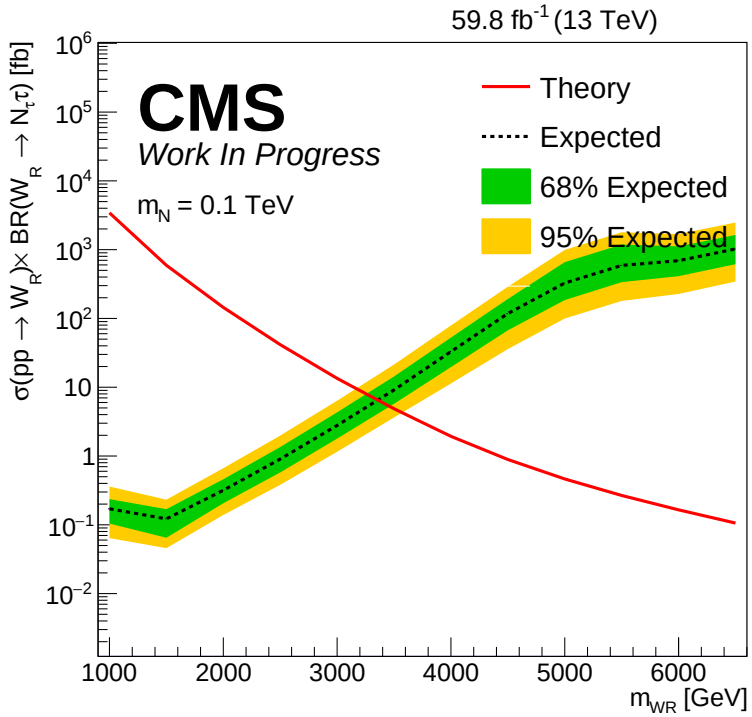

Figure 31: Expected limit at 95% CL in the $m(N) = 0.1\,\text{TeV}$ scenario on the $\sigma\,(pp \to W_R) \times \text{BR}\,(W_R \to N\tau)$ with respect to different $m(W_R)$ hypotheses for inclusive signal regions for 2018.

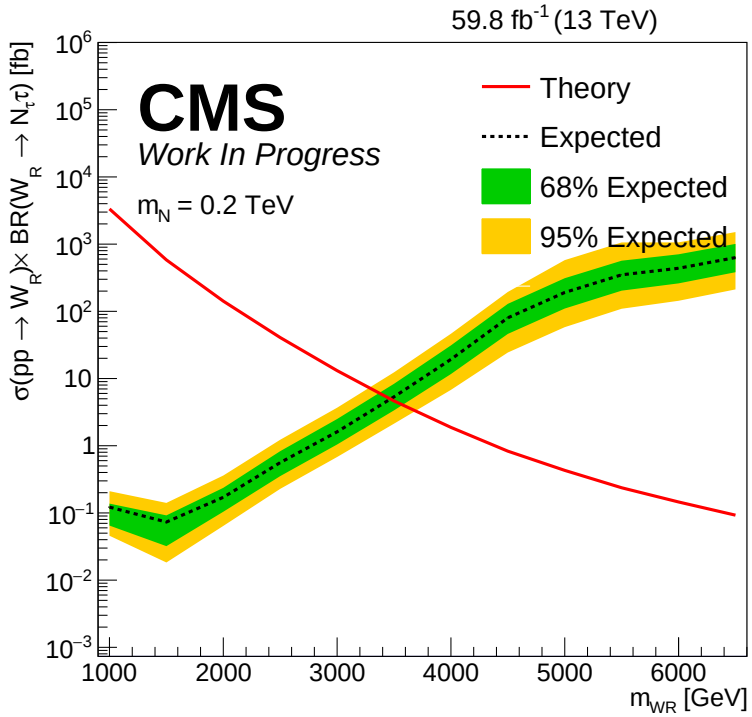

Figure 32: Expected limit at 95% CL in the $m(N) = 0.2\,\text{TeV}$ scenario on the $\sigma(pp \to W_R) \times \text{BR}(W_R \to N\tau)$ with respect to different $m(W_R)$ hypotheses for inclusive signal regions for 2018

10 Conclusion

A search for W_R boson decaying into a heavy neutral lepton N has been performed in a light lepton, hadronic tau and jets final state using data collected by the CMS detector in Run 2. This search has improved the upper limit of the signal cross section, especially in the boosted region where $m(W_R) \gg m(N)$.

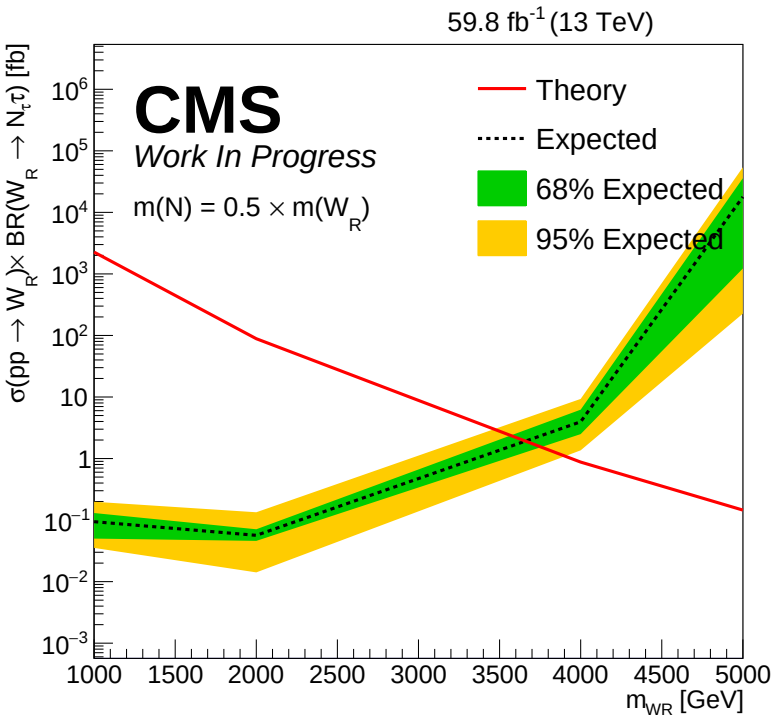

Figure 33: Expected limit at 95% CL in the $m(N) = 0.5 \times m(W_R)$ scenario on the $\sigma\,(pp \to W_R) \times \mathrm{BR}\,(W_R \to N\tau)$ with respect to different $m(W_R)$ hypotheses for inclusive signal regions for 2018

A Signal Sample

A.1 Cross Section

Table 23: Cross section of produced signal samplesSample Name

$\sigma(pb)$ LO	$k^{\mathrm{NLO/LO}}$	
WRTau_WR1000_N100	0.88×10^1	-
WRTau_WR1000_N200	0.83×10^1	-
WRTau_WR1000_N300	0.77×10^1	-
WRTau_WR1000_N400	0.69×10^1	-
WRTau_WR1000_N500	0.59×10^1	-
WRTau_WR1000_N600	0.47×10^1	-
WRTau_WR1000_N700	0.33×10^1	-
WRTau_WR1000_N800	0.18×10^1	-
WRTau_WR1000_N900	0.60	-
WRTau_WR1200_N1000	0.63	-
WRTau_WR1200_N100	0.41×10^1	-
WRTau_WR1200_N1100	0.21	-
WRTau_WR1200_N200	0.39×10^1	-
WRTau_WR1200_N300	0.37×10^1	-
WRTau_WR1200_N400	0.35×10^1	-
WRTau_WR1200_N500	0.31×10^1	-
WRTau_WR1200_N600	0.27×10^1	-
WRTau_WR1200_N700	0.23×10^1	-
WRTau_WR1200_N800	0.17×10^1	-

WRTau_WR1200_N900	0.12×10^{1}	-
WRTau_WR1400_N1000	0.70	-
WRTau_WR1400_N100	0.21×10^{1}	-
WRTau_WR1400_N1100	0.47	-
WRTau_WR1400_N1200	0.25	-
WRTau_WR1400_N1300	0.81×10^{-1}	-
WRTau_WR1400_N200	0.20×10^{1}	-
WRTau_WR1400_N300	0.19×10^{1}	-
WRTau_WR1400_N400	0.18×10^{1}	-
WRTau_WR1400_N500	0.17×10^{1}	-
WRTau_WR1400_N600	0.16×10^{1}	-
WRTau_WR1400_N700	0.14×10^{1}	-
WRTau_WR1400_N800	0.12×10^{1}	-
WRTau_WR1400_N900	0.95	-
WRTau_WR1600_N1000	0.54	-
WRTau_WR1600_N100	0.11×10^{1}	-
WRTau_WR1600_N1100	0.42	-
WRTau_WR1600_N1200	0.31	-
WRTau_WR1600_N1300	0.20	-
WRTau_WR1600_N1400	0.10	-
WRTau_WR1600_N1500	0.35×10^{-1}	-
WRTau_WR1600_N200	0.11×10^{1}	-
WRTau_WR1600_N300	0.10×10^{1}	-
WRTau_WR1600_N400	0.10×10^{1}	-
WRTau_WR1600_N500	0.95	-
WRTau_WR1600_N600	0.89	-
WRTau_WR1600_N700	0.81	-
WRTau_WR1600_N800	0.73	-
WRTau_WR1600_N900	0.64	-
WRTau_WR1800_N1000	0.36	-
WRTau_WR1800_N100	0.63	-
WRTau_WR1800_N1100	0.31	-
WRTau_WR1800_N1200	0.26	-
WRTau_WR1800_N1300	0.20	-
WRTau_WR1800_N1400	0.14	-
WRTau_WR1800_N1500	0.93×10^{-1}	-
WRTau_WR1800_N1600	0.47×10^{-1}	-
WRTau_WR1800_N1700	0.16×10^{-1}	-
WRTau_WR1800_N200	0.62	-
WRTau_WR1800_N300	0.59	-
WRTau_WR1800_N400	0.57	-
WRTau_WR1800_N500	0.55	-
WRTau_WR1800_N600	0.52	-
WRTau_WR1800_N700	0.49	-
WRTau_WR1800_N800	0.45	-
WRTau_WR1800_N900	0.41	-
WRTau_WR2000_N1000	0.23	-
WRTau_WR2000_N100	0.37	-
WRTau_WR2000_N1100	0.21	-

WRTau_WR2000_N1200	0.18	-
WRTau_WR2000_N1300	0.16	-
WRTau_WR2000_N1400	0.13	-
WRTau_WR2000_N1500	0.99×10^{-1}	-
WRTau_WR2000_N1600	0.70×10^{-1}	-
WRTau_WR2000_N1700	0.45×10^{-1}	-
WRTau_WR2000_N1800	0.23×10^{-1}	-
WRTau_WR2000_N1900	0.78×10^{-2}	-
WRTau_WR2000_N200	0.36	-
WRTau_WR2000_N300	0.34	-
WRTau_WR2000_N400	0.34	-
WRTau_WR2000_N500	0.33	-
WRTau_WR2000_N600	0.31	-
WRTau_WR2000_N700	0.29	-
WRTau_WR2000_N800	0.27	-
WRTau_WR2000_N900	0.26	-
WRTau_WR2200_N1000	0.15	-
WRTau_WR2200_N100	0.22	-
WRTau_WR2200_N1100	0.14	-
WRTau_WR2200_N1200	0.12	-
WRTau_WR2200_N1300	0.11	-
WRTau_WR2200_N1400	0.97×10^{-1}	-
WRTau_WR2200_N1500	0.81×10^{-1}	-
WRTau_WR2200_N1600	0.66×10^{-1}	-
WRTau_WR2200_N1700	0.50×10^{-1}	-
WRTau_WR2200_N1800	0.35×10^{-1}	-
WRTau_WR2200_N1900	0.22×10^{-1}	-
WRTau_WR2200_N2000	0.11×10^{-1}	-
WRTau_WR2200_N200	0.21	-
WRTau_WR2200_N2100	0.39×10^{-2}	-
WRTau_WR2200_N300	0.21	-
WRTau_WR2200_N400	0.20	-
WRTau_WR2200_N500	0.19	-
WRTau_WR2200_N600	0.19	-
WRTau_WR2200_N700	0.18	-
WRTau_WR2200_N800	0.17	-
WRTau_WR2200_N900	0.16	-
WRTau_WR2400_N1000	0.97×10^{-1}	-
WRTau_WR2400_N100	0.13	-
WRTau_WR2400_N1100	0.90×10^{-1}	-
WRTau_WR2400_N1200	0.83×10^{-1}	-
WRTau_WR2400_N1300	0.76×10^{-1}	-
WRTau_WR2400_N1400	0.68×10^{-1}	-
WRTau_WR2400_N1500	0.60×10^{-1}	-
WRTau_WR2400_N1600	0.52×10^{-1}	-
WRTau_WR2400_N1700	0.43×10^{-1}	-
WRTau_WR2400_N1800	0.35×10^{-1}	-
WRTau_WR2400_N1900	0.26×10^{-1}	-
WRTau_WR2400_N2000	0.18×10^{-1}	-

WRTau_WR2400_N200	0.13	-
WRTau_WR2400_N2100	0.11×10^{-1}	-
WRTau_WR2400_N2200	0.58×10^{-2}	-
WRTau_WR2400_N2300	0.21×10^{-2}	-
WRTau_WR2400_N300	0.13	-
WRTau_WR2400_N400	0.12	-
WRTau_WR2400_N500	0.12	-
WRTau_WR2400_N600	0.12	-
WRTau_WR2400_N700	0.11	-
WRTau_WR2400_N800	0.11	-
WRTau_WR2400_N900	0.10	-
WRTau_WR2600_N1000	0.62×10^{-1}	-
WRTau_WR2600_N100	0.84×10^{-1}	-
WRTau_WR2600_N1100	0.58×10^{-1}	-
WRTau_WR2600_N1200	0.55×10^{-1}	-
WRTau_WR2600_N1300	0.50×10^{-1}	-
WRTau_WR2600_N1400	0.47×10^{-1}	-
WRTau_WR2600_N1500	0.42×10^{-1}	-
WRTau_WR2600_N1600	0.38×10^{-1}	-
WRTau_WR2600_N1700	0.33×10^{-1}	-
WRTau_WR2600_N1800	0.28×10^{-1}	-
WRTau_WR2600_N1900	0.24×10^{-1}	-
WRTau_WR2600_N2000	0.19×10^{-1}	-
WRTau_WR2600_N200	0.82×10^{-1}	-
WRTau_WR2600_N2100	0.14×10^{-1}	-
WRTau_WR2600_N2200	0.98×10^{-2}	-
WRTau_WR2600_N2300	0.61×10^{-2}	-
WRTau_WR2600_N2400	0.31×10^{-2}	-
WRTau_WR2600_N2500	0.11×10^{-2}	-
WRTau_WR2600_N300	0.79×10^{-1}	-
WRTau_WR2600_N400	0.78×10^{-1}	-
WRTau_WR2600_N500	0.75×10^{-1}	-
WRTau_WR2600_N600	0.73×10^{-1}	-
WRTau_WR2600_N700	0.70×10^{-1}	-
WRTau_WR2600_N800	0.68×10^{-1}	-
WRTau_WR2600_N900	0.65×10^{-1}	-
WRTau_WR2800_N1000	0.40×10^{-1}	-
WRTau_WR2800_N100	0.53×10^{-1}	-
WRTau_WR2800_N1100	0.38×10^{-1}	-
WRTau_WR2800_N1200	0.36×10^{-1}	-
WRTau_WR2800_N1300	0.34×10^{-1}	-
WRTau_WR2800_N1400	0.31×10^{-1}	-
WRTau_WR2800_N1500	0.29×10^{-1}	-
WRTau_WR2800_N1600	0.27×10^{-1}	-
WRTau_WR2800_N1700	0.24×10^{-1}	-
WRTau_WR2800_N1800	0.21×10^{-1}	-
WRTau_WR2800_N1900	0.19×10^{-1}	-
WRTau_WR2800_N2000	0.16×10^{-1}	-
WRTau_WR2800_N200	0.52×10^{-1}	-

WRTau_WR2800_N2100	0.13×10^{-1}	-
WRTau_WR2800_N2200	0.10×10^{-1}	-
WRTau_WR2800_N2300	0.77×10^{-2}	-
WRTau_WR2800_N2400	0.53×10^{-2}	-
WRTau_WR2800_N2500	0.33×10^{-2}	-
WRTau_WR2800_N2600	0.17×10^{-2}	-
WRTau_WR2800_N2700	0.62×10^{-3}	-
WRTau_WR2800_N300	0.50×10^{-1}	-
WRTau_WR2800_N400	0.49×10^{-1}	-
WRTau_WR2800_N500	0.47×10^{-1}	-
WRTau_WR2800_N600	0.46×10^{-1}	-
WRTau_WR2800_N700	0.45×10^{-1}	-
WRTau_WR2800_N800	0.43×10^{-1}	-
WRTau_WR2800_N900	0.41×10^{-1}	-
WRTau_WR3000_N1000	0.26×10^{-1}	-
WRTau_WR3000_N100	0.34×10^{-1}	-
WRTau_WR3000_N1100	0.25×10^{-1}	-
WRTau_WR3000_N1200	0.23×10^{-1}	-
WRTau_WR3000_N1300	0.22×10^{-1}	-
WRTau_WR3000_N1400	0.21×10^{-1}	-
WRTau_WR3000_N1500	0.20×10^{-1}	-
WRTau_WR3000_N1600	0.18×10^{-1}	-
WRTau_WR3000_N1700	0.17×10^{-1}	-
WRTau_WR3000_N1800	0.15×10^{-1}	-
WRTau_WR3000_N1900	0.14×10^{-1}	-
WRTau_WR3000_N2000	0.12×10^{-1}	-
WRTau_WR3000_N200	0.33×10^{-1}	-
WRTau_WR3000_N2100	0.11×10^{-1}	-
WRTau_WR3000_N2200	0.90×10^{-2}	-
WRTau_WR3000_N2300	0.74×10^{-2}	-
WRTau_WR3000_N2400	0.58×10^{-2}	-
WRTau_WR3000_N2500	0.43×10^{-2}	-
WRTau_WR3000_N2600	0.30×10^{-2}	-
WRTau_WR3000_N2700	0.18×10^{-2}	-
WRTau_WR3000_N2800	0.94×10^{-3}	-
WRTau_WR3000_N2900	0.35×10^{-3}	-
WRTau_WR3000_N300	0.32×10^{-1}	-
WRTau_WR3000_N400	0.32×10^{-1}	-
WRTau_WR3000_N500	0.31×10^{-1}	-
WRTau_WR3000_N600	0.30×10^{-1}	-
WRTau_WR3000_N700	0.29×10^{-1}	-
WRTau_WR3000_N800	0.28×10^{-1}	-
WRTau_WR3000_N900	0.27×10^{-1}	-
WRTau_WR3200_N1000	0.17×10^{-1}	-
WRTau_WR3200_N100	0.23×10^{-1}	-
WRTau_WR3200_N1100	0.16×10^{-1}	-
WRTau_WR3200_N1200	0.16×10^{-1}	-
WRTau_WR3200_N1300	0.15×10^{-1}	-
WRTau_WR3200_N1400	0.14×10^{-1}	-

WRTau_WR3200_N1500	0.13×10^{-1}	-
WRTau_WR3200_N1600	0.13×10^{-1}	-
WRTau_WR3200_N1700	0.12×10^{-1}	-
WRTau_WR3200_N1800	0.11×10^{-1}	-
WRTau_WR3200_N1900	0.99×10^{-2}	-
WRTau_WR3200_N2000	0.90×10^{-2}	-
WRTau_WR3200_N200	0.22×10^{-1}	-
WRTau_WR3200_N2100	0.80×10^{-2}	-
WRTau_WR3200_N2200	0.70×10^{-2}	-
WRTau_WR3200_N2300	0.61×10^{-2}	-
WRTau_WR3200_N2400	0.51×10^{-2}	-
WRTau_WR3200_N2500	0.42×10^{-2}	-
WRTau_WR3200_N2600	0.33×10^{-2}	-
WRTau_WR3200_N2700	0.24×10^{-2}	-
WRTau_WR3200_N2800	0.17×10^{-2}	-
WRTau_WR3200_N2900	0.10×10^{-2}	-
WRTau_WR3200_N3000	0.53×10^{-3}	-
WRTau_WR3200_N300	0.21×10^{-1}	-
WRTau_WR3200_N3100	0.20×10^{-3}	-
WRTau_WR3200_N400	0.21×10^{-1}	-
WRTau_WR3200_N500	0.20×10^{-1}	-
WRTau_WR3200_N600	0.19×10^{-1}	-
WRTau_WR3200_N700	0.19×10^{-1}	-
WRTau_WR3200_N800	0.18×10^{-1}	-
WRTau_WR3200_N900	0.17×10^{-1}	-
WRTau_WR3400_N1000	0.11×10^{-1}	-
WRTau_WR3400_N100	0.15×10^{-1}	-
WRTau_WR3400_N1100	0.11×10^{-1}	-
WRTau_WR3400_N1200	0.10×10^{-1}	-
WRTau_WR3400_N1300	0.99×10^{-2}	-
WRTau_WR3400_N1400	0.94×10^{-2}	-
WRTau_WR3400_N1500	0.89×10^{-2}	-
WRTau_WR3400_N1600	0.85×10^{-2}	-
WRTau_WR3400_N1700	0.80×10^{-2}	-
WRTau_WR3400_N1800	0.75×10^{-2}	-
WRTau_WR3400_N1900	0.70×10^{-2}	-
WRTau_WR3400_N2000	0.64×10^{-2}	-
WRTau_WR3400_N200	0.15×10^{-1}	-
WRTau_WR3400_N2100	0.58×10^{-2}	-
WRTau_WR3400_N2200	0.53×10^{-2}	-
WRTau_WR3400_N2300	0.47×10^{-2}	-
WRTau_WR3400_N2400	0.42×10^{-2}	-
WRTau_WR3400_N2500	0.36×10^{-2}	-
WRTau_WR3400_N2600	0.30×10^{-2}	-
WRTau_WR3400_N2700	0.24×10^{-2}	-
WRTau_WR3400_N2800	0.19×10^{-2}	-
WRTau_WR3400_N2900	0.14×10^{-2}	-
WRTau_WR3400_N3000	0.96×10^{-3}	-
WRTau_WR3400_N300	0.14×10^{-1}	-

WRTau_WR3400_N3100	0.59×10^{-3}	-
WRTau_WR3400_N3200	0.30×10^{-3}	-
WRTau_WR3400_N3300	0.12×10^{-3}	-
WRTau_WR3400_N400	0.14×10^{-1}	-
WRTau_WR3400_N500	0.13×10^{-1}	-
WRTau_WR3400_N600	0.13×10^{-1}	-
WRTau_WR3400_N700	0.12×10^{-1}	-
WRTau_WR3400_N800	0.12×10^{-1}	-
WRTau_WR3400_N900	0.11×10^{-1}	-
WRTau_WR3600_N1000	0.75×10^{-2}	-
WRTau_WR3600_N100	0.10×10^{-1}	-
WRTau_WR3600_N1100	0.71×10^{-2}	-
WRTau_WR3600_N1200	0.69×10^{-2}	-
WRTau_WR3600_N1300	0.67×10^{-2}	-
WRTau_WR3600_N1400	0.64×10^{-2}	-
WRTau_WR3600_N1500	0.61×10^{-2}	-
WRTau_WR3600_N1600	0.58×10^{-2}	-
WRTau_WR3600_N1700	0.55×10^{-2}	-
WRTau_WR3600_N1800	0.52×10^{-2}	-
WRTau_WR3600_N1900	0.49×10^{-2}	-
WRTau_WR3600_N2000	0.46×10^{-2}	-
WRTau_WR3600_N200	1.00×10^{-2}	-
WRTau_WR3600_N2100	0.42×10^{-2}	-
WRTau_WR3600_N2200	0.39×10^{-2}	-
WRTau_WR3600_N2300	0.35×10^{-2}	-
WRTau_WR3600_N2400	0.32×10^{-2}	-
WRTau_WR3600_N2500	0.28×10^{-2}	-
WRTau_WR3600_N2600	0.25×10^{-2}	-
WRTau_WR3600_N2700	0.21×10^{-2}	-
WRTau_WR3600_N2800	0.18×10^{-2}	-
WRTau_WR3600_N2900	0.14×10^{-2}	-
WRTau_WR3600_N3000	0.11×10^{-2}	-
WRTau_WR3600_N300	0.95×10^{-2}	-
WRTau_WR3600_N3100	0.82×10^{-3}	-
WRTau_WR3600_N3200	0.56×10^{-3}	-
WRTau_WR3600_N3300	0.34×10^{-3}	-
WRTau_WR3600_N3400	0.18×10^{-3}	-
WRTau_WR3600_N3500	0.72×10^{-4}	-
WRTau_WR3600_N400	0.91×10^{-2}	-
WRTau_WR3600_N500	0.89×10^{-2}	-
WRTau_WR3600_N600	0.85×10^{-2}	-
WRTau_WR3600_N700	0.82×10^{-2}	-
WRTau_WR3600_N800	0.80×10^{-2}	-
WRTau_WR3600_N900	0.77×10^{-2}	-
WRTau_WR3800_N1000	0.50×10^{-2}	-
WRTau_WR3800_N100	0.73×10^{-2}	-
WRTau_WR3800_N1100	0.48×10^{-2}	-
WRTau_WR3800_N1200	0.47×10^{-2}	-
WRTau_WR3800_N1300	0.46×10^{-2}	-

WRTau_WR3800_N1400	0.43×10^{-2}	-
WRTau_WR3800_N1500	0.42×10^{-2}	-
WRTau_WR3800_N1600	0.40×10^{-2}	-
WRTau_WR3800_N1700	0.38×10^{-2}	-
WRTau_WR3800_N1800	0.36×10^{-2}	-
WRTau_WR3800_N1900	0.34×10^{-2}	-
WRTau_WR3800_N2000	0.32×10^{-2}	-
WRTau_WR3800_N200	0.68×10^{-2}	-
WRTau_WR3800_N2100	0.30×10^{-2}	-
WRTau_WR3800_N2200	0.28×10^{-2}	-
WRTau_WR3800_N2300	0.26×10^{-2}	-
WRTau_WR3800_N2400	0.24×10^{-2}	-
WRTau_WR3800_N2500	0.22×10^{-2}	-
WRTau_WR3800_N2600	0.19×10^{-2}	-
WRTau_WR3800_N2700	0.17×10^{-2}	-
WRTau_WR3800_N2800	0.15×10^{-2}	-
WRTau_WR3800_N2900	0.13×10^{-2}	-
WRTau_WR3800_N3000	0.11×10^{-2}	-
WRTau_WR3800_N300	0.65×10^{-2}	-
WRTau_WR3800_N3100	0.86×10^{-3}	-
WRTau_WR3800_N3200	0.67×10^{-3}	-
WRTau_WR3800_N3300	0.49×10^{-3}	-
WRTau_WR3800_N3400	0.33×10^{-3}	-
WRTau_WR3800_N3500	0.21×10^{-3}	-
WRTau_WR3800_N3600	0.11×10^{-3}	-
WRTau_WR3800_N3700	0.44×10^{-4}	-
WRTau_WR3800_N400	0.62×10^{-2}	-
WRTau_WR3800_N500	0.60×10^{-2}	-
WRTau_WR3800_N600	0.58×10^{-2}	-
WRTau_WR3800_N700	0.56×10^{-2}	-
WRTau_WR3800_N800	0.54×10^{-2}	-
WRTau_WR3800_N900	0.52×10^{-2}	-
WRTau_WR4000_N1000	0.35×10^{-2}	-
WRTau_WR4000_N100	0.51×10^{-2}	-
WRTau_WR4000_N1100	0.33×10^{-2}	-
WRTau_WR4000_N1200	0.32×10^{-2}	-
WRTau_WR4000_N1300	0.31×10^{-2}	-
WRTau_WR4000_N1400	0.30×10^{-2}	-
WRTau_WR4000_N1500	0.29×10^{-2}	-
WRTau_WR4000_N1600	0.28×10^{-2}	-
WRTau_WR4000_N1700	0.26×10^{-2}	-
WRTau_WR4000_N1800	0.25×10^{-2}	-
WRTau_WR4000_N1900	0.24×10^{-2}	-
WRTau_WR4000_N2000	0.23×10^{-2}	-
WRTau_WR4000_N200	0.48×10^{-2}	-
WRTau_WR4000_N2100	0.22×10^{-2}	-
WRTau_WR4000_N2200	0.20×10^{-2}	-
WRTau_WR4000_N2300	0.19×10^{-2}	-
WRTau_WR4000_N2400	0.18×10^{-2}	-

WRTau_WR4000_N2500	0.16×10^{-2}	-
WRTau_WR4000_N2600	0.15×10^{-2}	-
WRTau_WR4000_N2700	0.13×10^{-2}	-
WRTau_WR4000_N2800	0.12×10^{-2}	-
WRTau_WR4000_N2900	0.11×10^{-2}	-
WRTau_WR4000_N3000	0.92×10^{-3}	-
WRTau_WR4000_N300	0.46×10^{-2}	-
WRTau_WR4000_N3100	0.79×10^{-3}	-
WRTau_WR4000_N3200	0.65×10^{-3}	-
WRTau_WR4000_N3300	0.52×10^{-3}	-
WRTau_WR4000_N3400	0.41×10^{-3}	-
WRTau_WR4000_N3500	0.30×10^{-3}	-
WRTau_WR4000_N3600	0.20×10^{-3}	-
WRTau_WR4000_N3700	0.13×10^{-3}	-
WRTau_WR4000_N3800	0.66×10^{-4}	-
WRTau_WR4000_N3900	0.28×10^{-4}	-
WRTau_WR4000_N400	0.44×10^{-2}	-
WRTau_WR4000_N500	0.42×10^{-2}	-
WRTau_WR4000_N600	0.40×10^{-2}	-
WRTau_WR4000_N700	0.39×10^{-2}	-
WRTau_WR4000_N800	0.37×10^{-2}	-
WRTau_WR4000_N900	0.36×10^{-2}	-
WRTau_WR4200_N1000	0.24×10^{-2}	-
WRTau_WR4200_N100	0.37×10^{-2}	-
WRTau_WR4200_N1100	0.23×10^{-2}	-
WRTau_WR4200_N1200	0.23×10^{-2}	-
WRTau_WR4200_N1300	0.22×10^{-2}	-
WRTau_WR4200_N1400	0.21×10^{-2}	-
WRTau_WR4200_N1500	0.20×10^{-2}	-
WRTau_WR4200_N1600	0.19×10^{-2}	-
WRTau_WR4200_N1700	0.19×10^{-2}	-
WRTau_WR4200_N1800	0.18×10^{-2}	-
WRTau_WR4200_N1900	0.17×10^{-2}	-
WRTau_WR4200_N2000	0.16×10^{-2}	-
WRTau_WR4200_N200	0.35×10^{-2}	-
WRTau_WR4200_N2100	0.15×10^{-2}	-
WRTau_WR4200_N2200	0.15×10^{-2}	-
WRTau_WR4200_N2300	0.14×10^{-2}	-
WRTau_WR4200_N2400	0.13×10^{-2}	-
WRTau_WR4200_N2500	0.12×10^{-2}	-
WRTau_WR4200_N2600	0.11×10^{-2}	-
WRTau_WR4200_N2700	0.10×10^{-2}	-
WRTau_WR4200_N2800	0.94×10^{-3}	-
WRTau_WR4200_N2900	0.85×10^{-3}	-
WRTau_WR4200_N3000	0.76×10^{-3}	-
WRTau_WR4200_N300	0.33×10^{-2}	-
WRTau_WR4200_N3100	0.67×10^{-3}	-
WRTau_WR4200_N3200	0.58×10^{-3}	-
WRTau_WR4200_N3300	0.49×10^{-3}	-

WRTau_WR4200_N3400	0.41×10^{-3}	-
WRTau_WR4200_N3500	0.32×10^{-3}	-
WRTau_WR4200_N3600	0.25×10^{-3}	-
WRTau_WR4200_N3700	0.18×10^{-3}	-
WRTau_WR4200_N3800	0.13×10^{-3}	-
WRTau_WR4200_N3900	0.78×10^{-4}	-
WRTau_WR4200_N4000	0.42×10^{-4}	-
WRTau_WR4200_N400	0.31×10^{-2}	-
WRTau_WR4200_N4100	0.18×10^{-4}	-
WRTau_WR4200_N500	0.30×10^{-2}	-
WRTau_WR4200_N600	0.28×10^{-2}	-
WRTau_WR4200_N700	0.27×10^{-2}	-
WRTau_WR4200_N800	0.26×10^{-2}	-
WRTau_WR4200_N900	0.25×10^{-2}	-
WRTau_WR4400_N1000	0.17×10^{-2}	-
WRTau_WR4400_N100	0.28×10^{-2}	-
WRTau_WR4400_N1100	0.17×10^{-2}	-
WRTau_WR4400_N1200	0.16×10^{-2}	-
WRTau_WR4400_N1300	0.15×10^{-2}	-
WRTau_WR4400_N1400	0.15×10^{-2}	-
WRTau_WR4400_N1500	0.14×10^{-2}	-
WRTau_WR4400_N1600	0.14×10^{-2}	-
WRTau_WR4400_N1700	0.13×10^{-2}	-
WRTau_WR4400_N1800	0.13×10^{-2}	-
WRTau_WR4400_N1900	0.12×10^{-2}	-
WRTau_WR4400_N2000	0.12×10^{-2}	-
WRTau_WR4400_N200	0.26×10^{-2}	-
WRTau_WR4400_N2100	0.11×10^{-2}	-
WRTau_WR4400_N2200	0.11×10^{-2}	-
WRTau_WR4400_N2300	0.10×10^{-2}	-
WRTau_WR4400_N2400	0.96×10^{-3}	-
WRTau_WR4400_N2500	0.90×10^{-3}	-
WRTau_WR4400_N2600	0.85×10^{-3}	-
WRTau_WR4400_N2700	0.78×10^{-3}	-
WRTau_WR4400_N2800	0.72×10^{-3}	-
WRTau_WR4400_N2900	0.66×10^{-3}	-
WRTau_WR4400_N3000	0.60×10^{-3}	-
WRTau_WR4400_N300	0.24×10^{-2}	-
WRTau_WR4400_N3100	0.55×10^{-3}	-
WRTau_WR4400_N3200	0.49×10^{-3}	-
WRTau_WR4400_N3300	0.43×10^{-3}	-
WRTau_WR4400_N3400	0.37×10^{-3}	-
WRTau_WR4400_N3500	0.31×10^{-3}	-
WRTau_WR4400_N3600	0.26×10^{-3}	-
WRTau_WR4400_N3700	0.21×10^{-3}	-
WRTau_WR4400_N3800	0.16×10^{-3}	-
WRTau_WR4400_N3900	0.12×10^{-3}	-
WRTau_WR4400_N4000	0.80×10^{-4}	-
WRTau_WR4400_N400	0.23×10^{-2}	-

WRTau_WR4400_N4100	0.50×10^{-4}	-
WRTau_WR4400_N4200	0.27×10^{-4}	-
WRTau_WR4400_N4300	0.12×10^{-4}	-
WRTau_WR4400_N500	0.21×10^{-2}	-
WRTau_WR4400_N600	0.20×10^{-2}	-
WRTau_WR4400_N700	0.19×10^{-2}	-
WRTau_WR4400_N800	0.19×10^{-2}	-
WRTau_WR4400_N900	0.18×10^{-2}	-
WRTau_WR4600_N1000	0.13×10^{-2}	-
WRTau_WR4600_N100	0.21×10^{-2}	-
WRTau_WR4600_N1100	0.12×10^{-2}	-
WRTau_WR4600_N1200	0.12×10^{-2}	-
WRTau_WR4600_N1300	0.11×10^{-2}	-
WRTau_WR4600_N1400	0.11×10^{-2}	-
WRTau_WR4600_N1500	0.10×10^{-2}	-
WRTau_WR4600_N1600	0.10×10^{-2}	-
WRTau_WR4600_N1700	0.97×10^{-3}	-
WRTau_WR4600_N1800	0.93×10^{-3}	-
WRTau_WR4600_N1900	0.89×10^{-3}	-
WRTau_WR4600_N2000	0.86×10^{-3}	-
WRTau_WR4600_N200	0.19×10^{-2}	-
WRTau_WR4600_N2100	0.82×10^{-3}	-
WRTau_WR4600_N2200	0.79×10^{-3}	-
WRTau_WR4600_N2300	0.75×10^{-3}	-
WRTau_WR4600_N2400	0.71×10^{-3}	-
WRTau_WR4600_N2500	0.68×10^{-3}	-
WRTau_WR4600_N2600	0.64×10^{-3}	-
WRTau_WR4600_N2700	0.60×10^{-3}	-
WRTau_WR4600_N2800	0.56×10^{-3}	-
WRTau_WR4600_N2900	0.52×10^{-3}	-
WRTau_WR4600_N3000	0.48×10^{-3}	-
WRTau_WR4600_N300	0.18×10^{-2}	-
WRTau_WR4600_N3100	0.44×10^{-3}	-
WRTau_WR4600_N3200	0.40×10^{-3}	-
WRTau_WR4600_N3300	0.36×10^{-3}	-
WRTau_WR4600_N3400	0.32×10^{-3}	-
WRTau_WR4600_N3500	0.28×10^{-3}	-
WRTau_WR4600_N3600	0.24×10^{-3}	-
WRTau_WR4600_N3700	0.20×10^{-3}	-
WRTau_WR4600_N3800	0.17×10^{-3}	-
WRTau_WR4600_N3900	0.13×10^{-3}	-
WRTau_WR4600_N4000	0.10×10^{-3}	-
WRTau_WR4600_N400	0.17×10^{-2}	-
WRTau_WR4600_N4100	0.76×10^{-4}	-
WRTau_WR4600_N4200	0.52×10^{-4}	-
WRTau_WR4600_N4300	0.33×10^{-4}	-
WRTau_WR4600_N4400	0.18×10^{-4}	-
WRTau_WR4600_N4500	0.79×10^{-5}	-
WRTau_WR4600_N500	0.16×10^{-2}	-

WRTau_WR4600_N600	0.15×10^{-2}	-
WRTau_WR4600_N700	0.14×10^{-2}	-
WRTau_WR4600_N800	0.14×10^{-2}	-
WRTau_WR4600_N900	0.13×10^{-2}	-
WRTau_WR4800_N1000	0.93×10^{-3}	-
WRTau_WR4800_N100	0.16×10^{-2}	-
WRTau_WR4800_N1100	0.88×10^{-3}	-
WRTau_WR4800_N1200	0.85×10^{-3}	-
WRTau_WR4800_N1300	0.82×10^{-3}	-
WRTau_WR4800_N1400	0.79×10^{-3}	-
WRTau_WR4800_N1500	0.76×10^{-3}	-
WRTau_WR4800_N1600	0.74×10^{-3}	-
WRTau_WR4800_N1700	0.71×10^{-3}	-
WRTau_WR4800_N1800	0.69×10^{-3}	-
WRTau_WR4800_N1900	0.66×10^{-3}	-
WRTau_WR4800_N2000	0.64×10^{-3}	-
WRTau_WR4800_N200	0.15×10^{-2}	-
WRTau_WR4800_N2100	0.61×10^{-3}	-
WRTau_WR4800_N2200	0.58×10^{-3}	-
WRTau_WR4800_N2300	0.56×10^{-3}	-
WRTau_WR4800_N2400	0.54×10^{-3}	-
WRTau_WR4800_N2500	0.51×10^{-3}	-
WRTau_WR4800_N2600	0.48×10^{-3}	-
WRTau_WR4800_N2700	0.46×10^{-3}	-
WRTau_WR4800_N2800	0.43×10^{-3}	-
WRTau_WR4800_N2900	0.40×10^{-3}	-
WRTau_WR4800_N3000	0.38×10^{-3}	-
WRTau_WR4800_N300	0.14×10^{-2}	-
WRTau_WR4800_N3100	0.35×10^{-3}	-
WRTau_WR4800_N3200	0.32×10^{-3}	-
WRTau_WR4800_N3300	0.30×10^{-3}	-
WRTau_WR4800_N3400	0.27×10^{-3}	-
WRTau_WR4800_N3500	0.24×10^{-3}	-
WRTau_WR4800_N3600	0.22×10^{-3}	-
WRTau_WR4800_N3700	0.19×10^{-3}	-
WRTau_WR4800_N3800	0.16×10^{-3}	-
WRTau_WR4800_N3900	0.14×10^{-3}	-
WRTau_WR4800_N4000	0.11×10^{-3}	-
WRTau_WR4800_N400	0.13×10^{-2}	-
WRTau_WR4800_N4100	0.91×10^{-4}	-
WRTau_WR4800_N4200	0.69×10^{-4}	-
WRTau_WR4800_N4300	0.51×10^{-4}	-
WRTau_WR4800_N4400	0.35×10^{-4}	-
WRTau_WR4800_N4500	0.22×10^{-4}	-
WRTau_WR4800_N4600	0.12×10^{-4}	-
WRTau_WR4800_N4700	0.55×10^{-5}	-
WRTau_WR4800_N500	0.12×10^{-2}	-
WRTau_WR4800_N600	0.11×10^{-2}	-
WRTau_WR4800_N700	0.11×10^{-2}	-

WRTau_WR4800_N800	0.10×10^{-2}	-
WRTau_WR4800_N900	0.97×10^{-3}	-
WRTau_WR5000_N1000	0.69×10^{-3}	-
WRTau_WR5000_N100	0.13×10^{-2}	-
WRTau_WR5000_N1100	0.67×10^{-3}	-
WRTau_WR5000_N1200	0.64×10^{-3}	-
WRTau_WR5000_N1300	0.61×10^{-3}	-
WRTau_WR5000_N1400	0.59×10^{-3}	-
WRTau_WR5000_N1500	0.57×10^{-3}	-
WRTau_WR5000_N1600	0.55×10^{-3}	-
WRTau_WR5000_N1700	0.54×10^{-3}	-
WRTau_WR5000_N1800	0.51×10^{-3}	-
WRTau_WR5000_N1900	0.50×10^{-3}	-
WRTau_WR5000_N2000	0.48×10^{-3}	-
WRTau_WR5000_N200	0.12×10^{-2}	-
WRTau_WR5000_N2100	0.46×10^{-3}	-
WRTau_WR5000_N2200	0.44×10^{-3}	-
WRTau_WR5000_N2300	0.42×10^{-3}	-
WRTau_WR5000_N2400	0.41×10^{-3}	-
WRTau_WR5000_N2500	0.39×10^{-3}	-
WRTau_WR5000_N2600	0.37×10^{-3}	-
WRTau_WR5000_N2700	0.35×10^{-3}	-
WRTau_WR5000_N2800	0.34×10^{-3}	-
WRTau_WR5000_N2900	0.32×10^{-3}	-
WRTau_WR5000_N3000	0.30×10^{-3}	-
WRTau_WR5000_N300	0.11×10^{-2}	-
WRTau_WR5000_N3100	0.28×10^{-3}	-
WRTau_WR5000_N3200	0.26×10^{-3}	-
WRTau_WR5000_N3300	0.24×10^{-3}	-
WRTau_WR5000_N3400	0.22×10^{-3}	-
WRTau_WR5000_N3500	0.20×10^{-3}	-
WRTau_WR5000_N3600	0.19×10^{-3}	-
WRTau_WR5000_N3700	0.17×10^{-3}	-
WRTau_WR5000_N3800	0.15×10^{-3}	-
WRTau_WR5000_N3900	0.13×10^{-3}	-
WRTau_WR5000_N4000	0.11×10^{-3}	-
WRTau_WR5000_N400	0.98×10^{-3}	-
WRTau_WR5000_N4100	0.93×10^{-4}	-
WRTau_WR5000_N4200	0.77×10^{-4}	-
WRTau_WR5000_N4300	0.61×10^{-4}	-
WRTau_WR5000_N4400	0.47×10^{-4}	-
WRTau_WR5000_N4500	0.35×10^{-4}	-
WRTau_WR5000_N4600	0.24×10^{-4}	-
WRTau_WR5000_N4700	0.15×10^{-4}	-
WRTau_WR5000_N4800	0.82×10^{-5}	-
WRTau_WR5000_N4900	0.38×10^{-5}	-
WRTau_WR5000_N500	0.91×10^{-3}	-
WRTau_WR5000_N600	0.86×10^{-3}	-
WRTau_WR5000_N700	0.80×10^{-3}	-

WRTau_WR5000_N800	0.77×10^{-3}	-
WRTau_WR5000_N900	0.72×10^{-3}	-

A.2 Generator Level Kinematic distributions

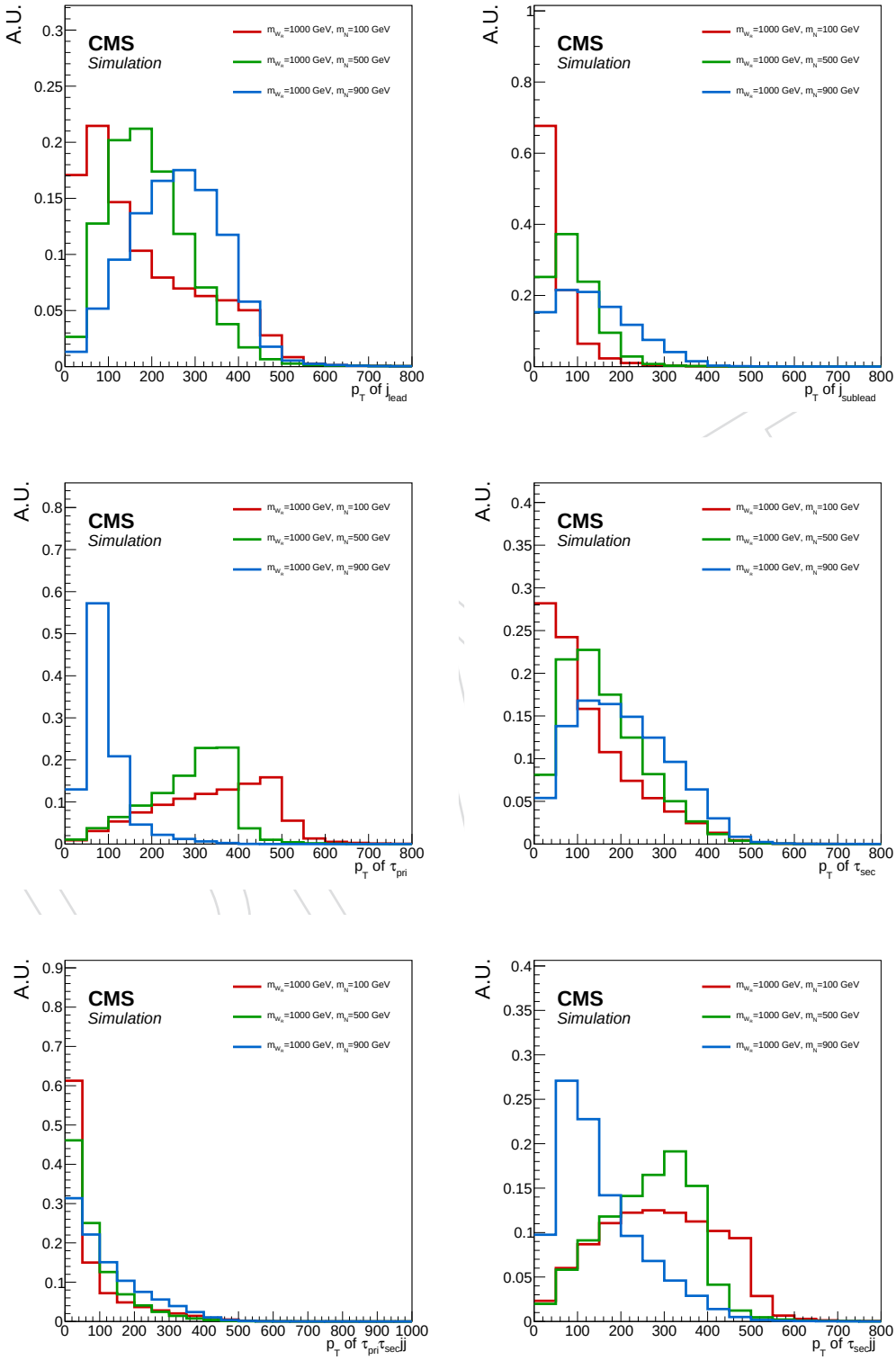

Figure 34: The p_T distributions of (sub)leading jet, primary and secondary τ, and N, W_R normalized by the number of events produced with different m_N and $m_{W_R} = 1$ TeV.

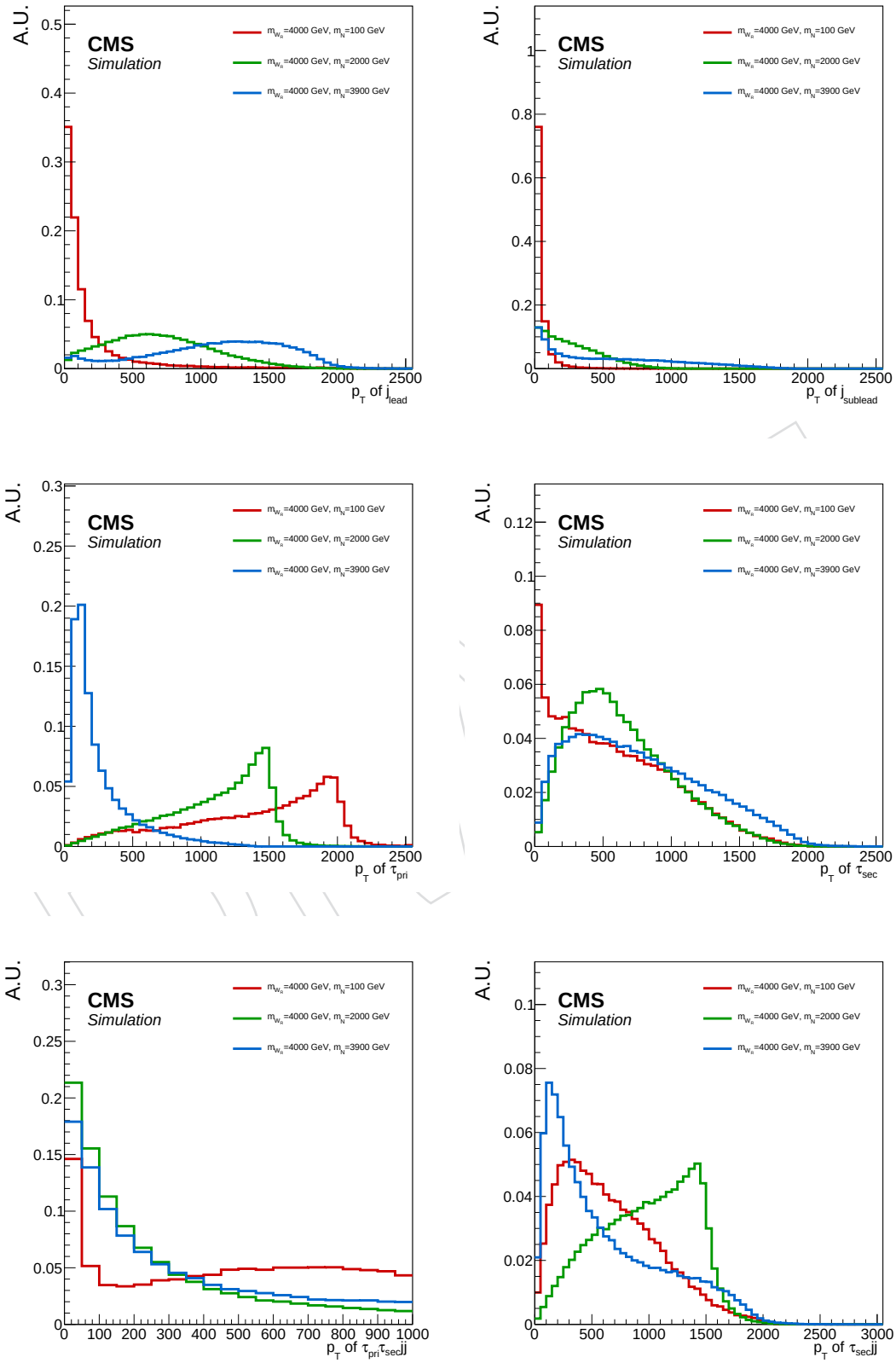

Figure 35: The p_T distributions of (sub)leading jet, primary and secondary τ, and N, W_R normalized by the number of events produced with different m_N and $m_{W_R} = 4$ TeV.

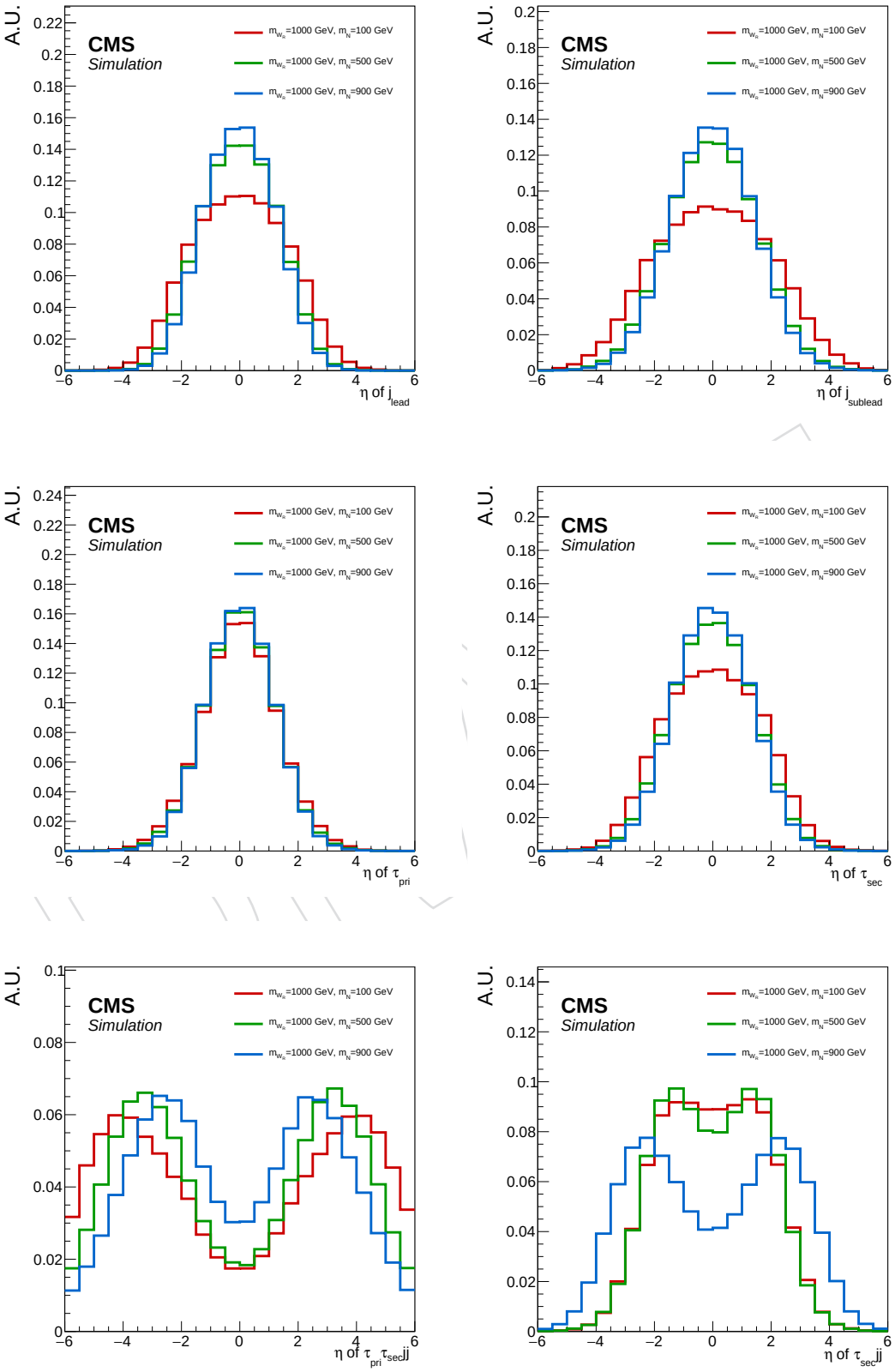

Figure 36: The η distributions of (sub)leading jet, primary and secondary τ, and N, W_R normalized by the number of events produced with different m_N and $m_{W_R} = 1$ TeV.

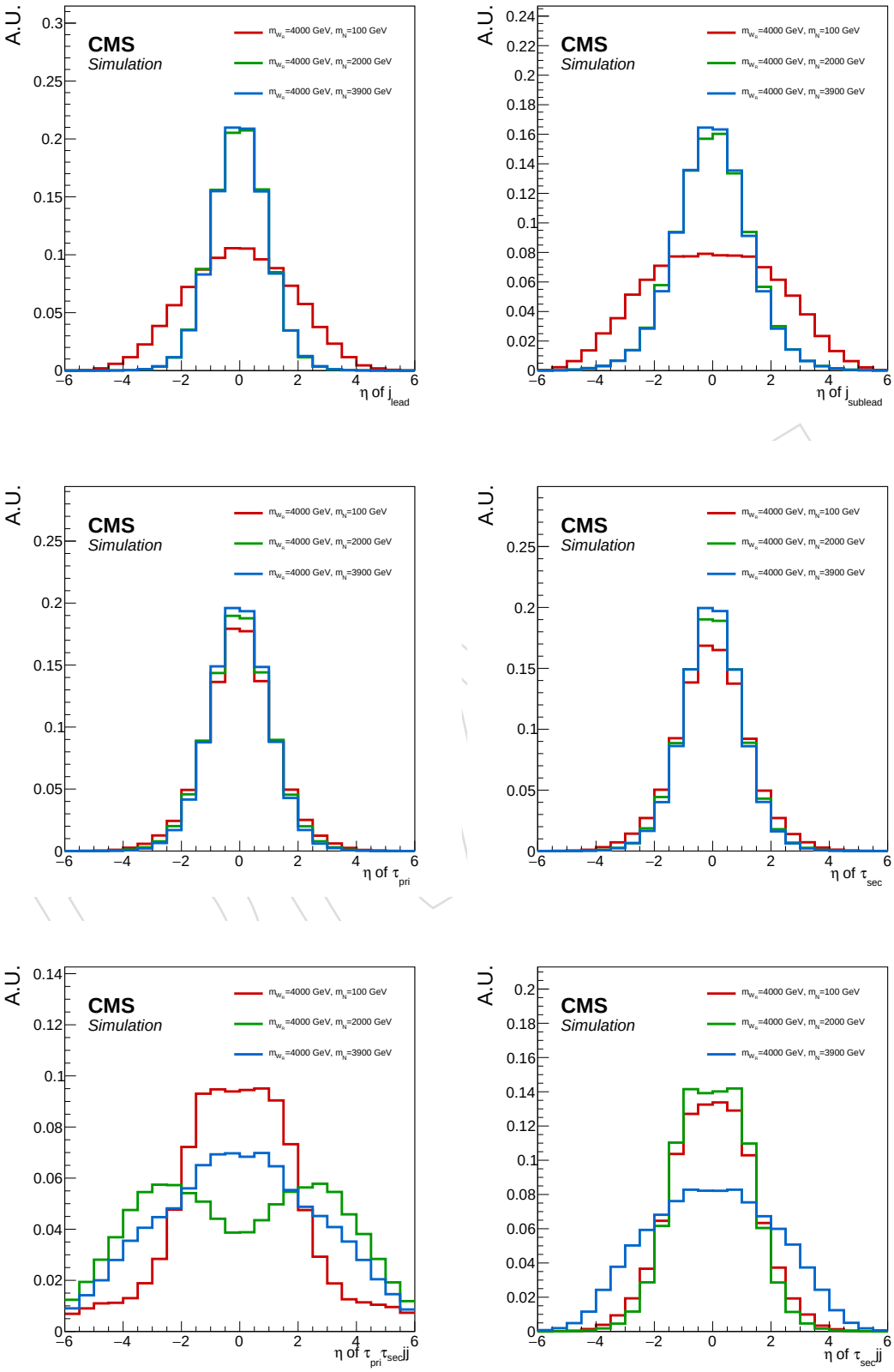

Figure 37: The η distributions of (sub)leading jet, primary and secondary τ, and N, W_R normalized by the number of events produced with different m_N and $m_{W_R} = 4$ TeV.

A.3 Signal Efficiencies

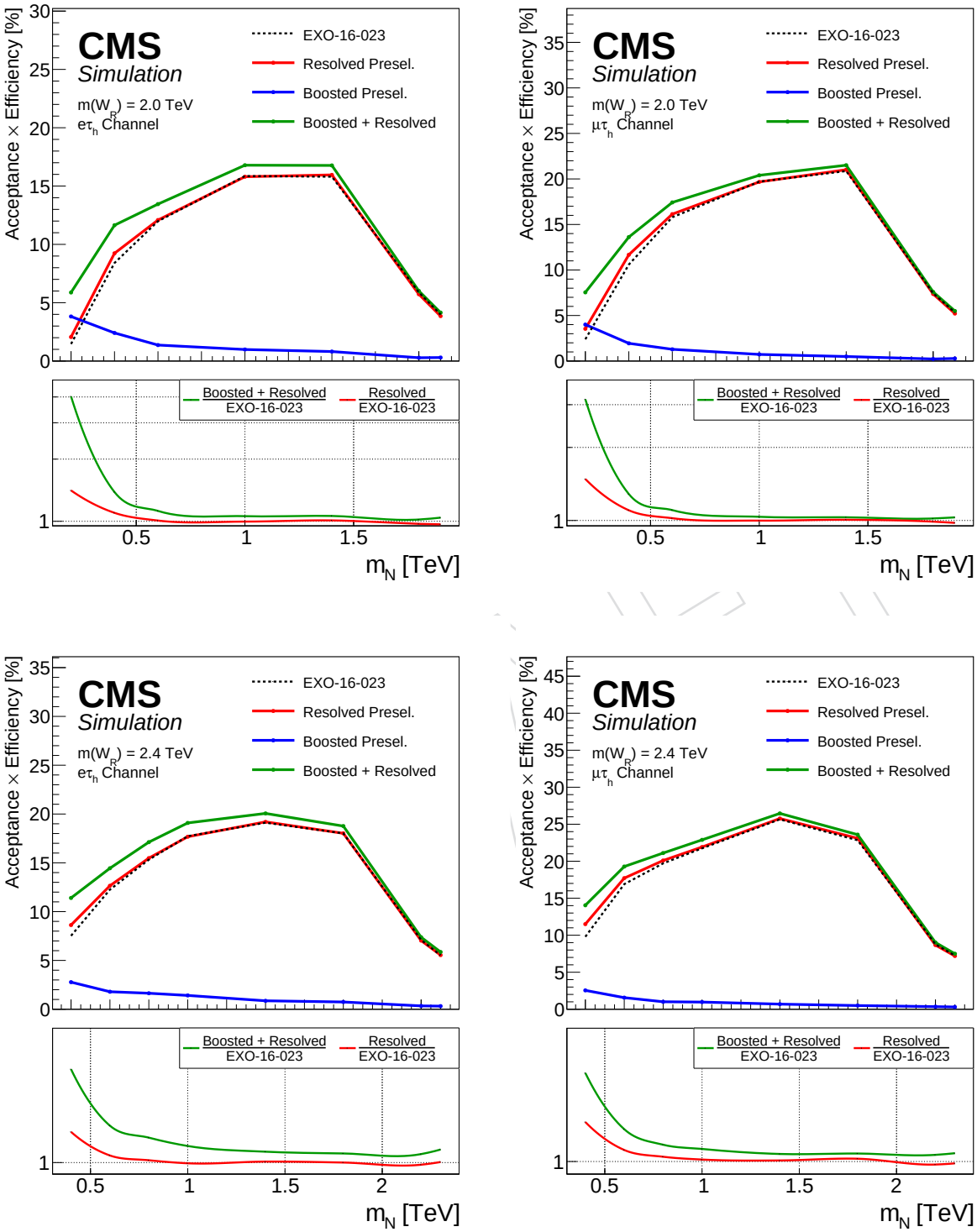

Figure 38: Signal preselection efficiency for $m(W_R)$=2.0 TeV (upper row) and $m(W_R)$=2.4 TeV (below row) with different m_N values for the electron (muon) channel in the left (right) column. The selections are before giving any missing transverse momentum or mass cuts.

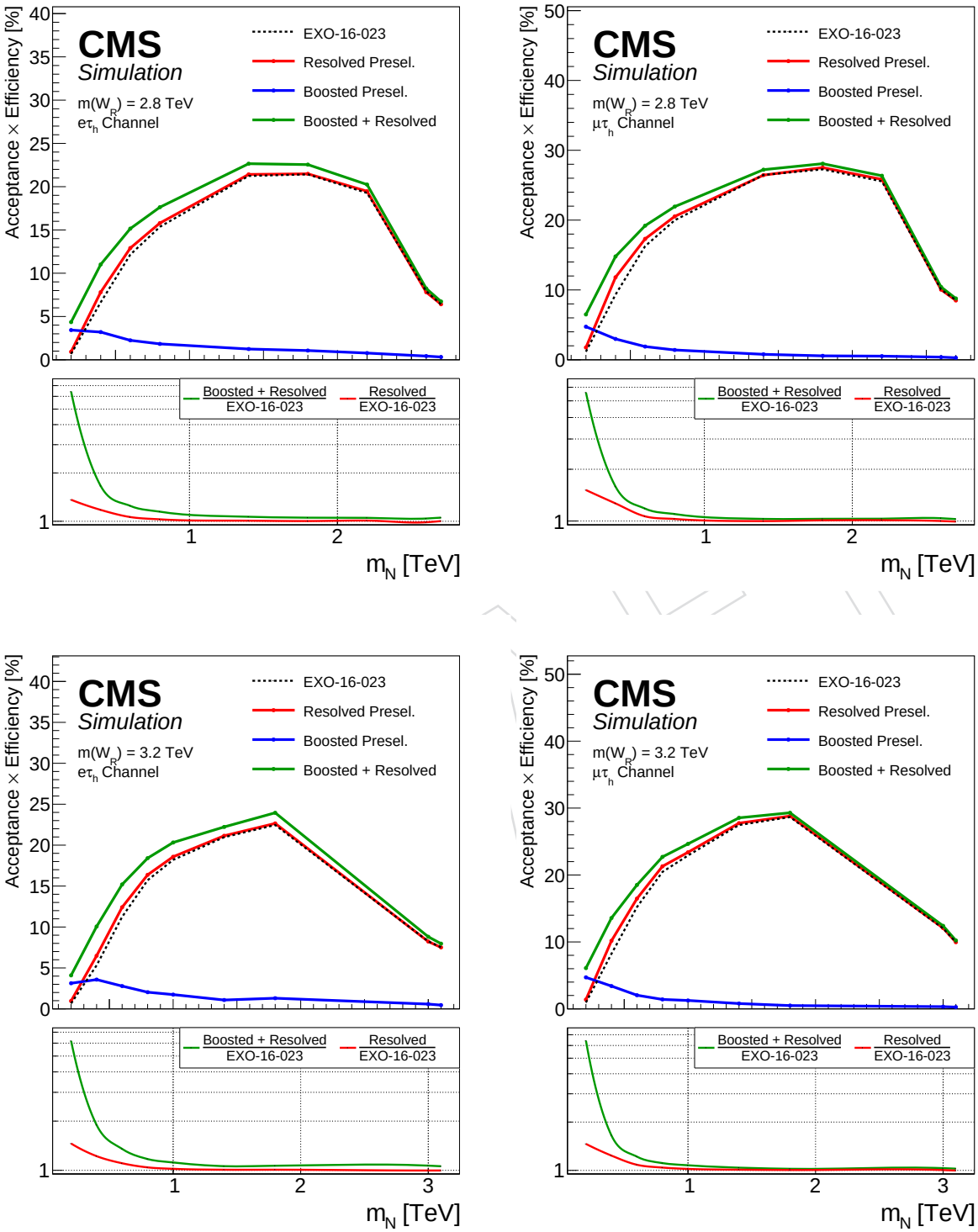

Figure 39: Signal preselection efficiency for $m(W_R)$=2.8 TeV (upper row) and $m(W_R)$=3.2 TeV (below row) with different m_N values for the electron (muon) channel in the left (right) column. The selections are before giving any missing transverse momentum or mass cuts.

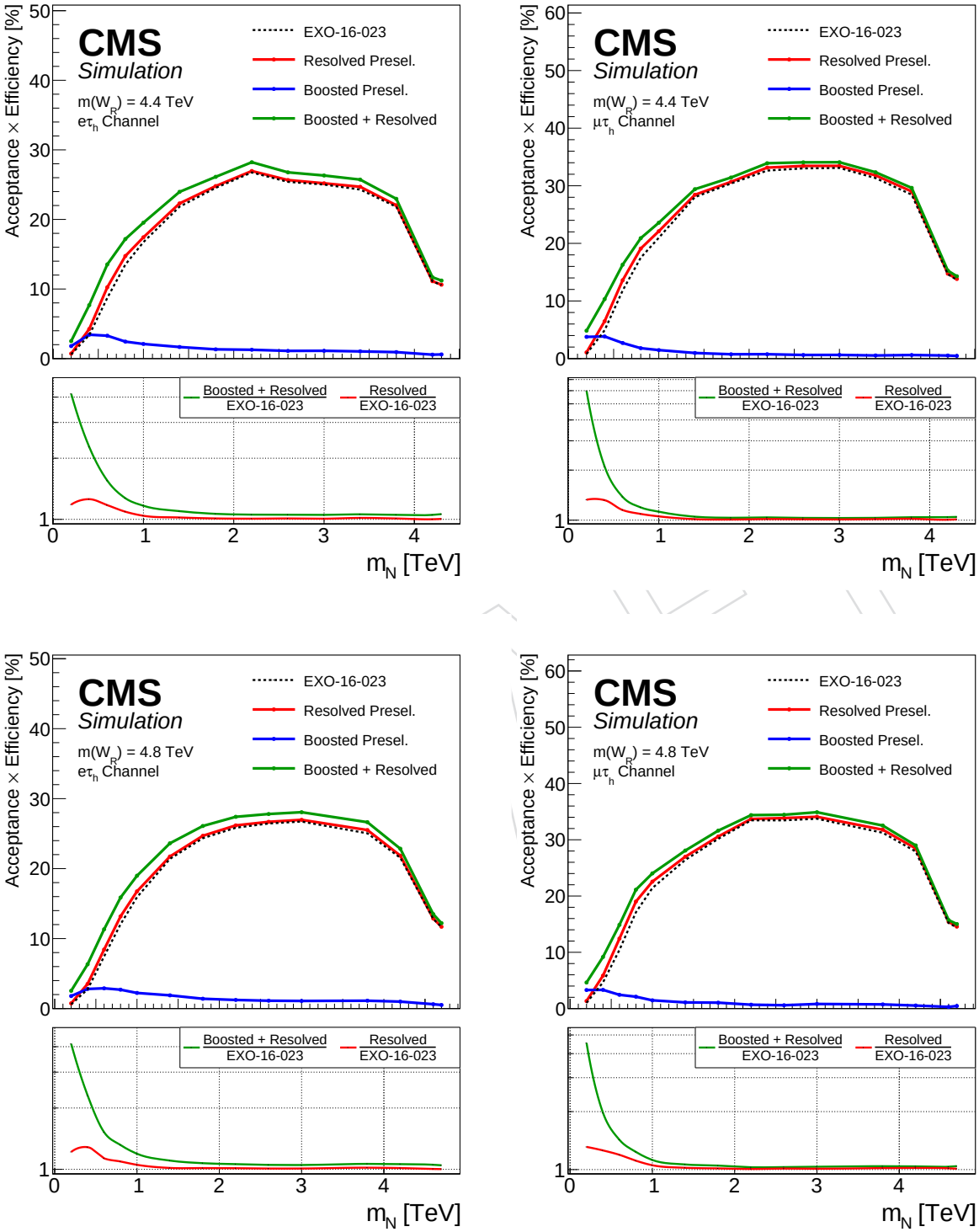

Figure 40: Signal preselection efficiency for $m(W_R)$=4.4 TeV (upper row) and $m(W_R)$=4.8 TeV (below row) with different m_N values for the electron (muon) channel in the left (right) column. The selections are before giving any missing transverse momentum or mass cuts.

B Optimization of Selections

B.1 Optimization of mass cut selection

Cut variables and values given after the preselection and the missing transverse momentum cut of 100 GeV is optimized by varying the cut and checking the significance of the signals in each region. Several variables are considered, such as the effective mass which is the mass of the 4-vector sum of all final state objects except the missing transverse momentum vector, $L_T + H_T$ which is the sum of all leptonic and hadronic momenta, S_T which is $L_T + H_T + E_T$.

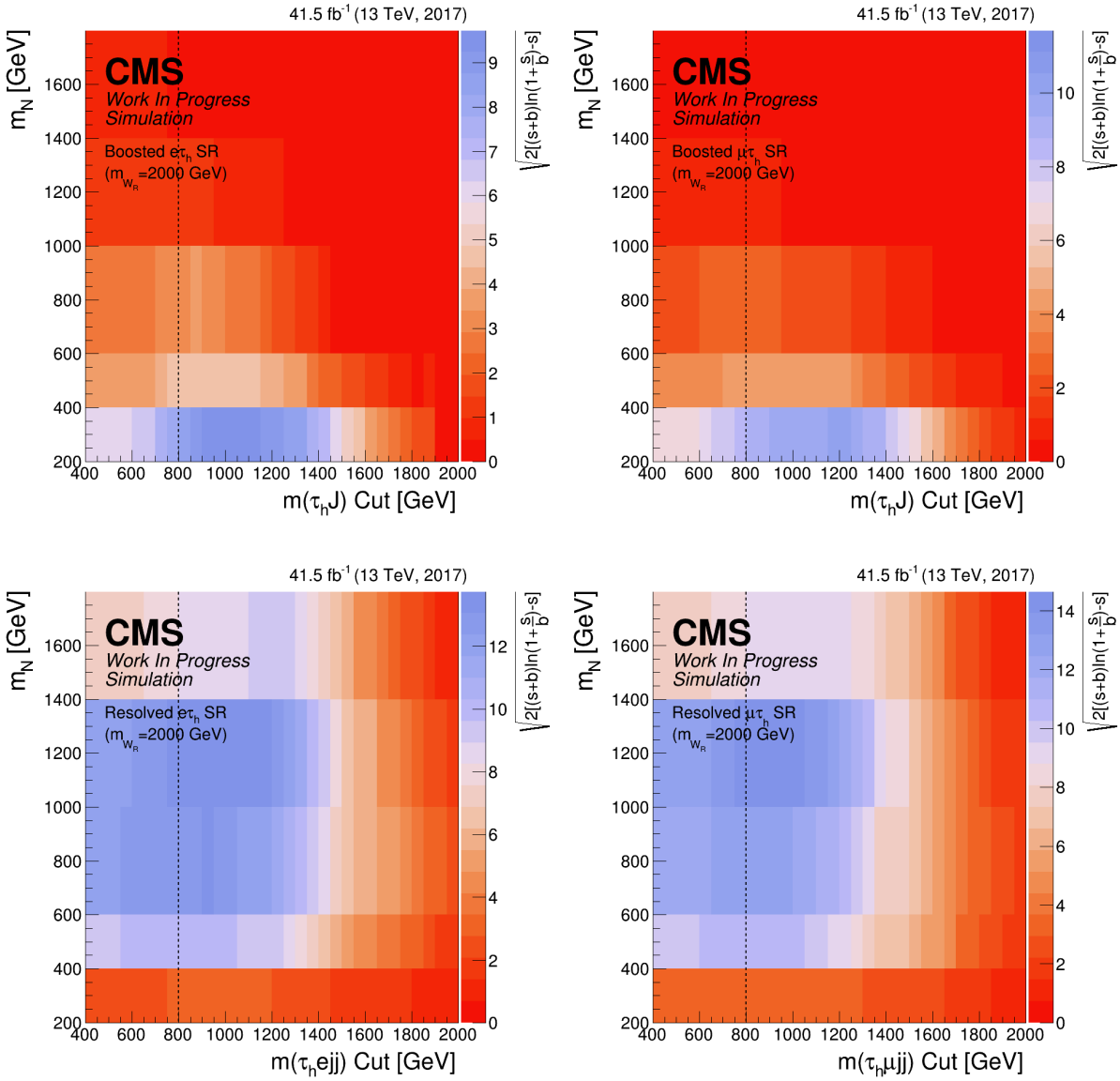

Figure 41: Significance of signals with the W_R mass fixed as 2 TeV with different N masses while differing the mass cut for each signal regions. Here the mass variable is defined as the mass value of the 4-vector sum of the final state objects.

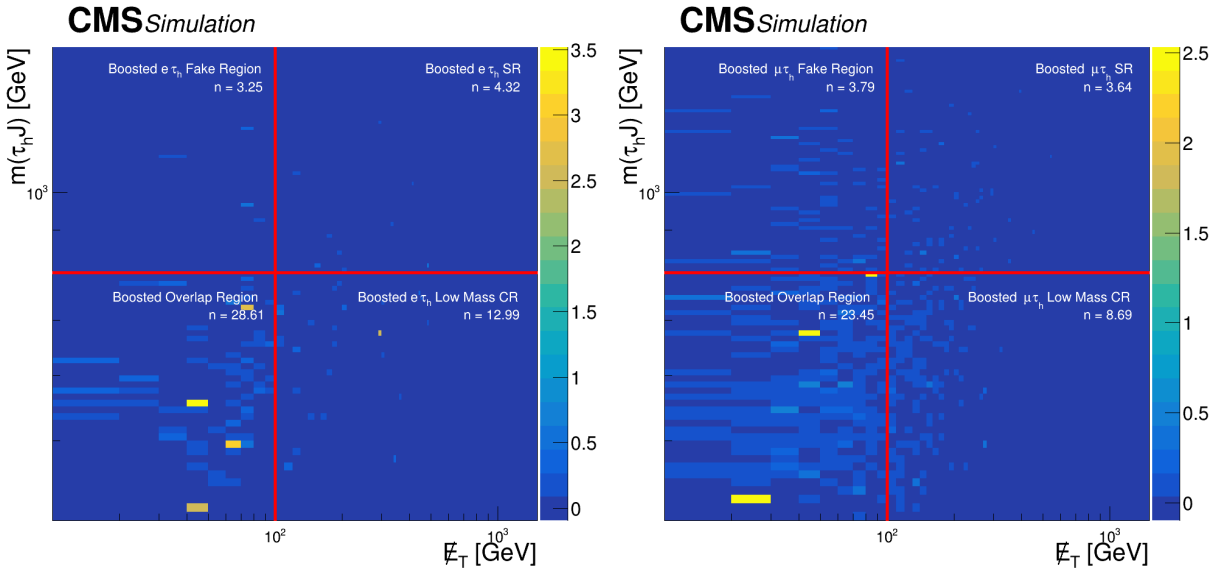

Figure 42: Number of prompt background events in each boosted regions with cutting the mass value of the 4-vector sum of the final state objects.

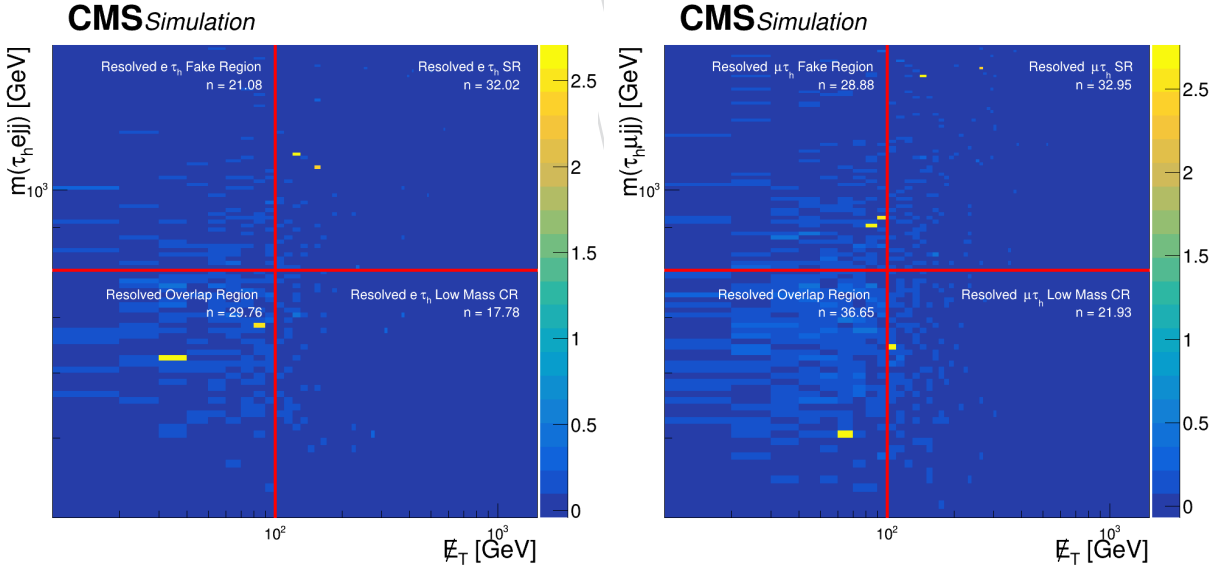

Figure 43: Number of prompt background events in each resolved regions with cutting the mass value of the 4-vector sum of the final state objects.

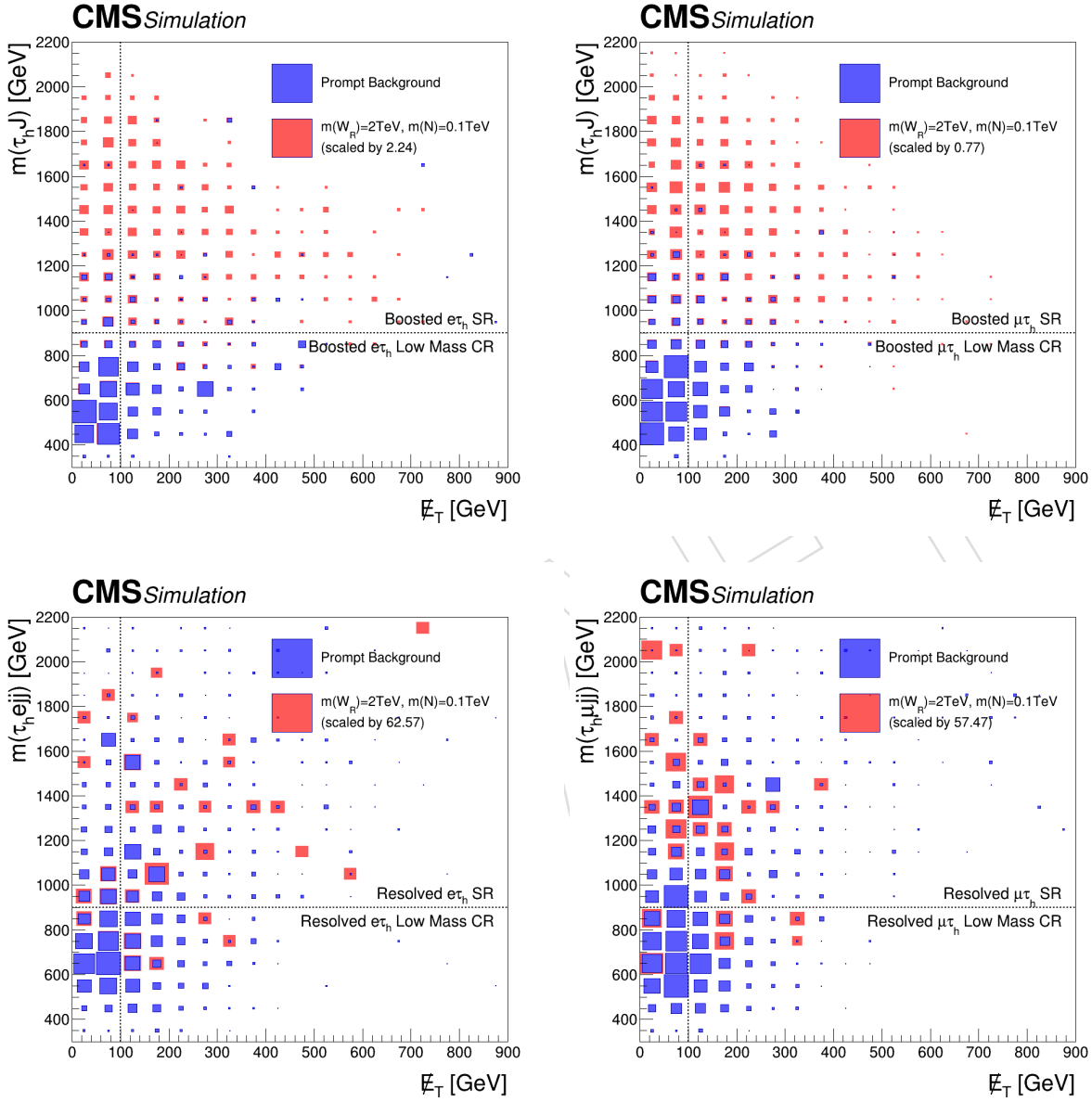

Figure 44: Schematic 2D box plot showing the distribution of missing transverse momentum and the effective mass for prompt backgrounds (blue) and signals (red) with $m(W_R) = 2\,\text{TeV}$ and $m(N) = 100\,\text{GeV}$ in boosted (resolved) regions in the upper (lower) row and electron (muon) channels in the left (right) column. The signals are scaled to match the number of background events to emphasize the shape difference of the distribution.

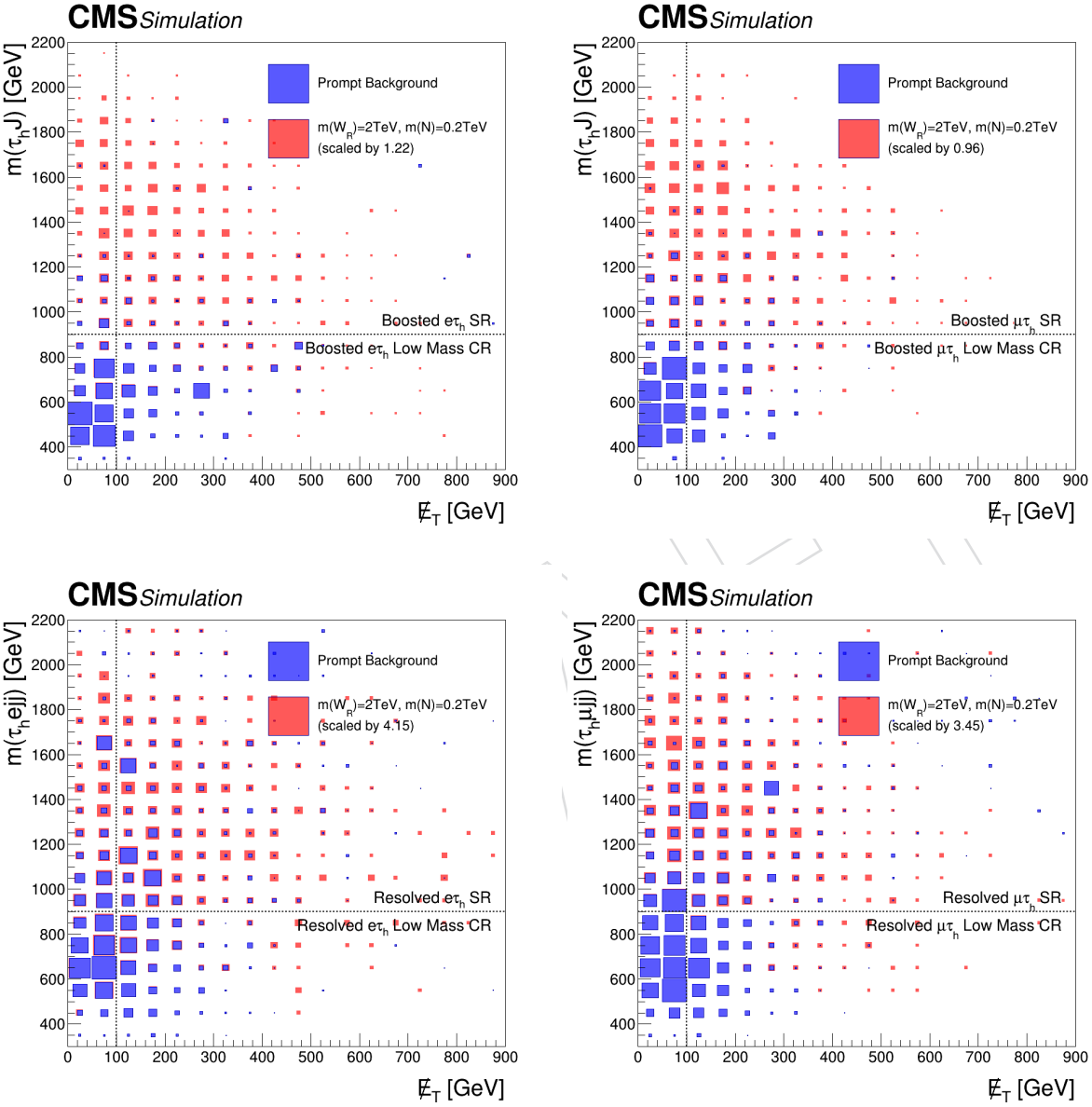

Figure 45: Schematic 2D box plot showing the distribution of missing transverse momentum and the effective mass for prompt backgrounds (blue) and signals (red) with $m(W_R) = 2\,\text{TeV}$ and $m(N) = 200\,\text{GeV}$ in boosted (resolved) regions in the upper (lower) row and electron (muon) channels in the left (right) column. The signals are scaled to match the number of background events to emphasize the shape difference of the distribution.

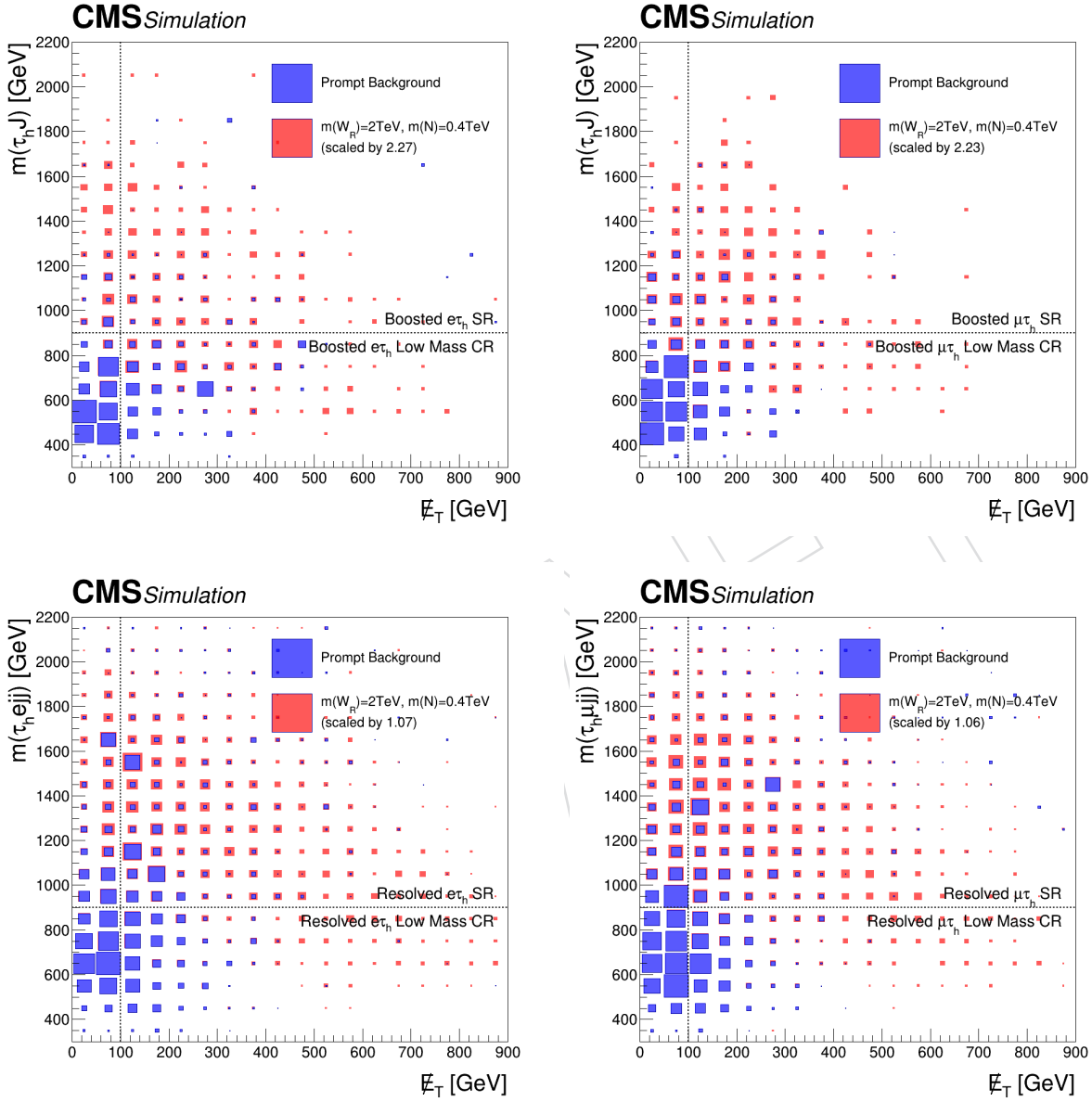

Figure 46: Schematic 2D box plot showing the distribution of missing transverse momentum and the effective mass for prompt backgrounds (blue) and signals (red) with $m(W_R) = 2\,\text{TeV}$ and $m(N) = 400\,\text{GeV}$ in boosted (resolved) regions in the upper (lower) row and electron (muon) channels in the left (right) column. The signals are scaled to match the number of background events to emphasize the shape difference of the distribution.

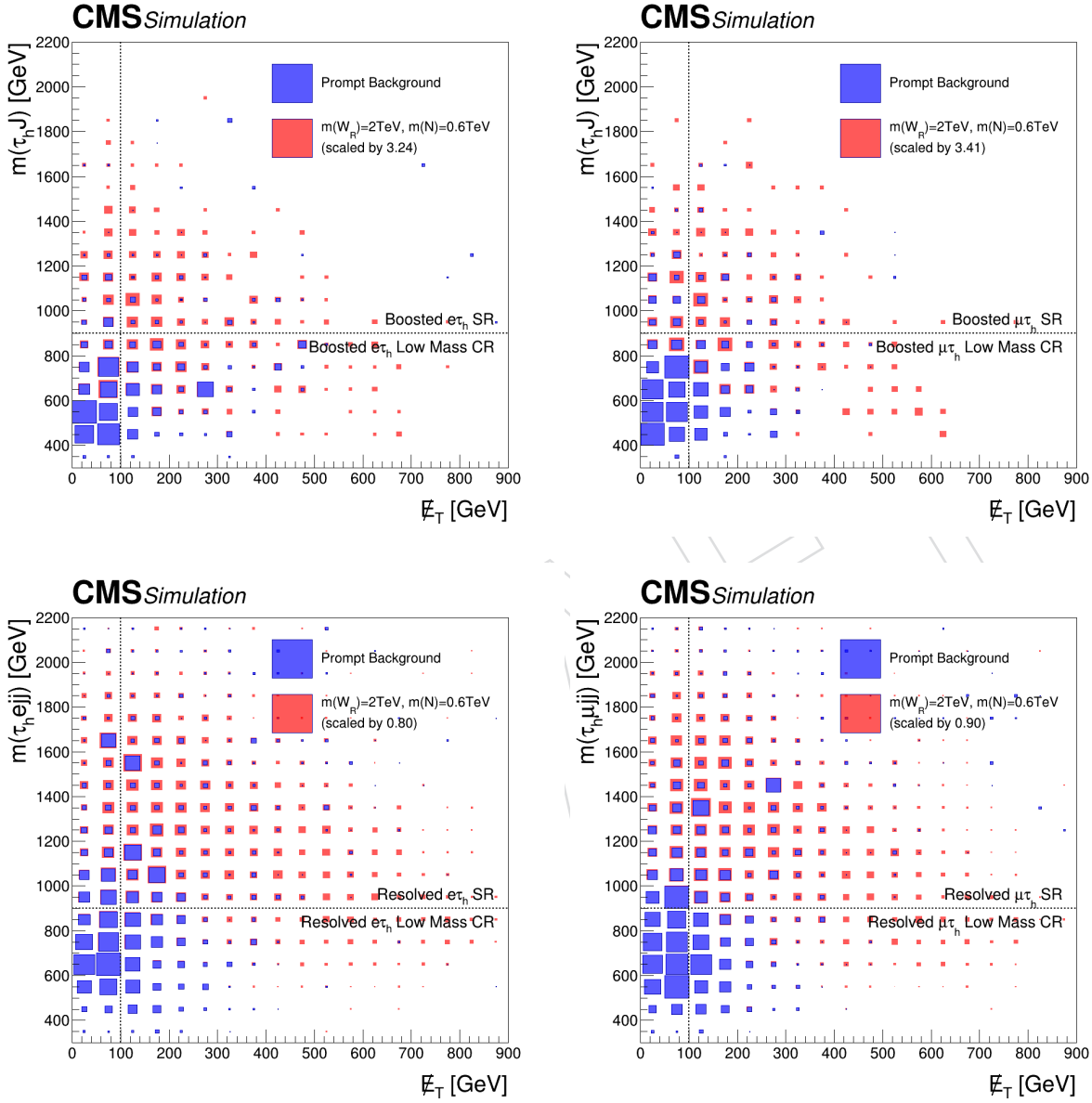

Figure 47: Schematic 2D box plot showing the distribution of missing transverse momentum and the effective mass for prompt backgrounds (blue) and signals (red) with $m(W_R) = 2\,\text{TeV}$ and $m(N) = 600\,\text{GeV}$ in boosted (resolved) regions in the upper (lower) row and electron (muon) channels in the left (right) column. The signals are scaled to match the number of background events to emphasize the shape difference of the distribution.

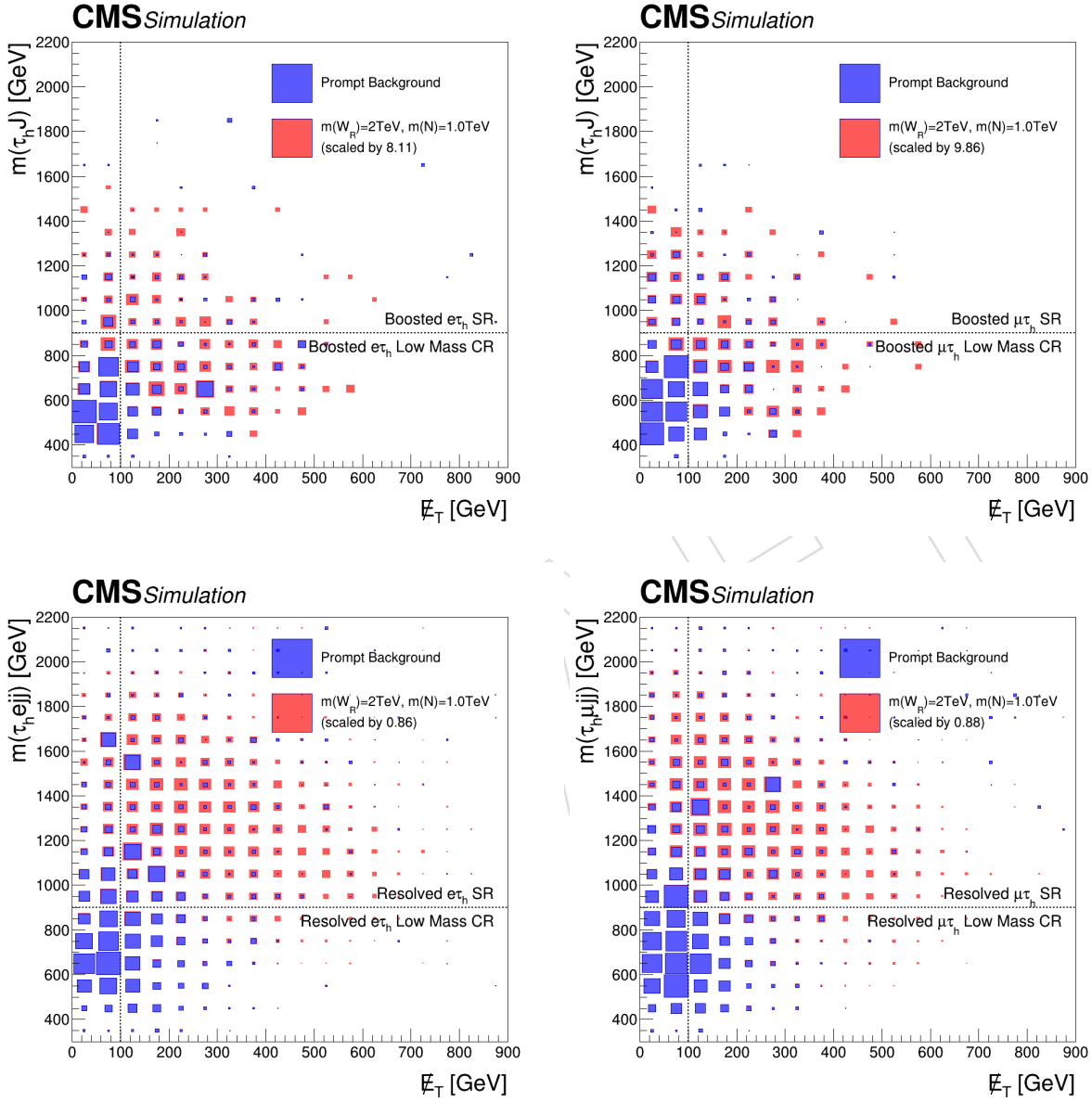

Figure 48: Schematic 2D box plot showing the distribution of missing transverse momentum and the effective mass for prompt backgrounds (blue) and signals (red) with $m(W_R) = 2\,\text{TeV}$ and $m(N) = 1000\,\text{GeV}$ in boosted (resolved) regions in the upper (lower) row and electron (muon) channels in the left (right) column. The signals are scaled to match the number of background events to emphasize the shape difference of the distribution.

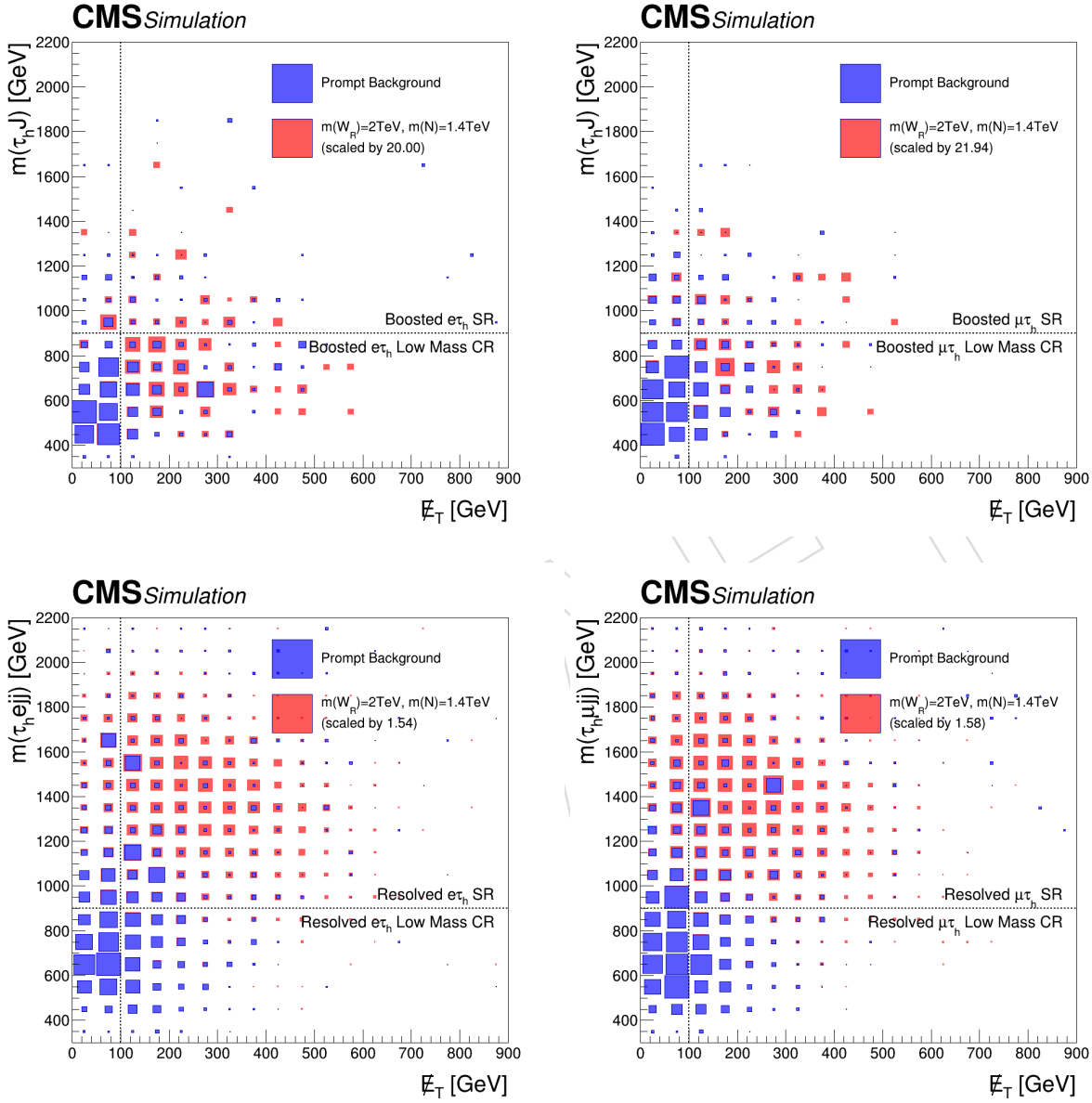

Figure 49: Schematic 2D box plot showing the distribution of missing transverse momentum and the effective mass for prompt backgrounds (blue) and signals (red) with $m(W_R) = 2\,\text{TeV}$ and $m(N) = 1400\,\text{GeV}$ in boosted (resolved) regions in the upper (lower) row and electron (muon) channels in the left (right) column. The signals are scaled to match the number of background events to emphasize the shape difference of the distribution.

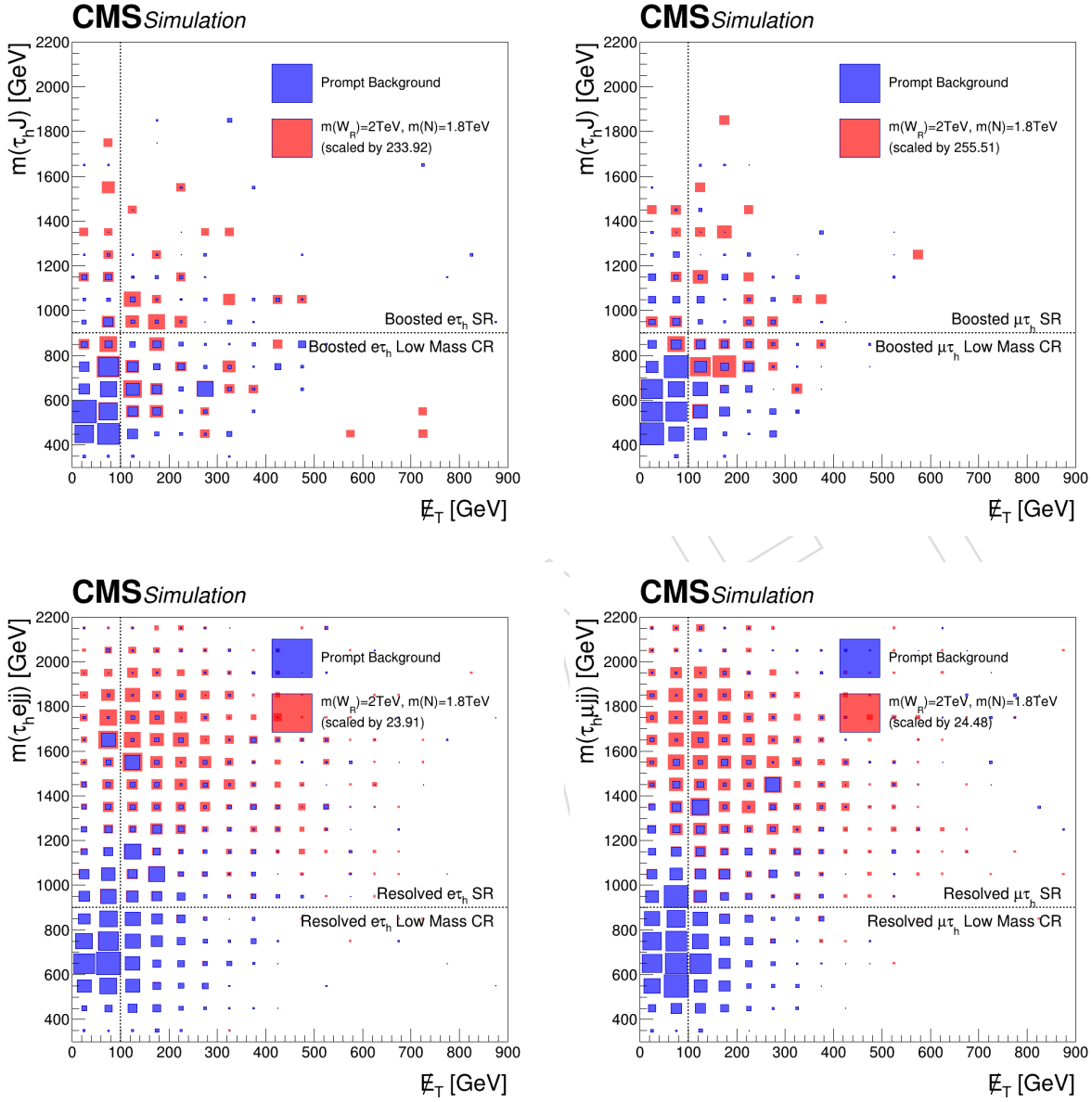

Figure 50: Schematic 2D box plot showing the distribution of missing transverse momentum and the effective mass for prompt backgrounds (blue) and signals (red) with $m(W_R) = 2\,\text{TeV}$ and $m(N) = 1800\,\text{GeV}$ in boosted (resolved) regions in the upper (lower) row and electron (muon) channels in the left (right) column. The signals are scaled to match the number of background events to emphasize the shape difference of the distribution.

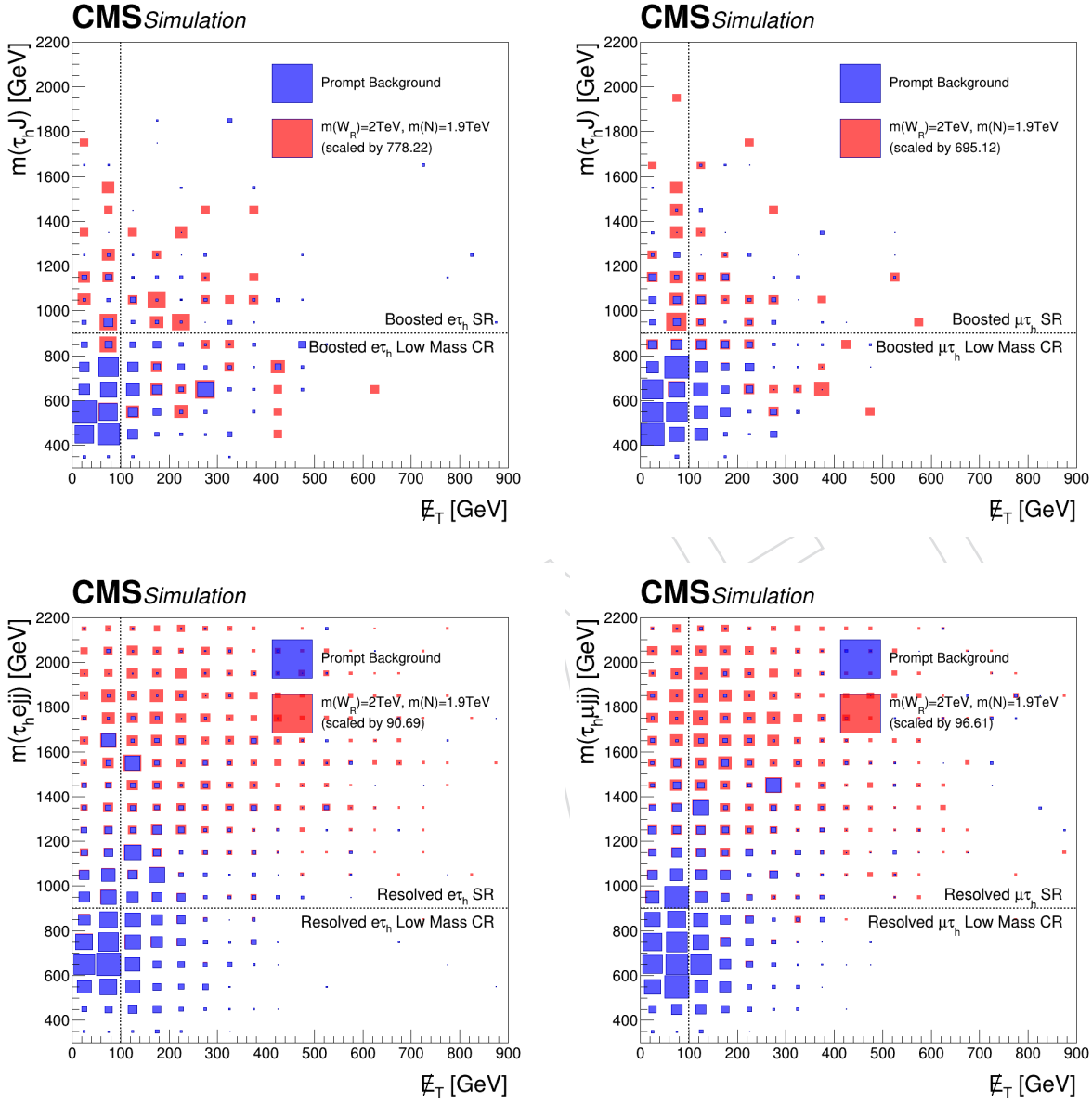

Figure 51: Schematic 2D box plot showing the distribution of missing transverse momentum and the effective mass for prompt backgrounds (blue) and signals (red) with $m(W_R) = 2\,\text{TeV}$ and $m(N) = 1900\,\text{GeV}$ in boosted (resolved) regions in the upper (lower) row and electron (muon) channels in the left (right) column. The signals are scaled to match the number of background events to emphasize the shape difference of the distribution.

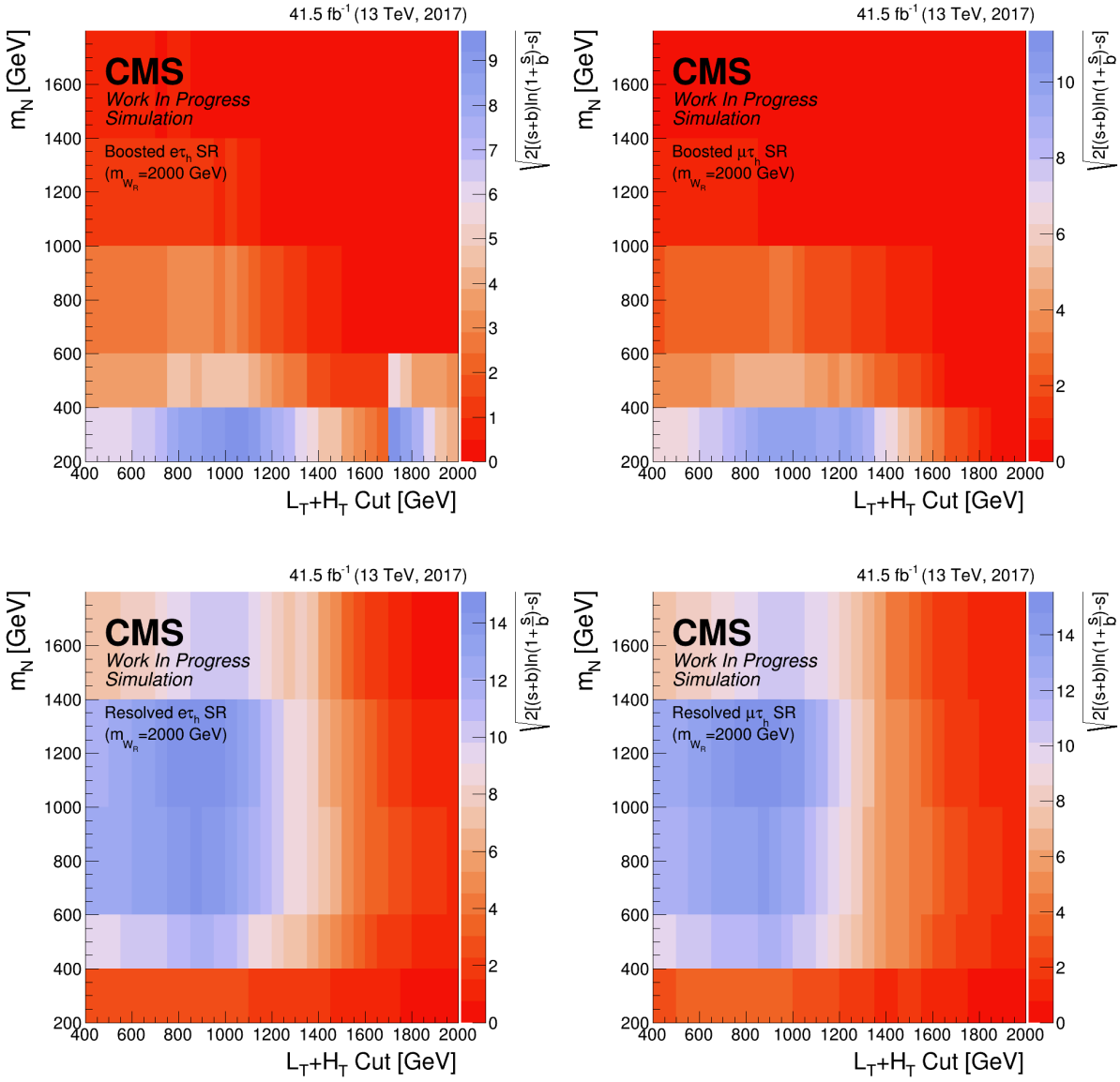

Figure 52: Significance of signals with the W_R mass fixed as 2 TeV with different N masses while differing the mass cut for each signal regions. Here the mass variable $L_T + H_T$ is defined as the p_T sum of all light leptons, hadronic taus and jets.

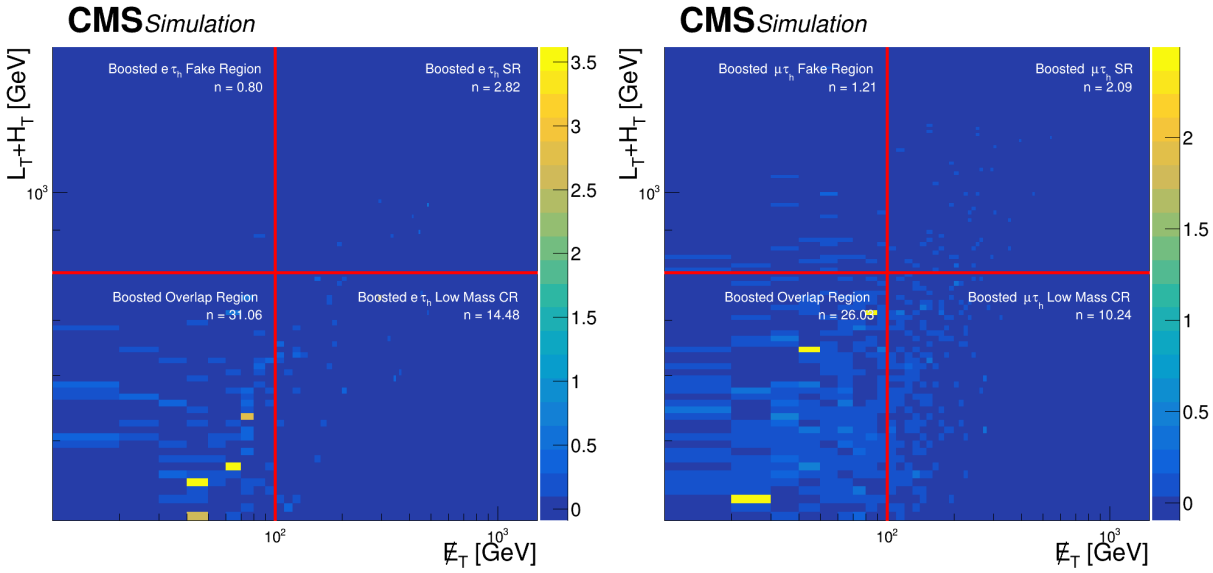

Figure 53: Number of prompt background events in each boosted regions with cutting $L_T + H_T$.

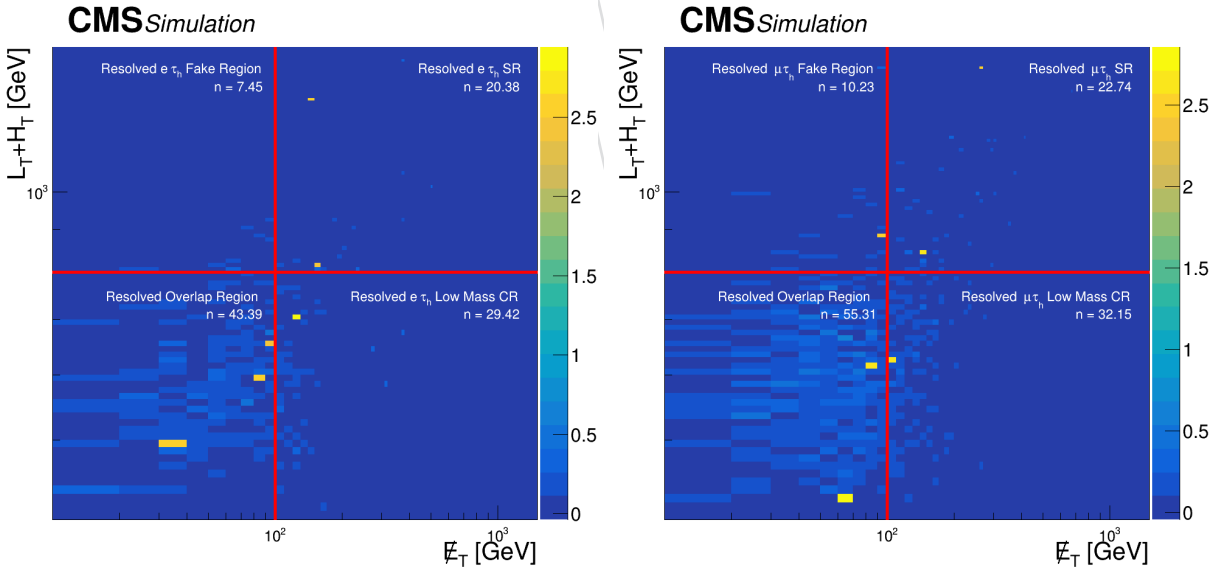

Figure 54: Number of prompt background events in each resolved regions with cutting $L_T + H_T$.

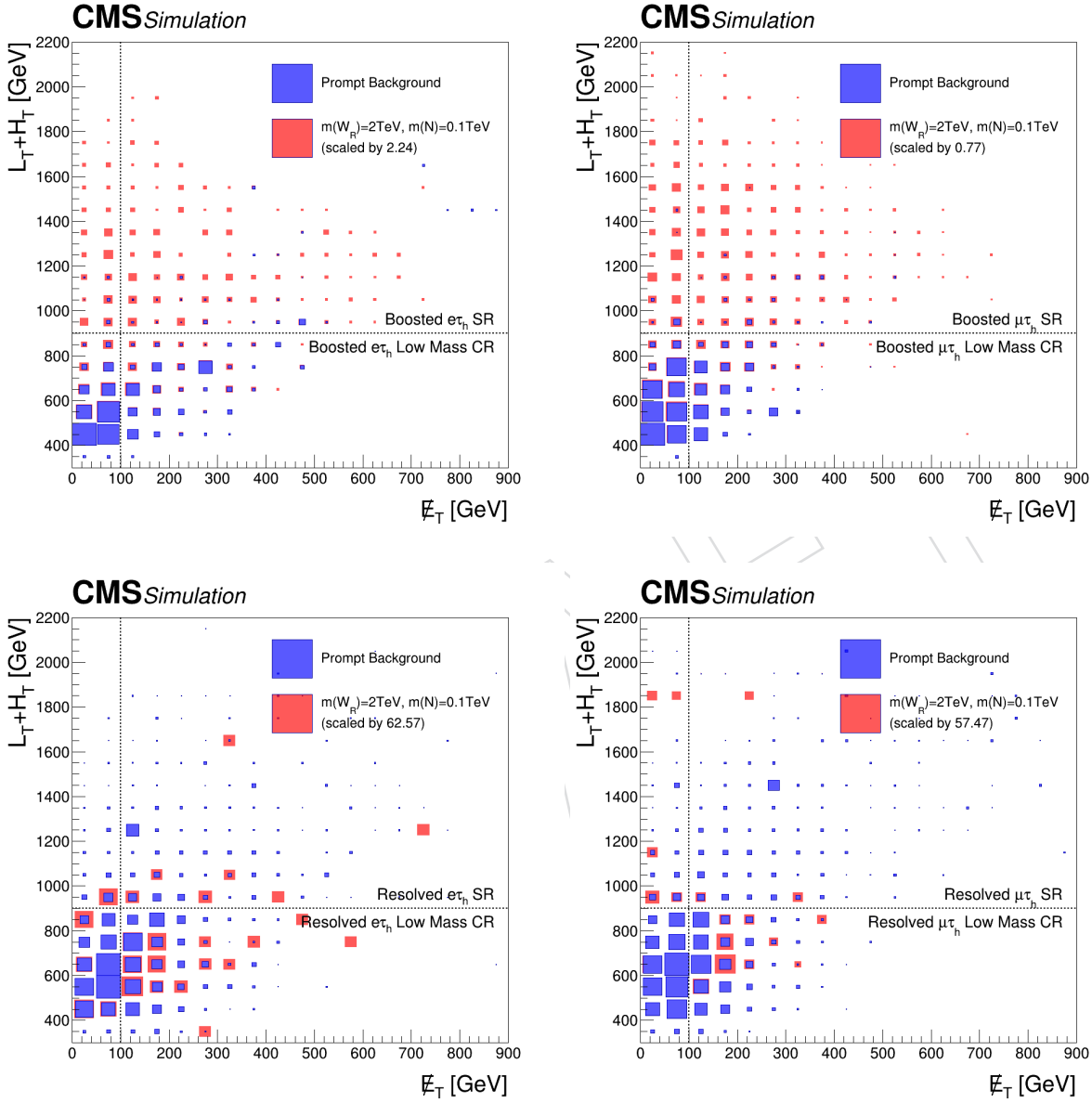

Figure 55: Schematic 2D box plot showing the distribution of missing transverse momentum and $L_T + H_T$ for prompt backgrounds (blue) and signals (red) with $m(W_R) = 2\,\text{TeV}$ and $m(N) = 100\,\text{GeV}$ in boosted (resolved) regions in the upper (lower) row and electron (muon) channels in the left (right) column. The signals are scaled to match the number of background events to emphasize the shape difference of the distribution.

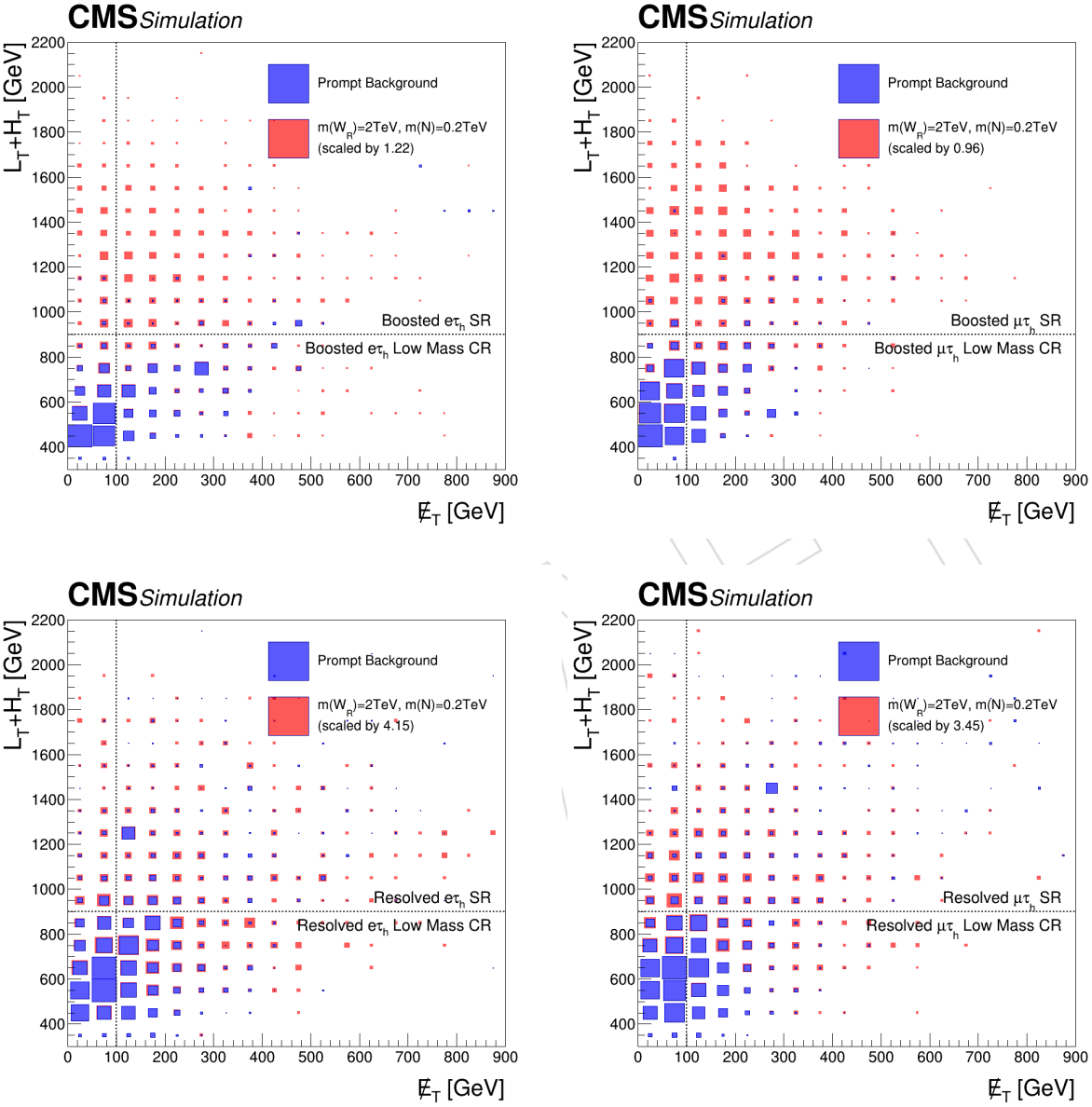

Figure 56: Schematic 2D box plot showing the distribution of missing transverse momentum and $L_T + H_T$ for prompt backgrounds (blue) and signals (red) with $m(W_R) = 2\,\text{TeV}$ and $m(N) = 200\,\text{GeV}$ in boosted (resolved) regions in the upper (lower) row and electron (muon) channels in the left (right) column. The signals are scaled to match the number of background events to emphasize the shape difference of the distribution.

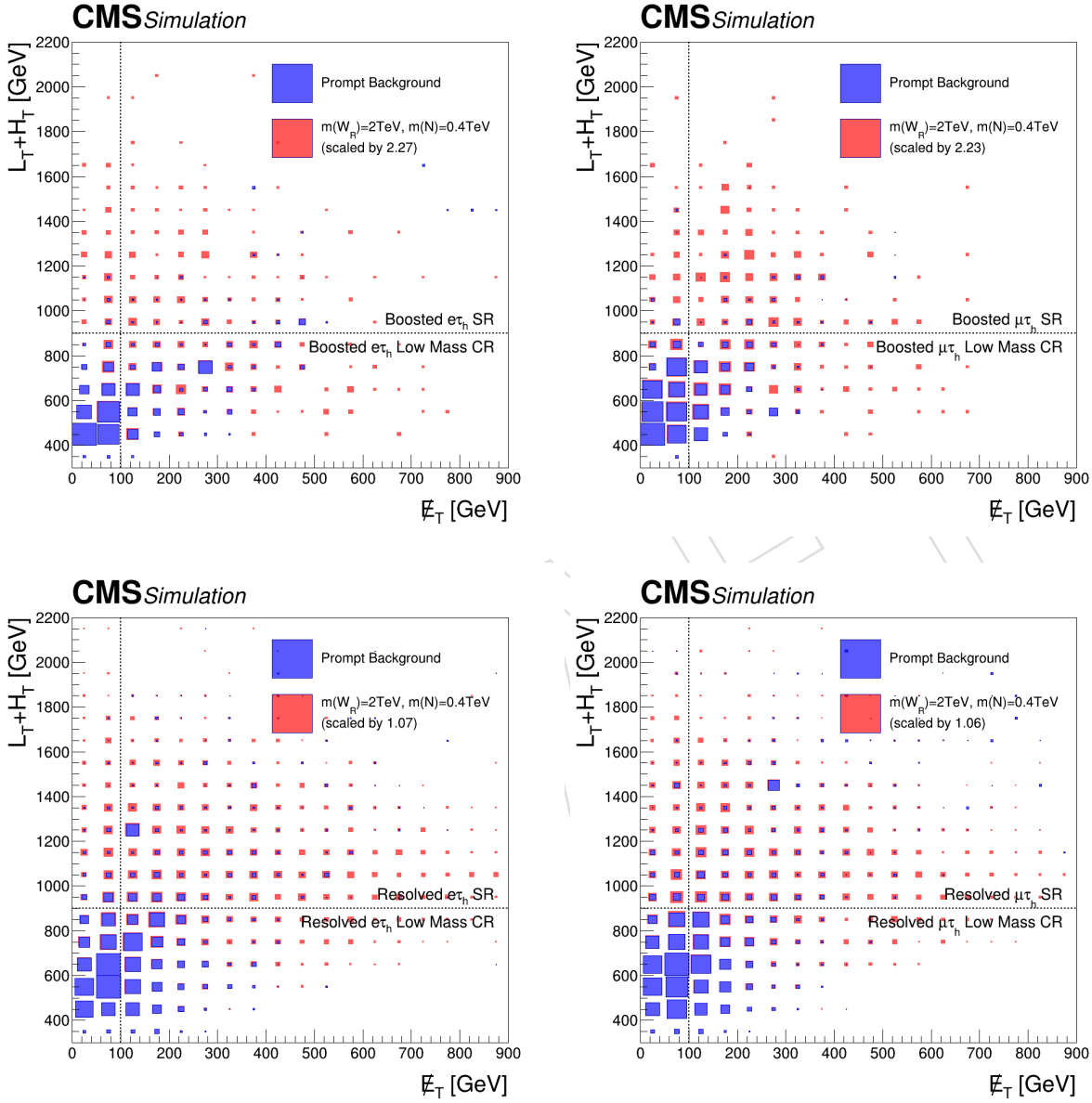

Figure 57: Schematic 2D box plot showing the distribution of missing transverse momentum and $L_T + H_T$ for prompt backgrounds (blue) and signals (red) with $m(W_R) = 2\,\text{TeV}$ and $m(N) = 400\,\text{GeV}$ in boosted (resolved) regions in the upper (lower) row and electron (muon) channels in the left (right) column. The signals are scaled to match the number of background events to emphasize the shape difference of the distribution.

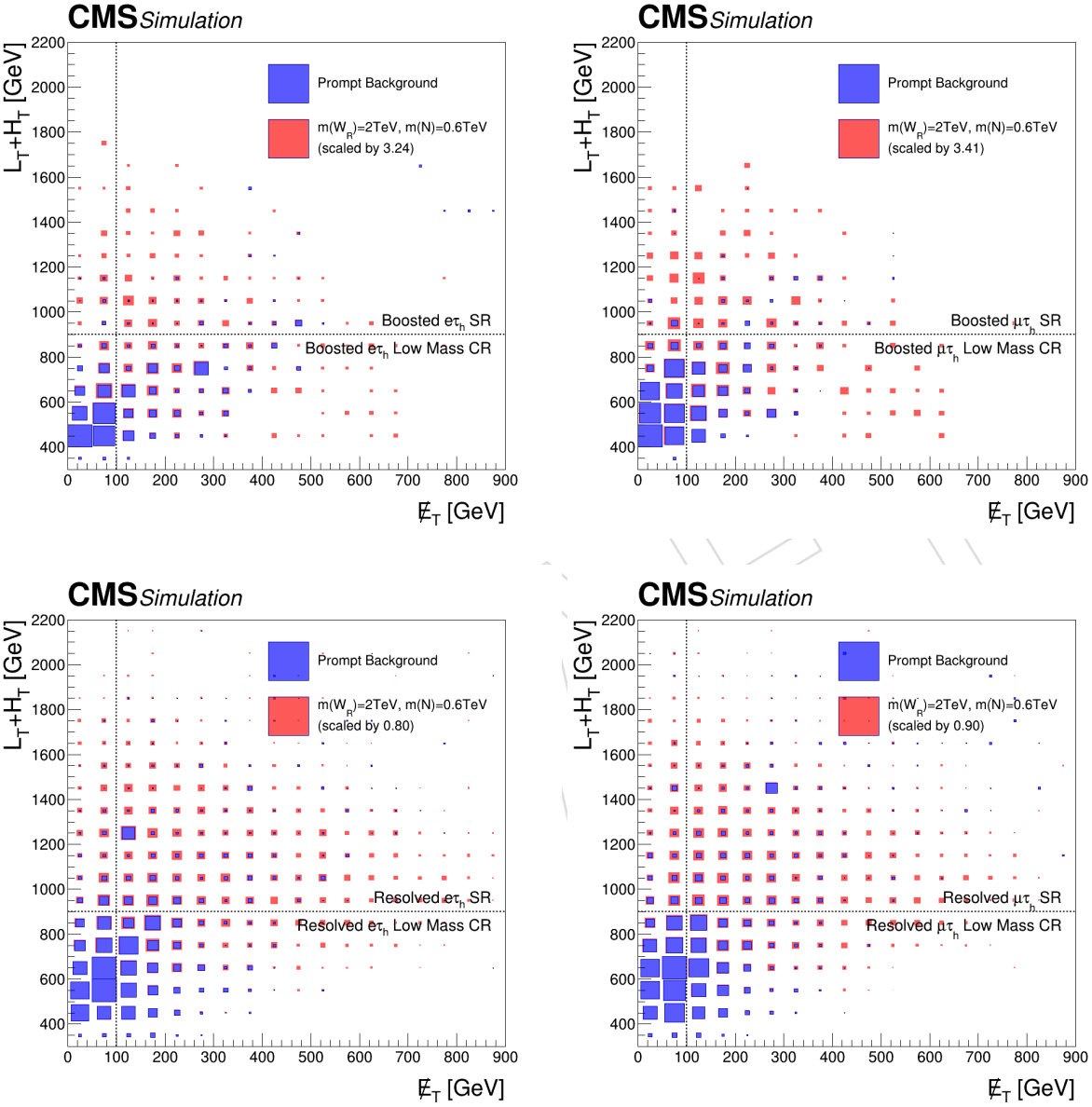

Figure 58: Schematic 2D box plot showing the distribution of missing transverse momentum and $L_T + H_T$ for prompt backgrounds (blue) and signals (red) with $m(W_R) = 2\,\text{TeV}$ and $m(N) = 600\,\text{GeV}$ in boosted (resolved) regions in the upper (lower) row and electron (muon) channels in the left (right) column. The signals are scaled to match the number of background events to emphasize the shape difference of the distribution.

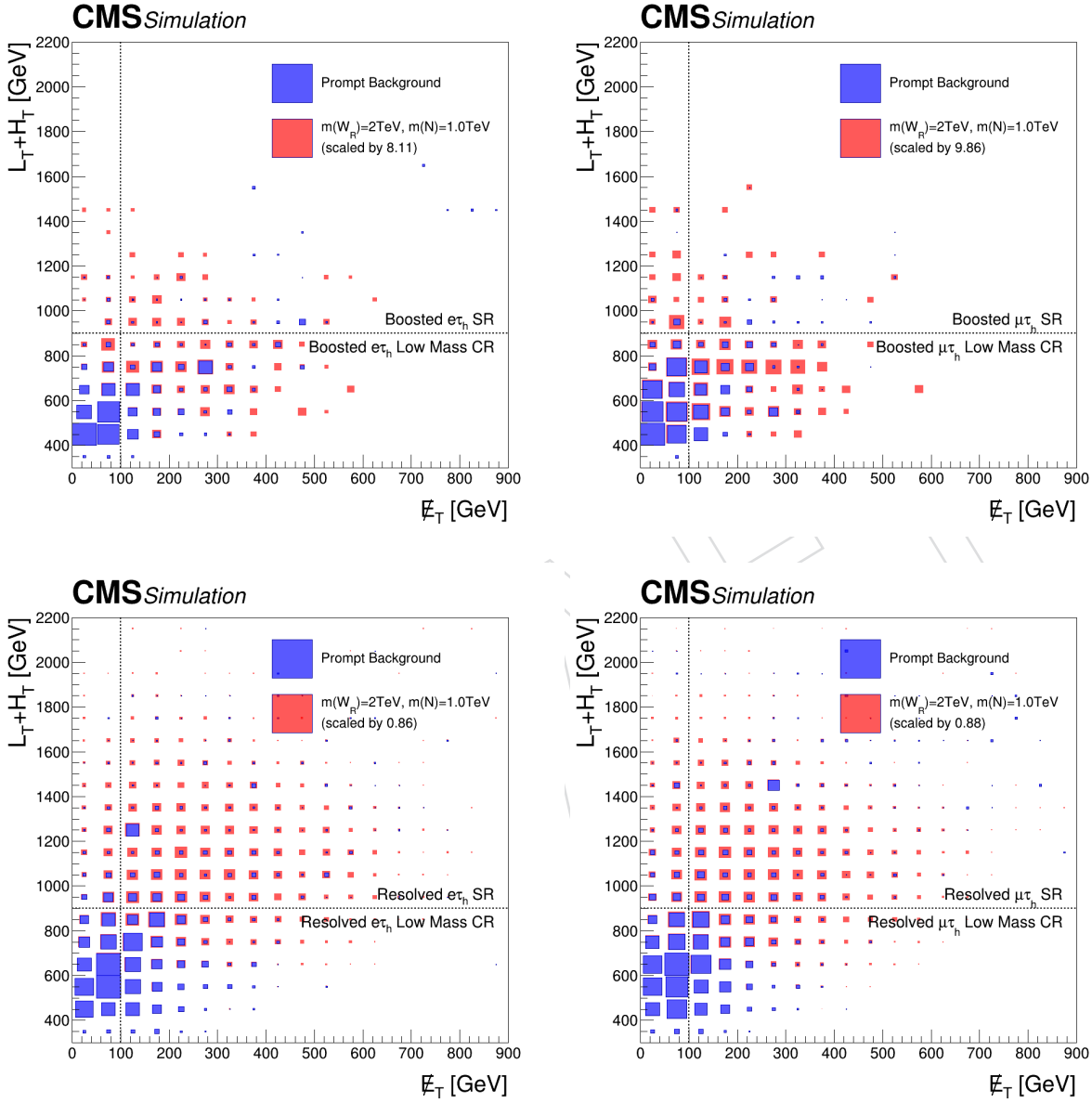

Figure 59: Schematic 2D box plot showing the distribution of missing transverse momentum and $L_T + H_T$ for prompt backgrounds (blue) and signals (red) with $m(W_R) = 2\,\text{TeV}$ and $m(N) = 1000\,\text{GeV}$ in boosted (resolved) regions in the upper (lower) row and electron (muon) channels in the left (right) column. The signals are scaled to match the number of background events to emphasize the shape difference of the distribution.

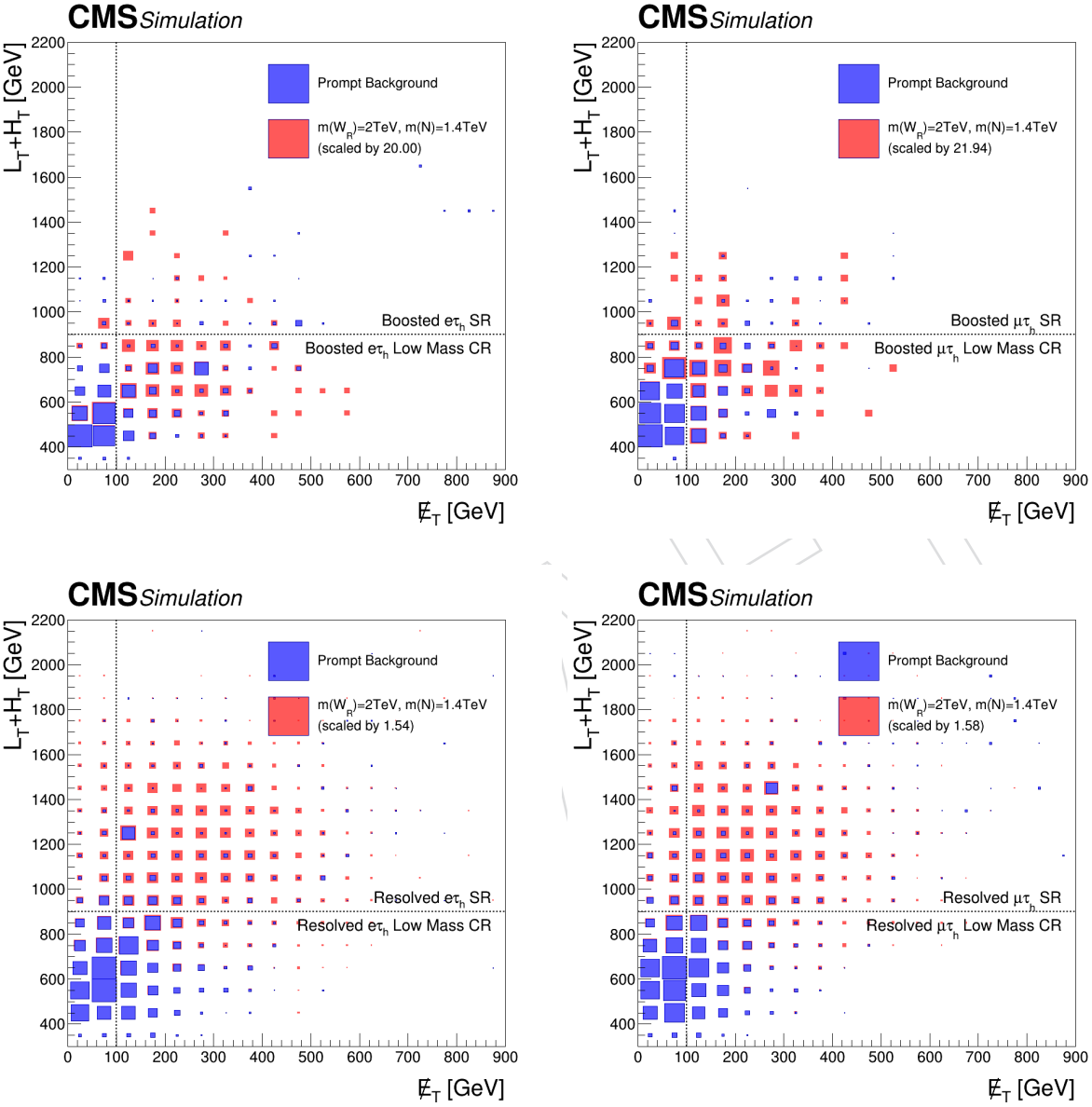

Figure 60: Schematic 2D box plot showing the distribution of missing transverse momentum and $L_T + H_T$ for prompt backgrounds (blue) and signals (red) with $m(W_R) = 2\,\text{TeV}$ and $m(N) = 1400\,\text{GeV}$ in boosted (resolved) regions in the upper (lower) row and electron (muon) channels in the left (right) column. The signals are scaled to match the number of background events to emphasize the shape difference of the distribution.

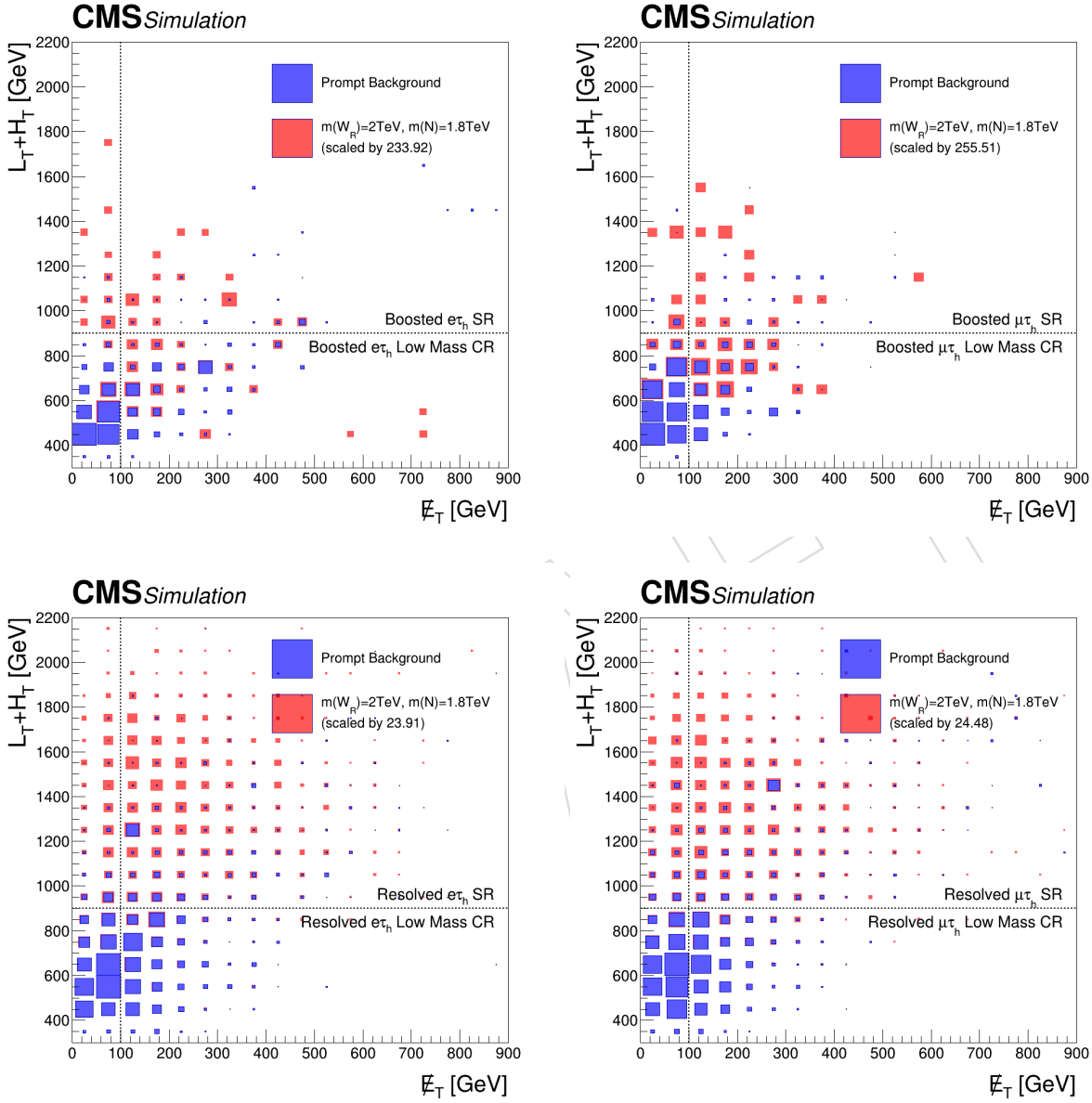

Figure 61: Schematic 2D box plot showing the distribution of missing transverse momentum and $L_T + H_T$ for prompt backgrounds (blue) and signals (red) with $m(W_R) = 2\,\text{TeV}$ and $m(N) = 1800\,\text{GeV}$ in boosted (resolved) regions in the upper (lower) row and electron (muon) channels in the left (right) column. The signals are scaled to match the number of background events to emphasize the shape difference of the distribution.

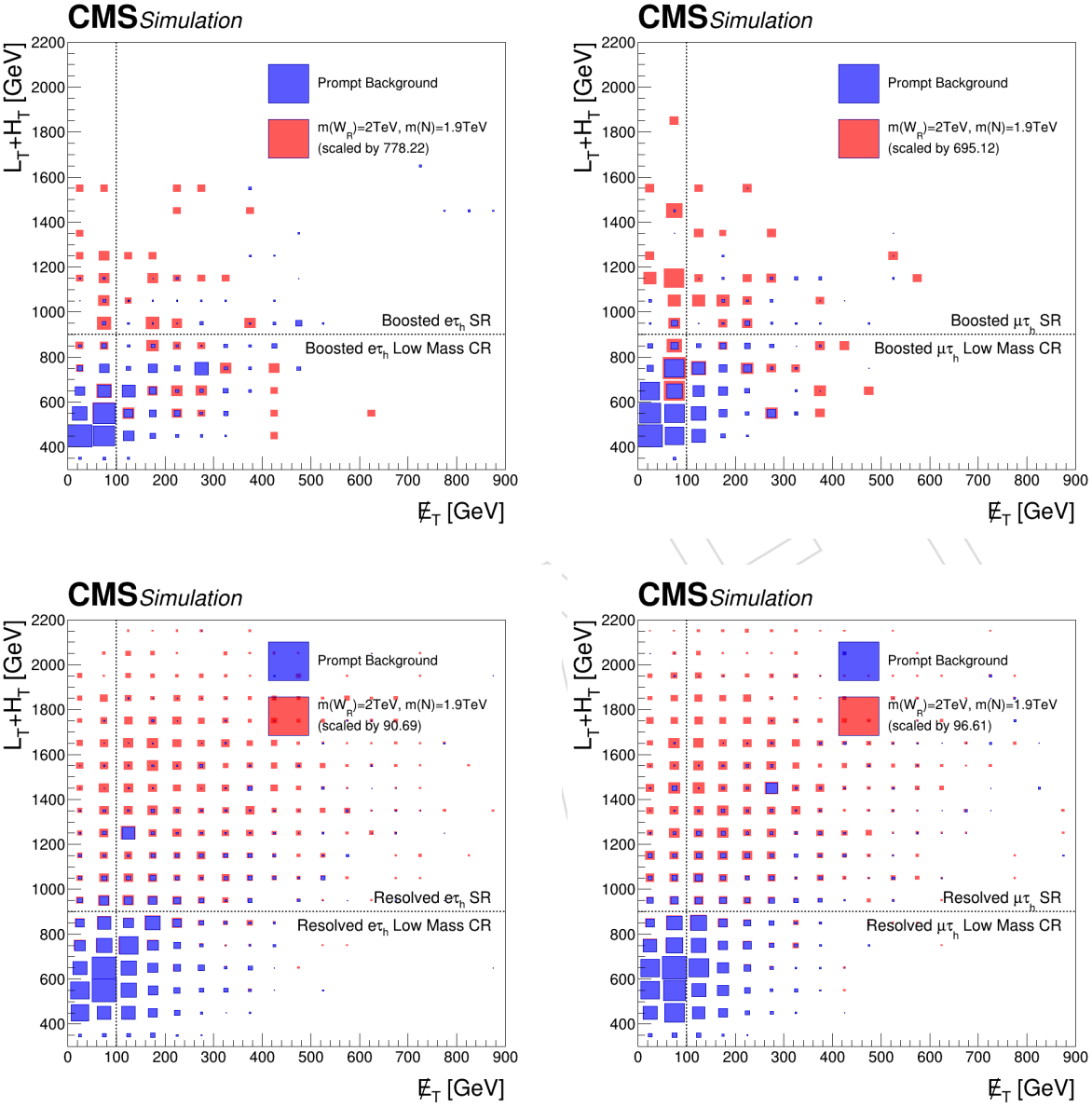

Figure 62: Schematic 2D box plot showing the distribution of missing transverse momentum and $L_T + H_T$ for prompt backgrounds (blue) and signals (red) with $m(W_R) = 2\,\text{TeV}$ and $m(N) = 1900\,\text{GeV}$ in boosted (resolved) regions in the upper (lower) row and electron (muon) channels in the left (right) column. The signals are scaled to match the number of background events to emphasize the shape difference of the distribution.

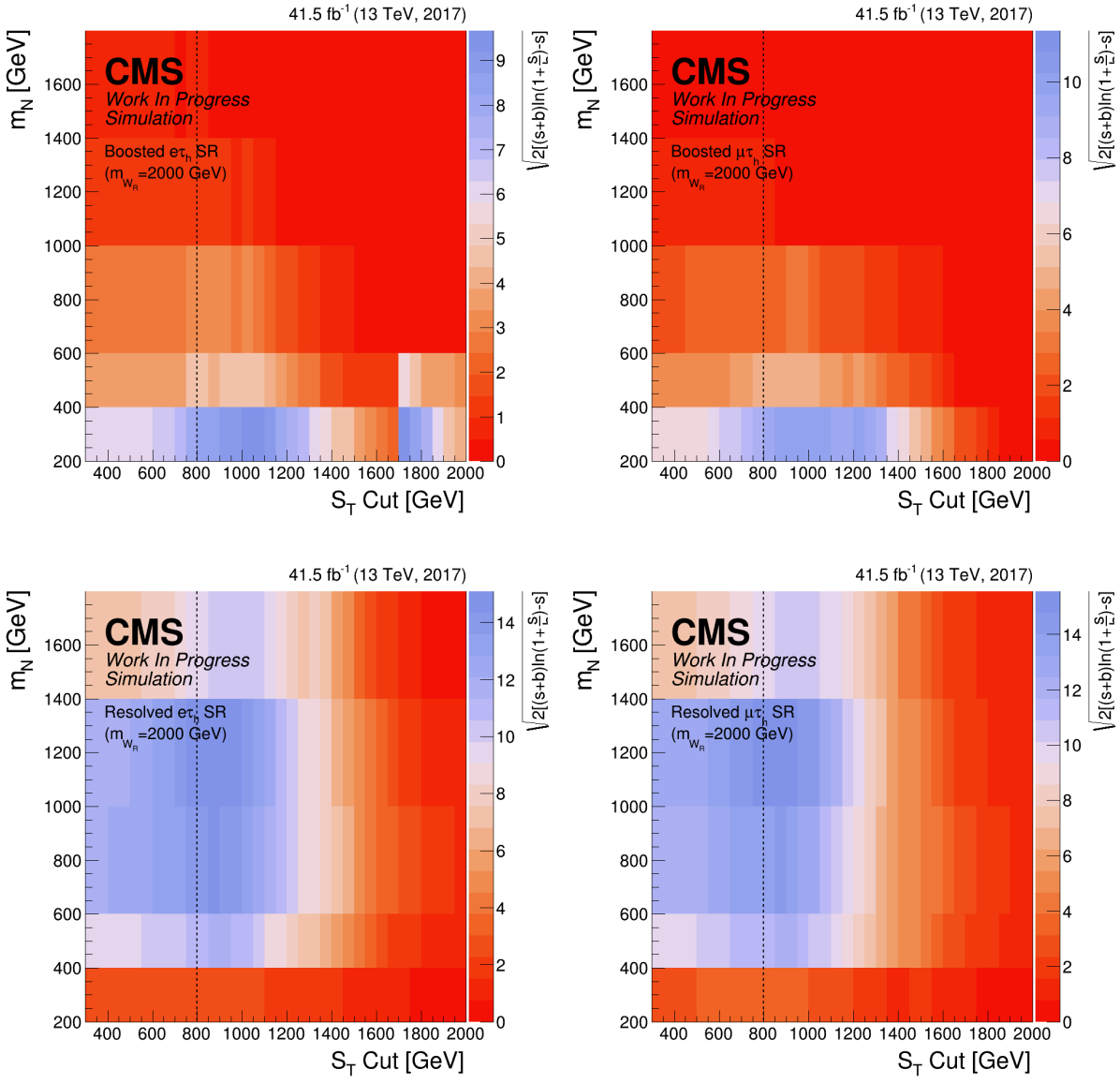

Figure 63: Significance of signals with the W_R mass fixed as 2 TeV with different N masses while differing the mass cut for each signal regions. Here the mass variable S_T is defined as the p_{T} sum of all light leptons, hadronic taus and jets.

513 ## B.2 Optimization of LSF selection

514 # C LSF Validation

515 # D Nonprompt Background Estimation

516 ## D.1 Top Pair MC Fake Factors

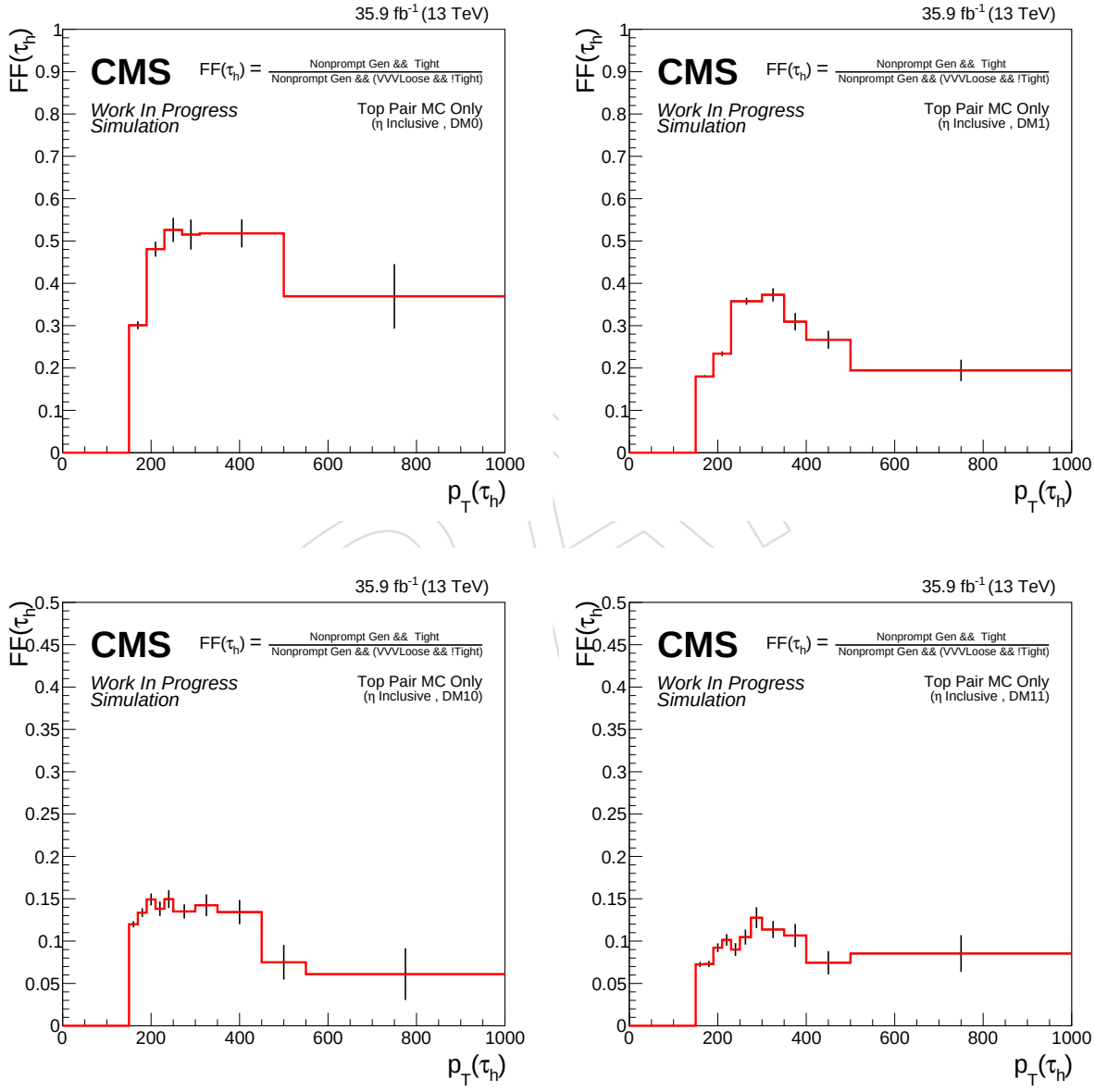

Figure 64: FF_{TT} as a function of hadronic tau p_T divided into its decay modes for 2016 simulations.

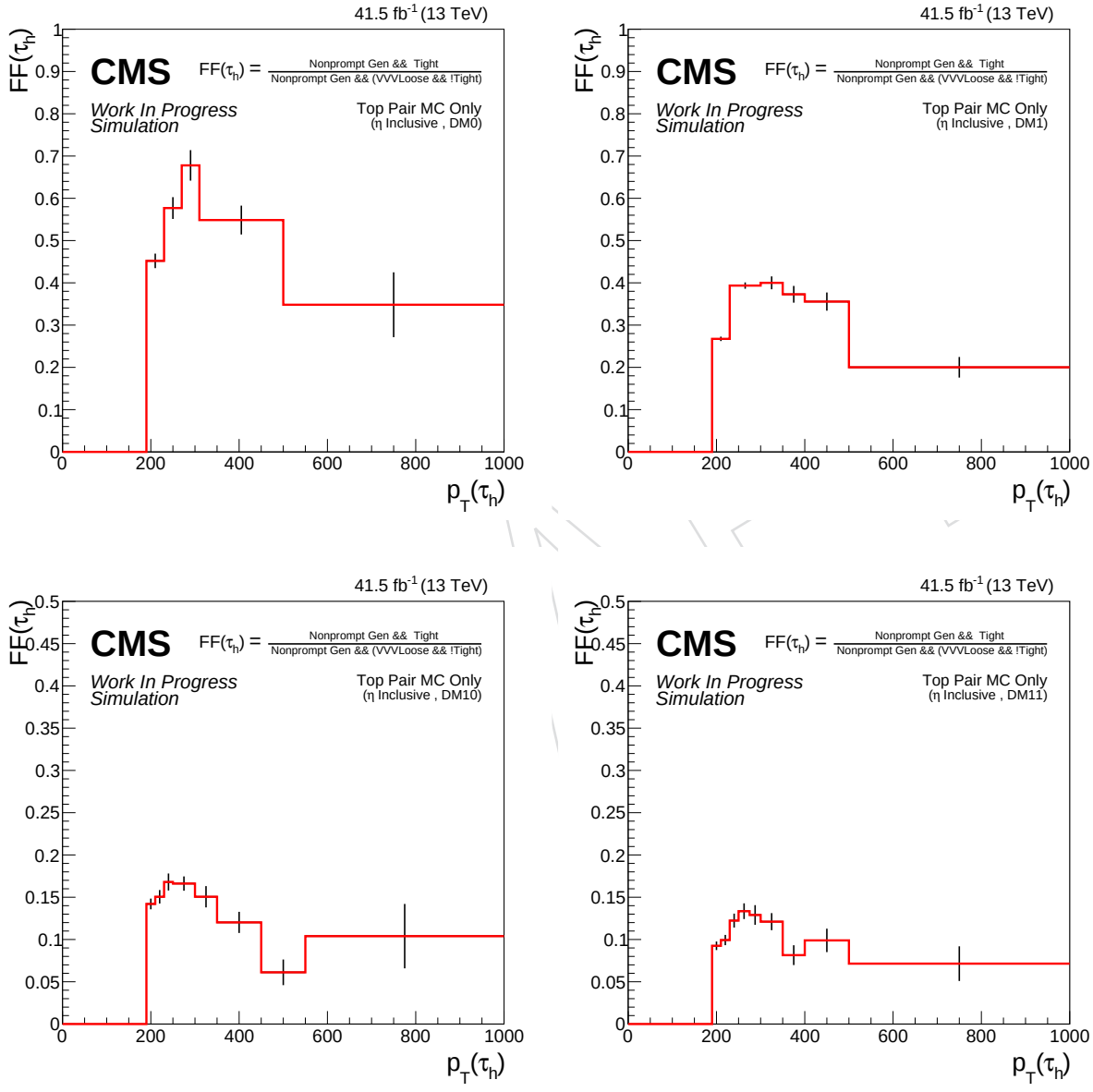

Figure 65: FF_{TT} as a function of hadronic tau p_T divided into its decay modes for 2017 simulations.

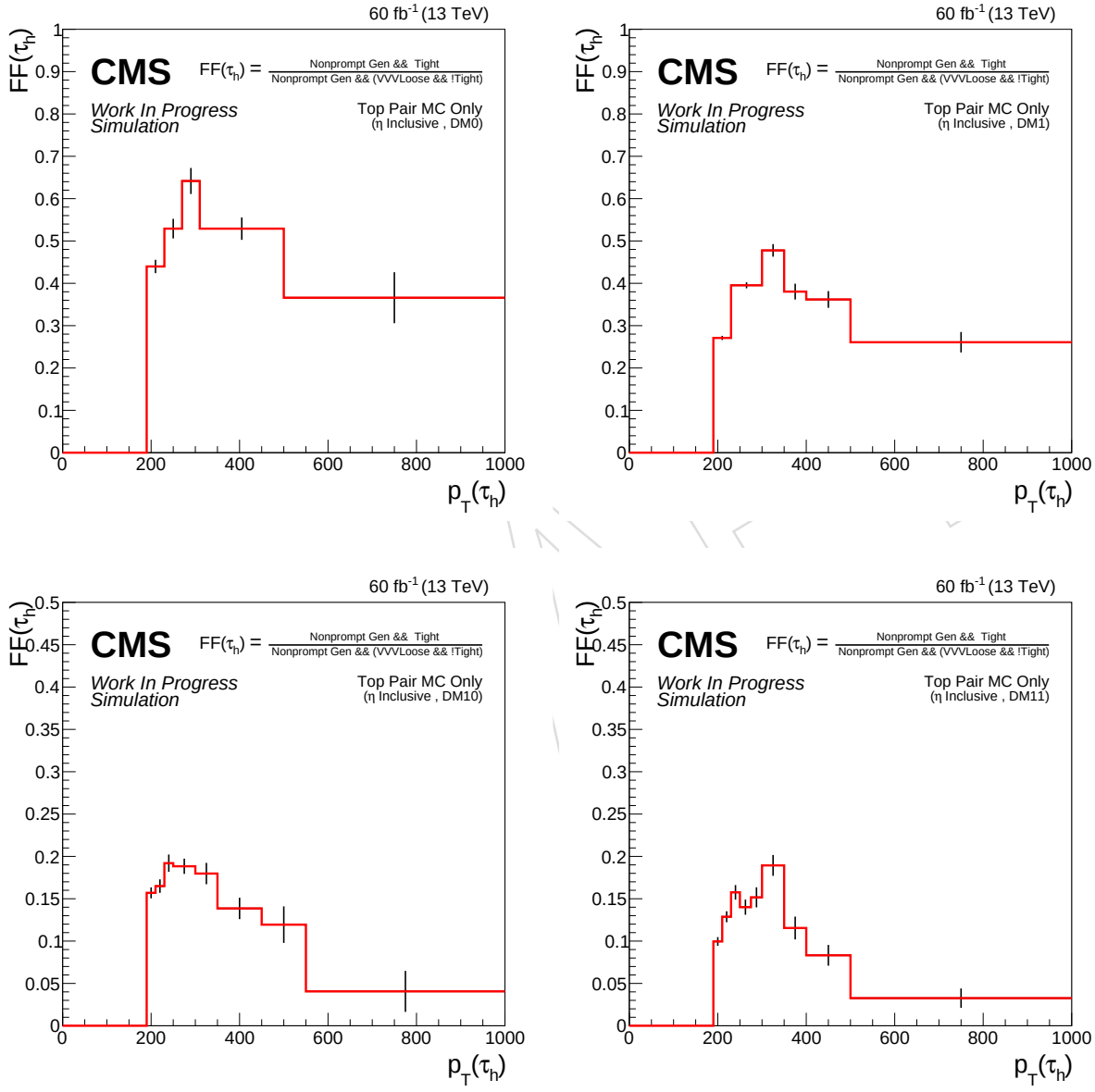

Figure 66: FF_{TT} as a function of hadronic tau p_T divided into its decay modes for 2018 simulations.

D.2 QCD Data Driven Fake Factors

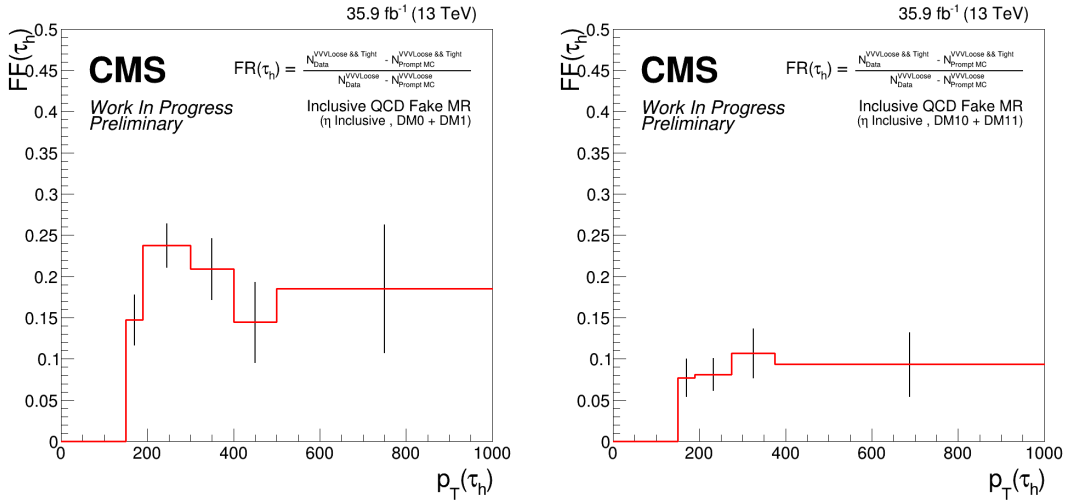

Figure 67: FF_{QCD} as a function of hadronic tau p_T divided into 1 (3) prong decay modes for 2016 data in the QCD Fake MR.

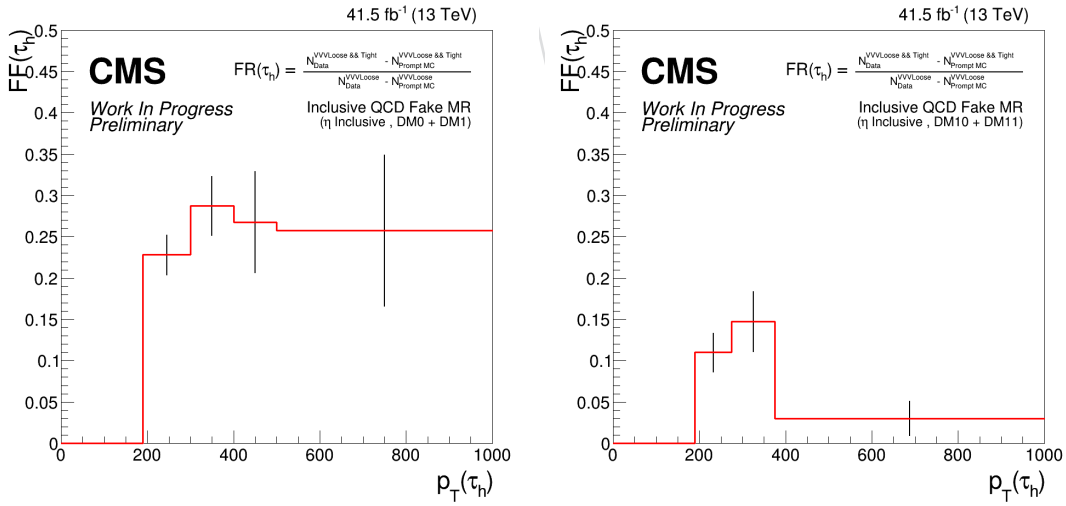

Figure 68: FF_{QCD} as a function of hadronic tau p_T divided into 1 (3) prong decay modes for 2016 data in the QCD Fake MR.

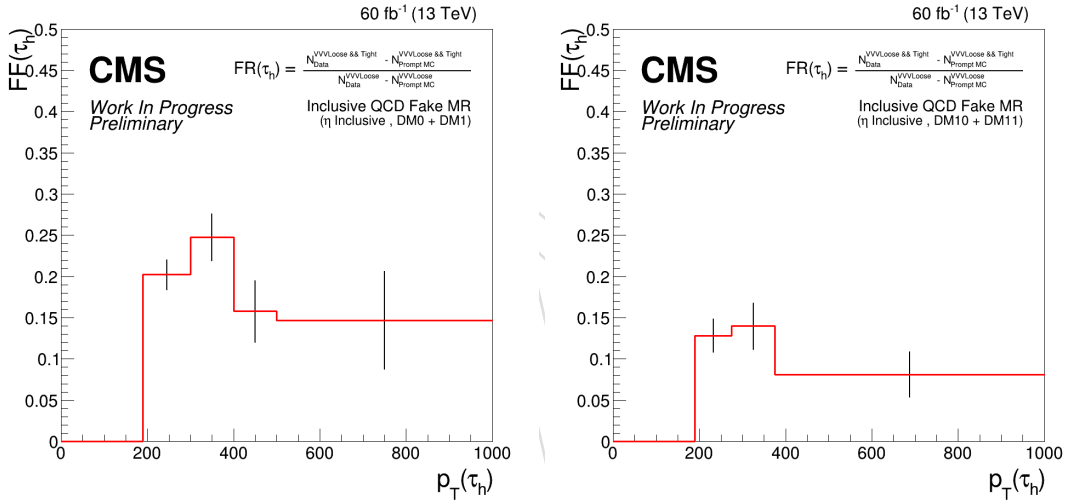

Figure 69: FF_{QCD} as a function of hadronic tau p_T divided into 1 (3) prong decay modes for 2016 data in the QCD Fake MR.

D.3 Application Region Fake Contribution Ratios

D.3.1 Signal Region Application Region ($m_{Eff.}$)

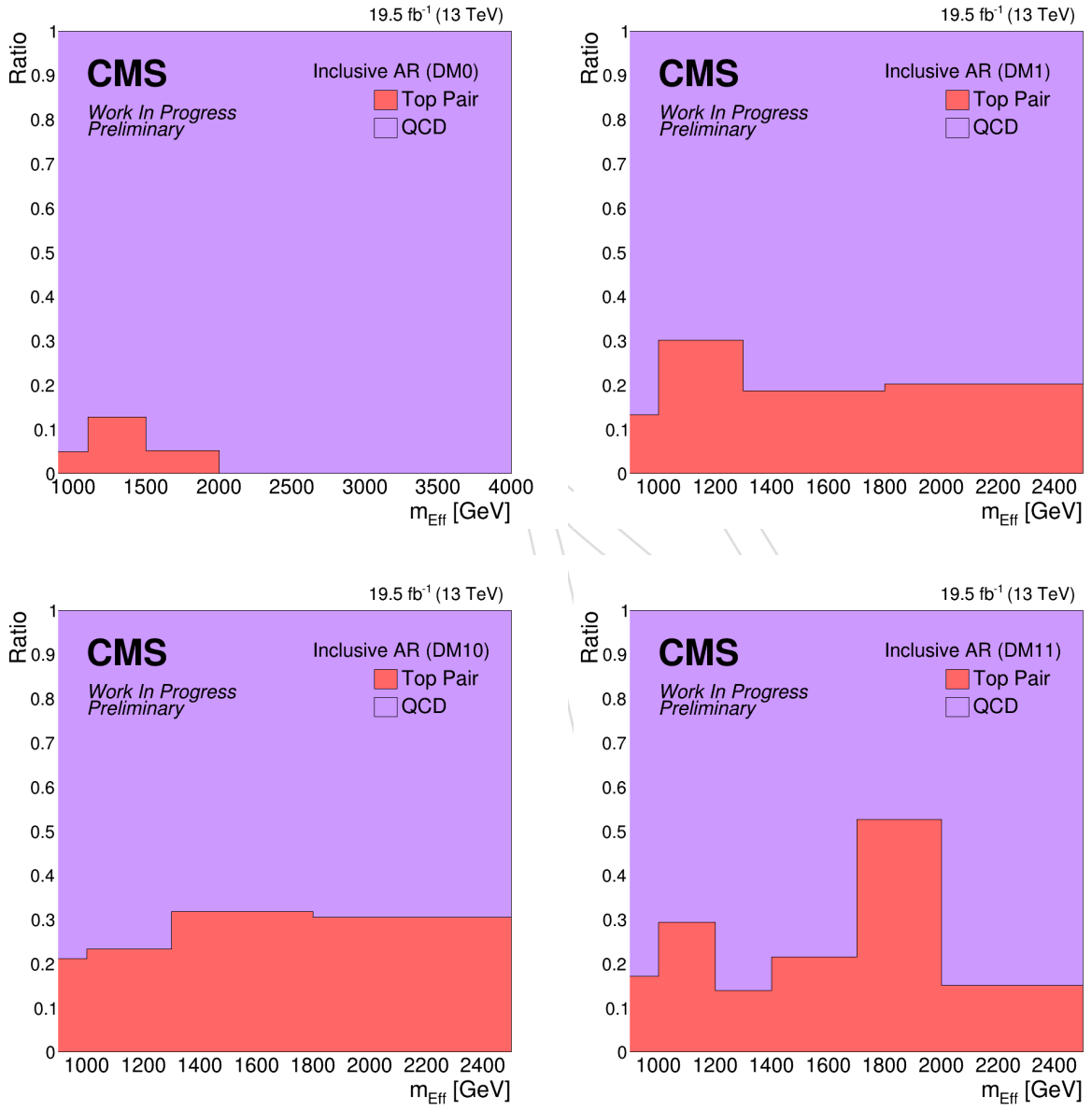

Figure 70: Fractions of the hadronic tau misidentification backgrounds as a function of m_{Eff}, divided by the hadronic tau decay modes used in this analysis in the Run2 UL 2016preVFP era.

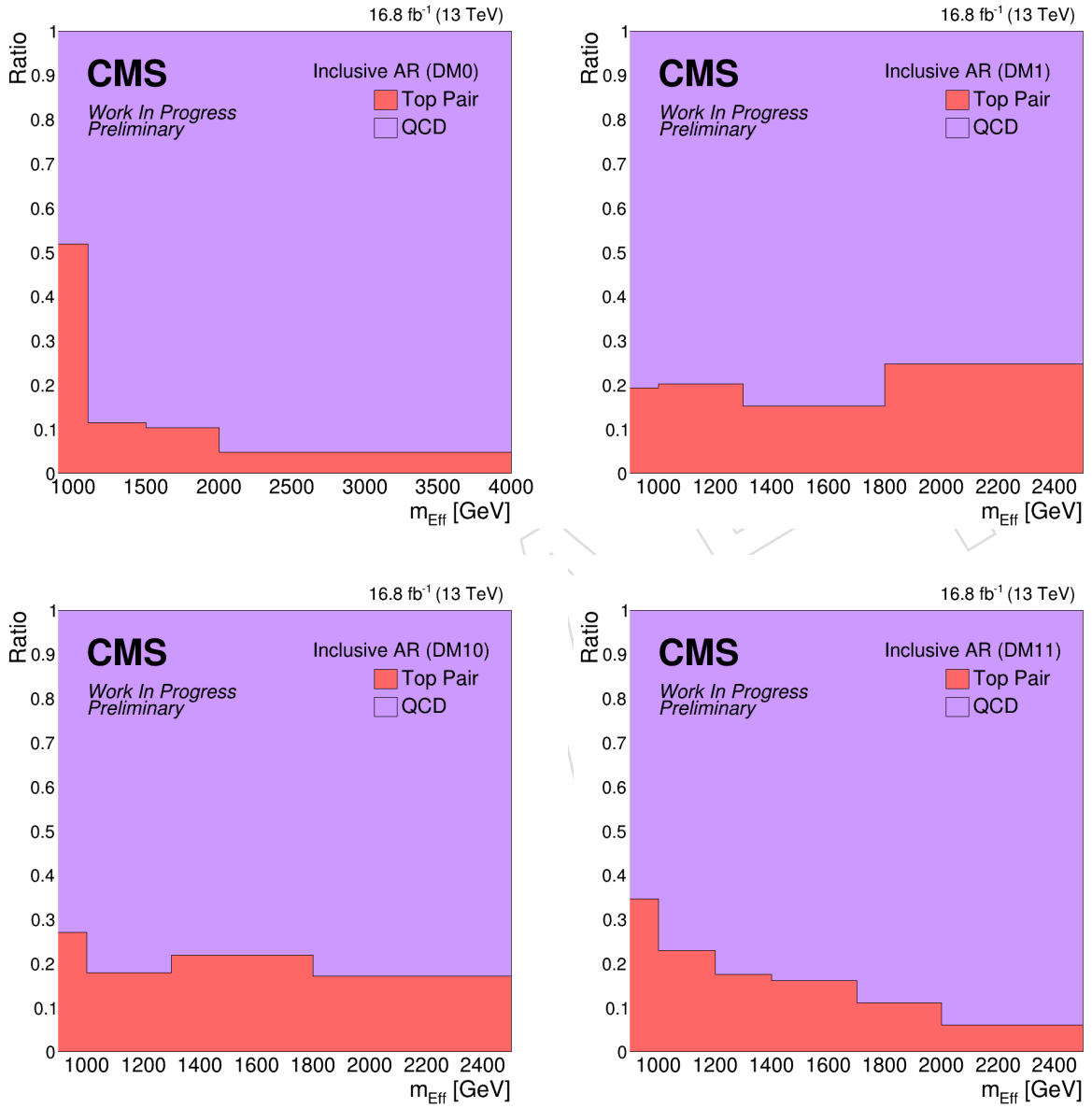

Figure 71: Fractions of the hadronic tau misidentification backgrounds as a function of m_{Eff}, divided by the hadronic tau decay modes used in this analysis in the Run2 UL 2016postVFP era.

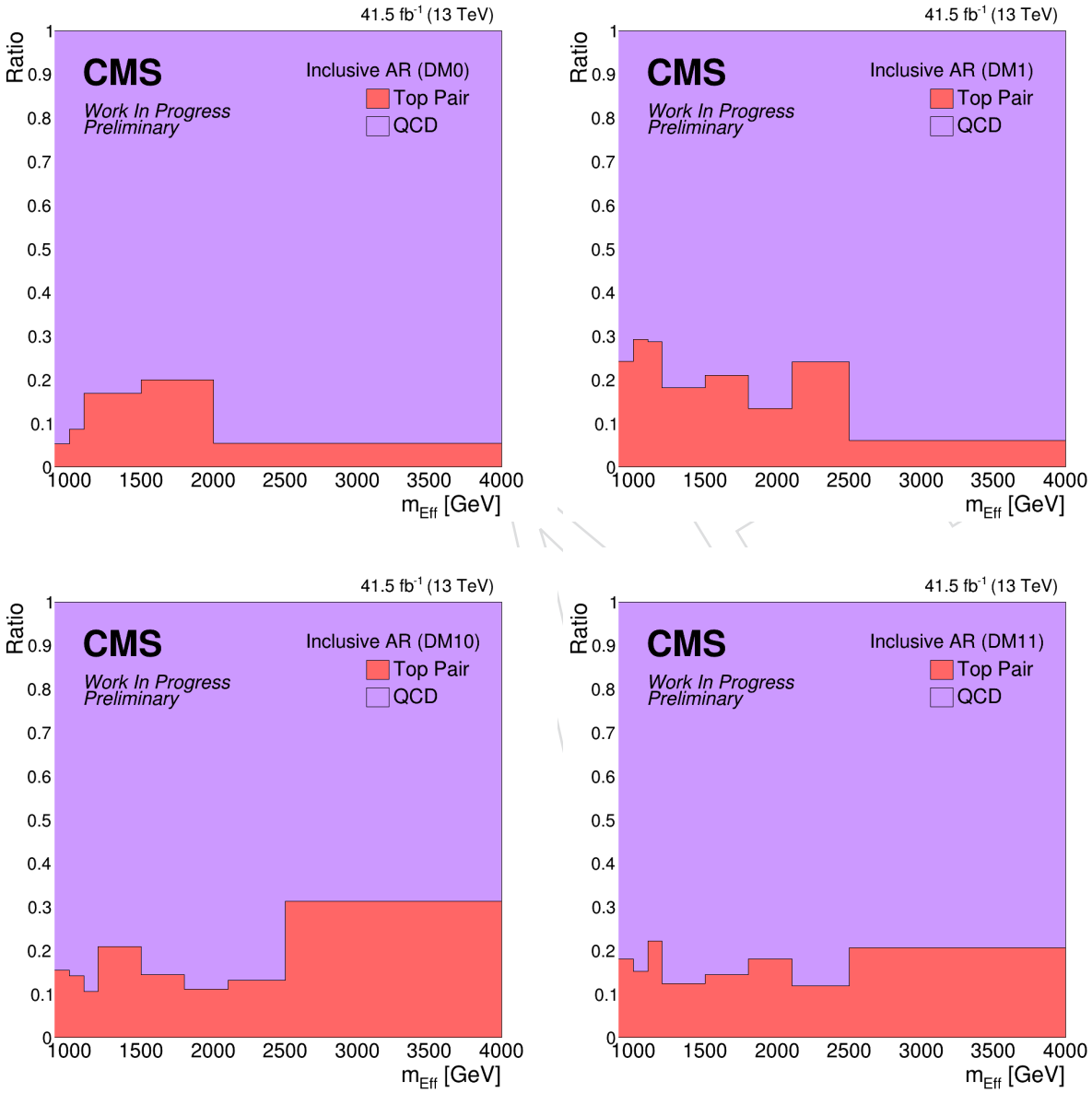

Figure 72: Fractions of the hadronic tau misidentification backgrounds as a function of m_{Eff}, divided by the hadronic tau decay modes used in this analysis in the Run2 UL 2017 era.

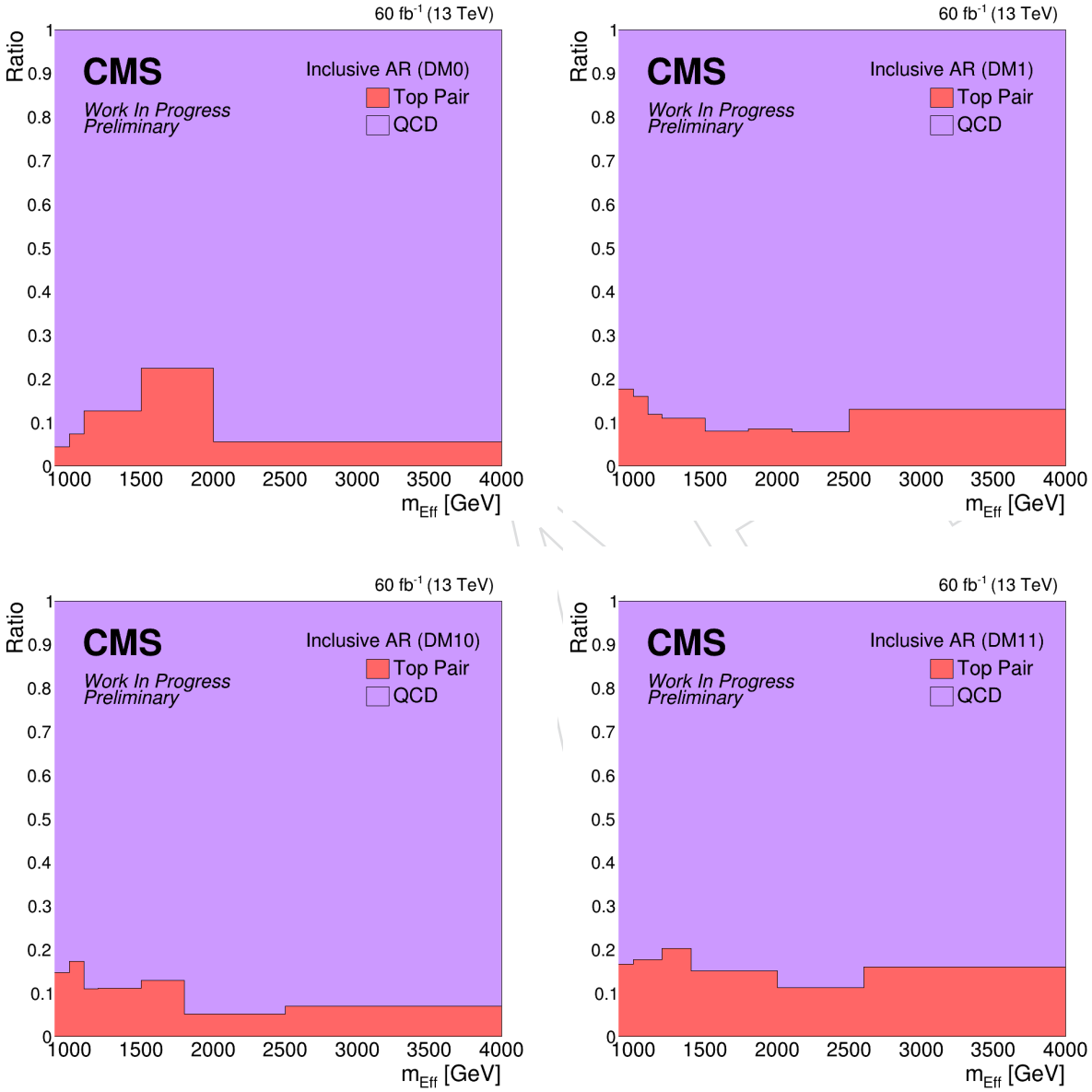

Figure 73: Fractions of the hadronic tau misidentification backgrounds as a function of m_{Eff}, divided by the hadronic tau decay modes used in this analysis in the Run2 UL 2018 era.

D.3.2 Low Mass CR Application Region (p_T)

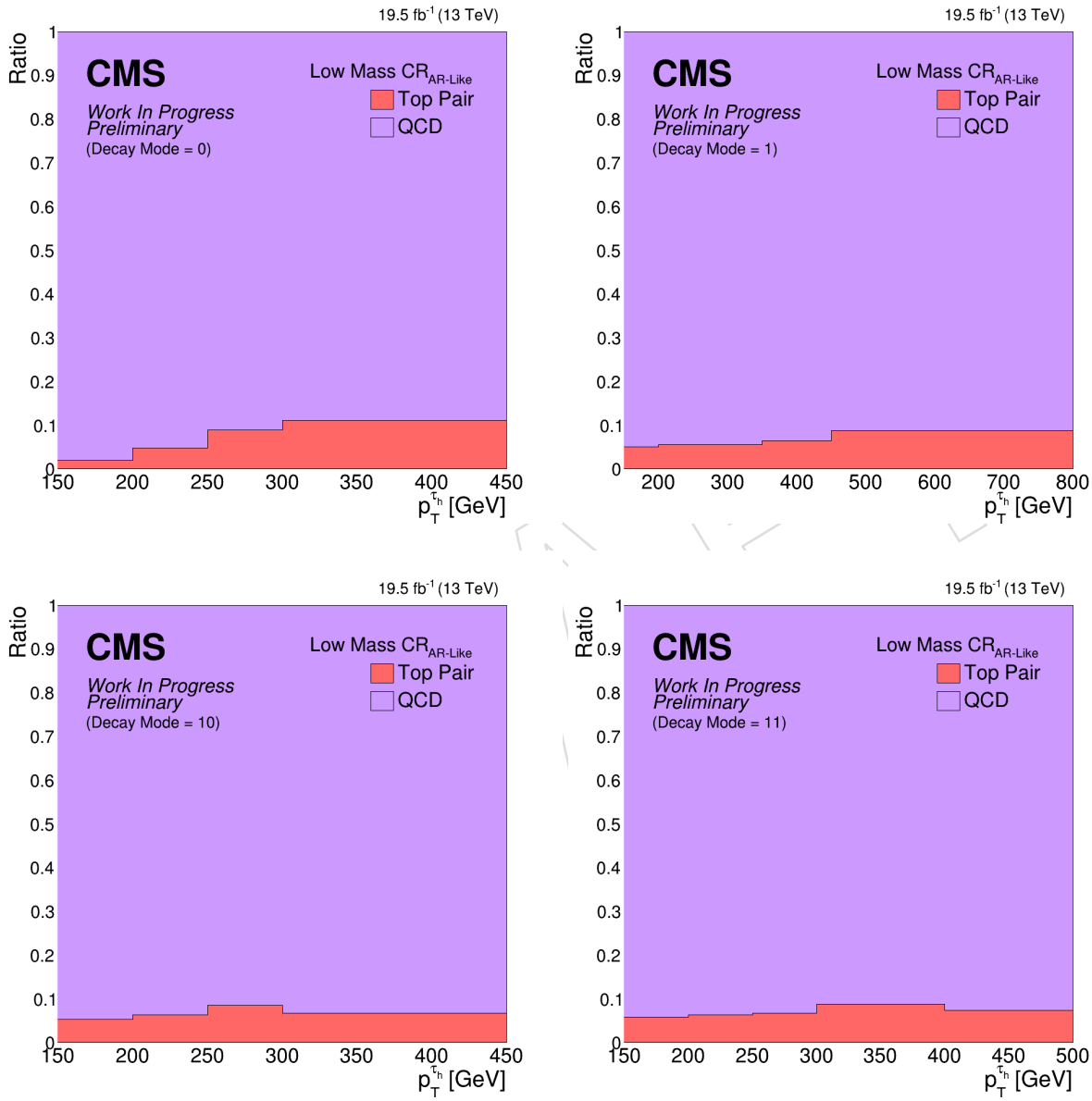

Figure 74: Fractions of the hadronic tau misidentification backgrounds in the low mass CR application region as a function of hadronic tau p_T, divided by the hadronic tau decay modes used in this analysis in the Run2 UL 2018 era.

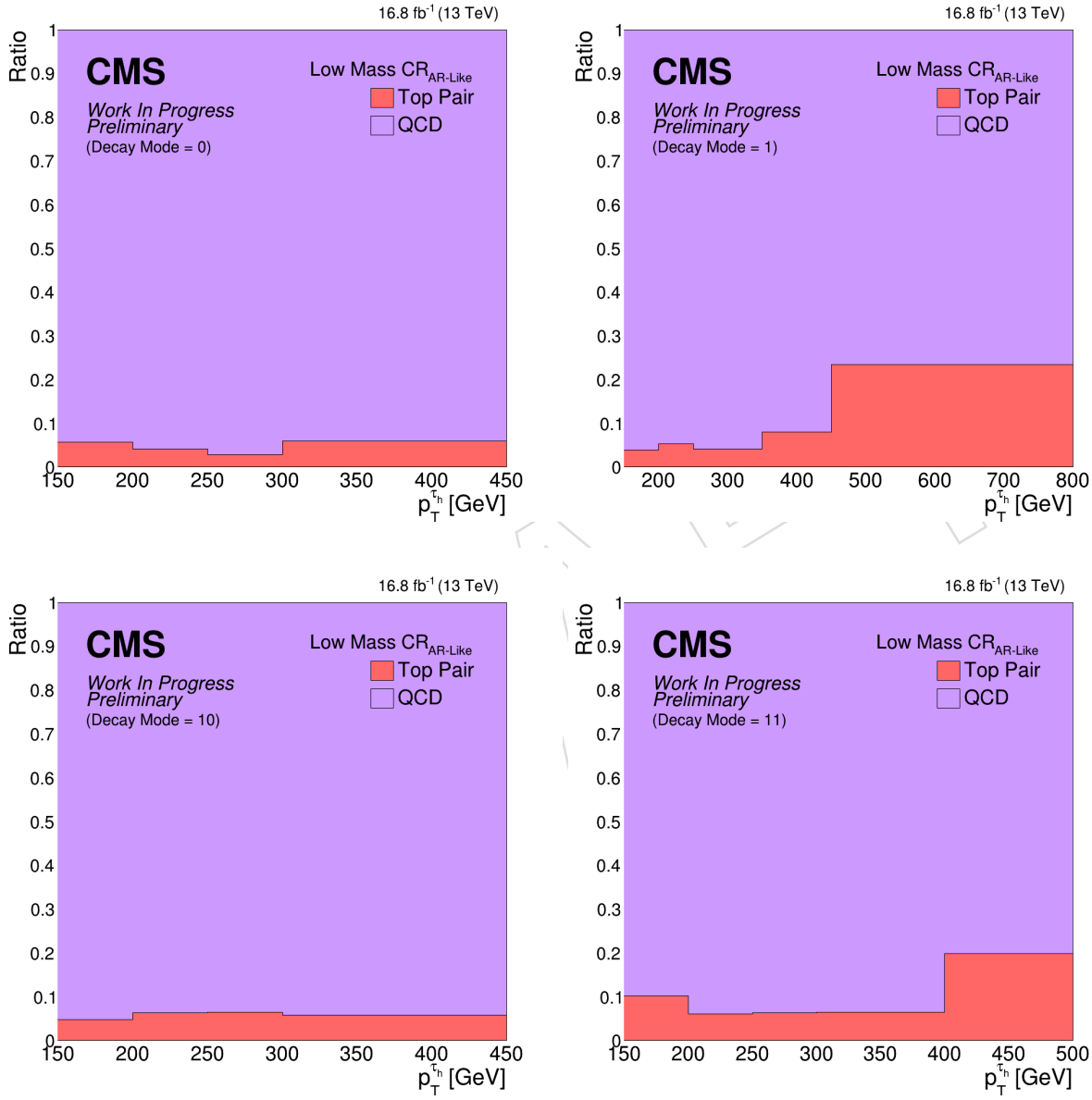

Figure 75: Fractions of the hadronic tau misidentification backgrounds in the low mass CR application region as a function of hadronic tau p_{T}, divided by the hadronic tau decay modes used in this analysis in the Run2 UL 2018 era.

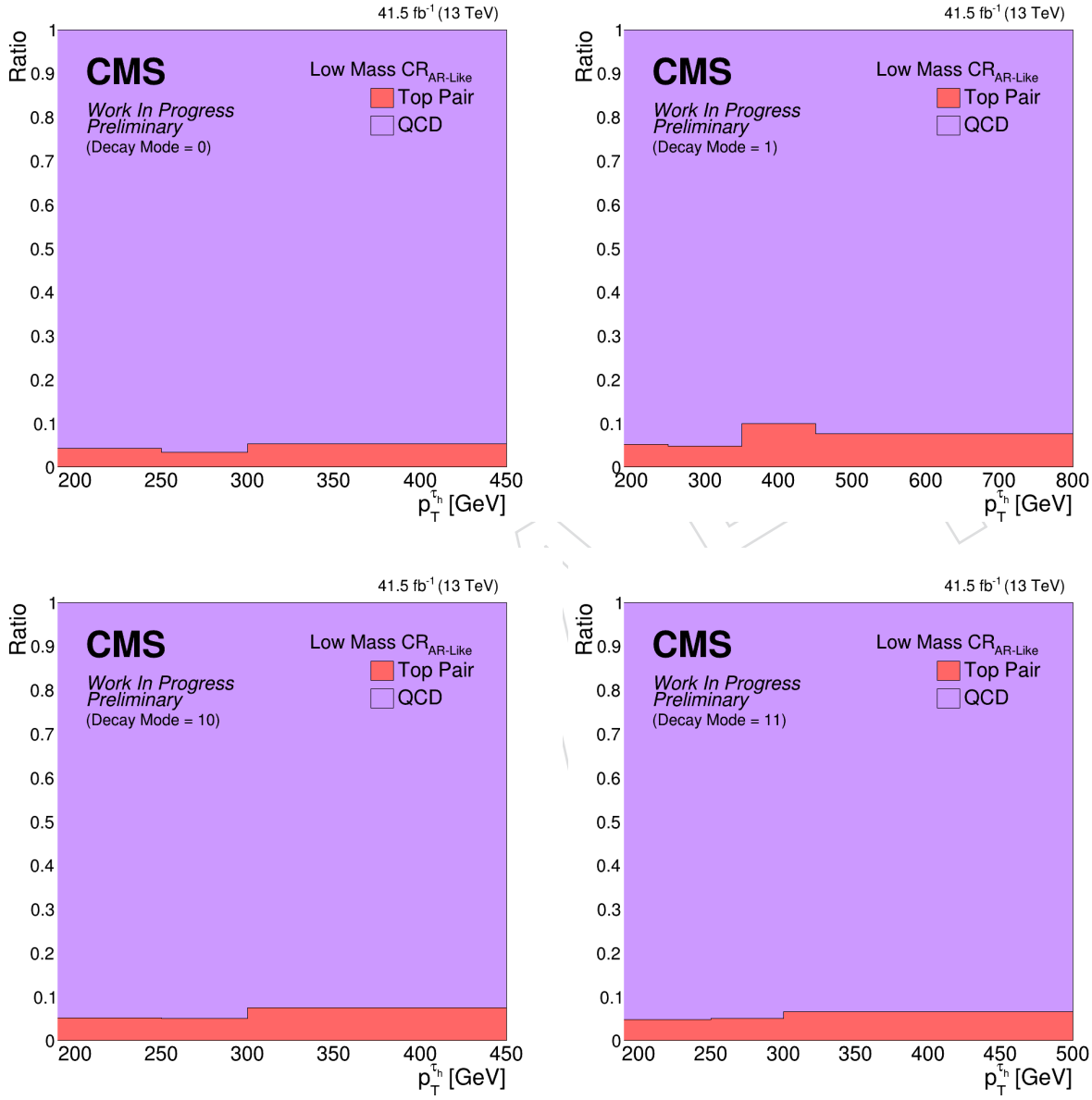

Figure 76: Fractions of the hadronic tau misidentification backgrounds in the low mass CR application region as a function of hadronic tau p_{T}, divided by the hadronic tau decay modes used in this analysis in the Run2 UL 2018 era.

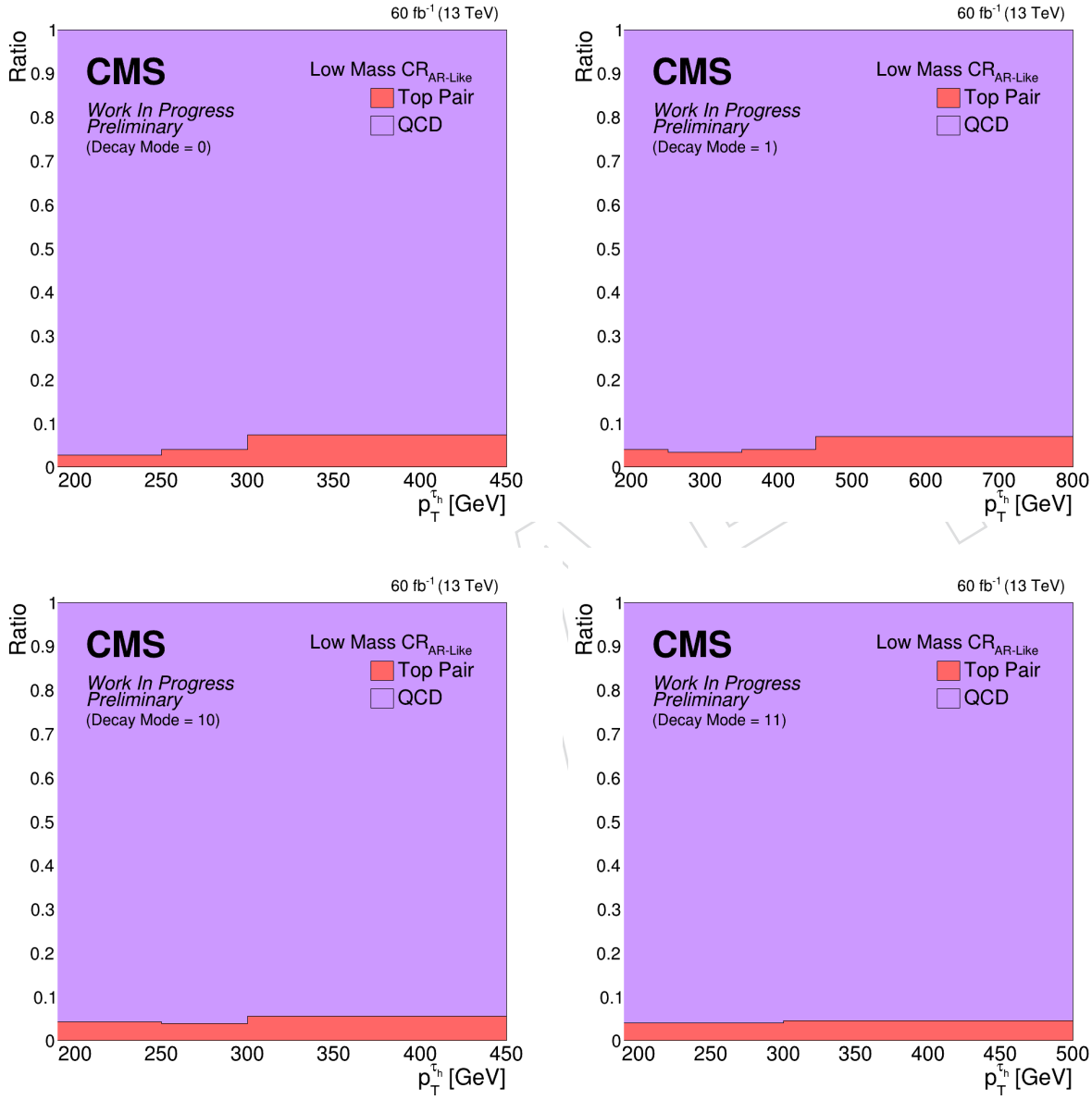

Figure 77: Fractions of the hadronic tau misidentification backgrounds in the low mass CR application region as a function of hadronic tau p_{T}, divided by the hadronic tau decay modes used in this analysis in the Run2 UL 2018 era.

D.3.3 Low Mass CR Application Region ($m_{Eff.}$)

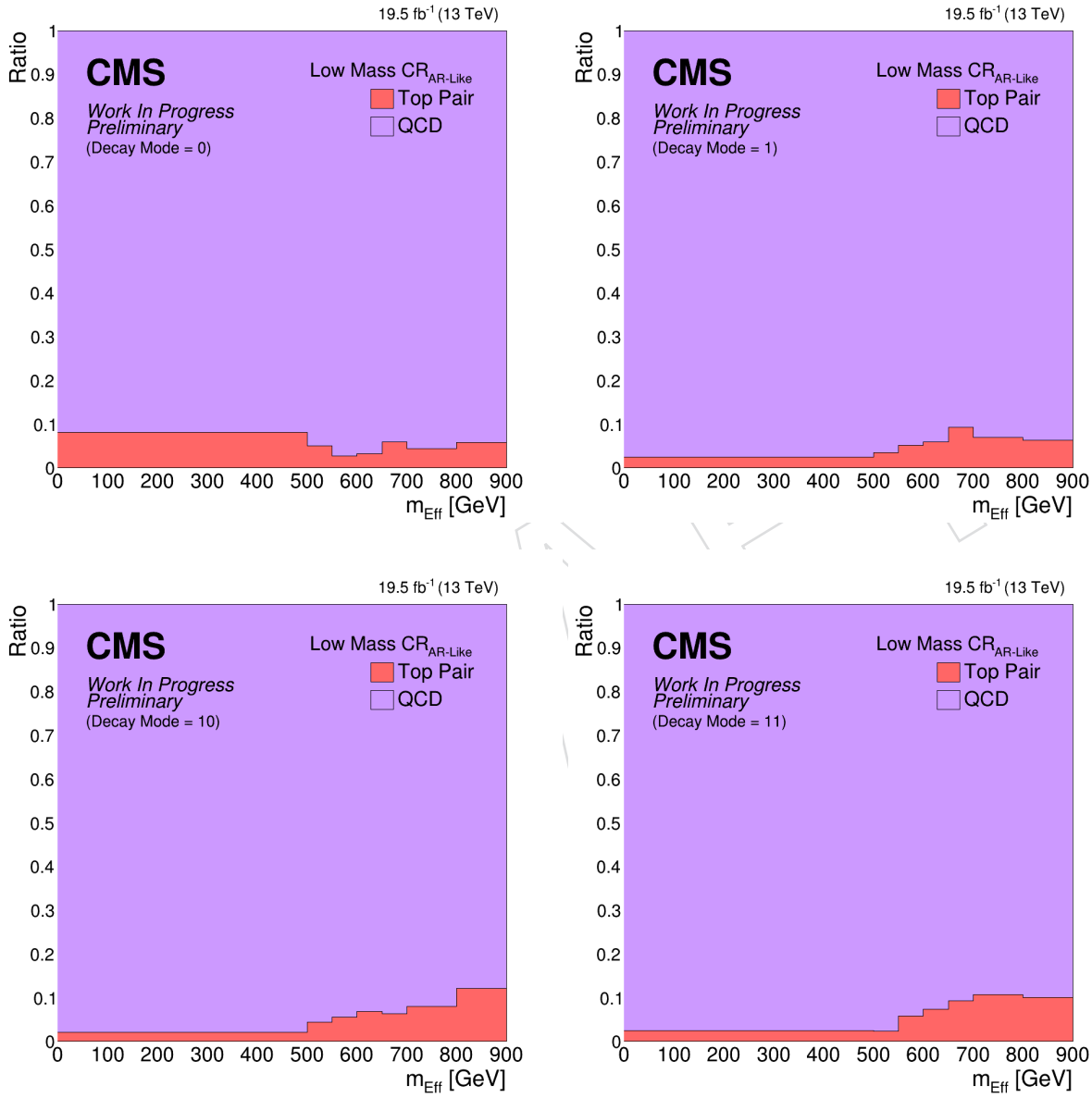

Figure 78: Fractions of the hadronic tau misidentification backgrounds in the low mass CR application region as a function of m_{Eff}, divided by the hadronic tau decay modes used in this analysis in the Run2 UL 2018 era.

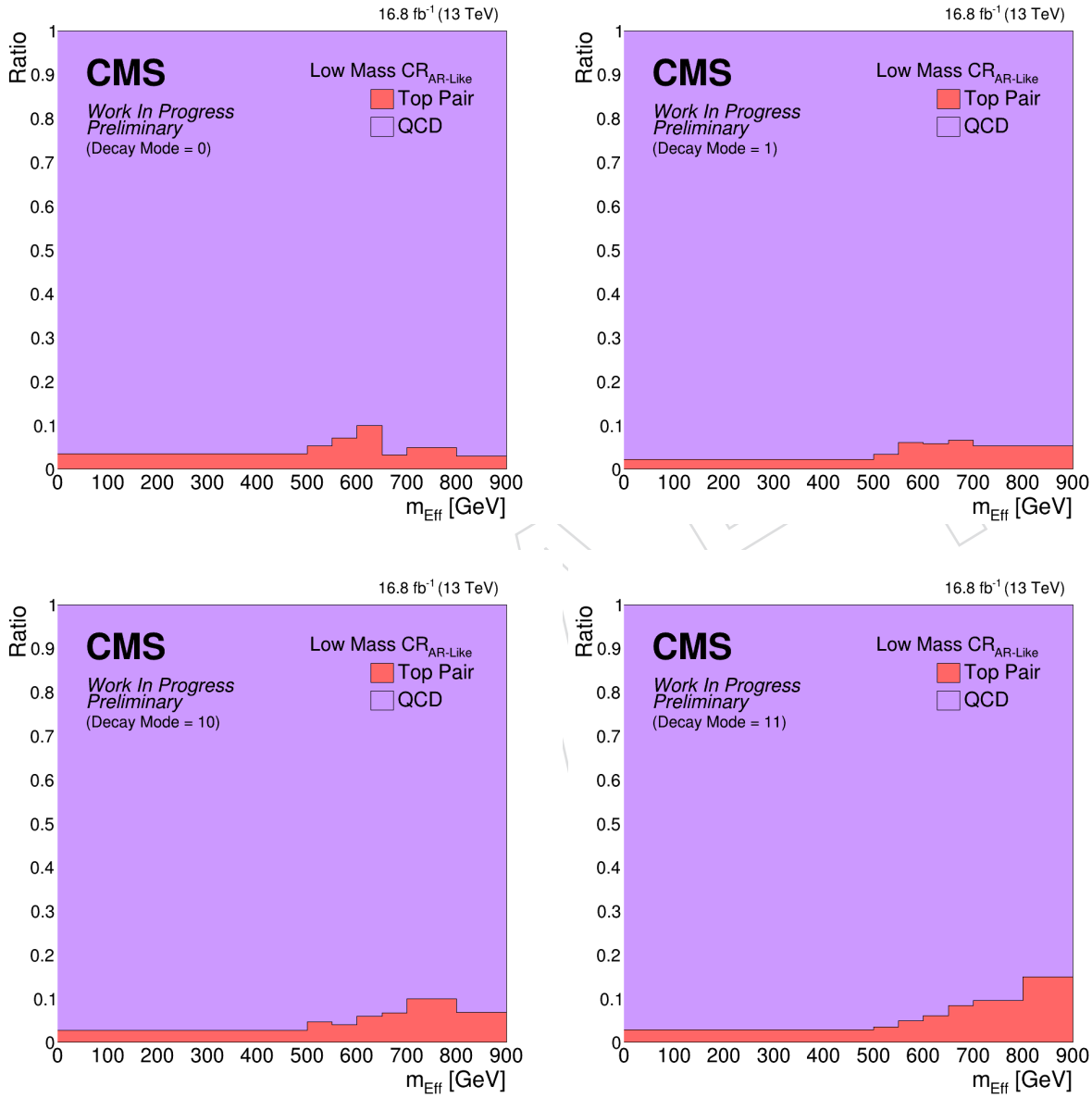

Figure 79: Fractions of the hadronic tau misidentification backgrounds in the low mass CR application region as a function of m_{Eff}, divided by the hadronic tau decay modes used in this analysis in the Run2 UL 2018 era.

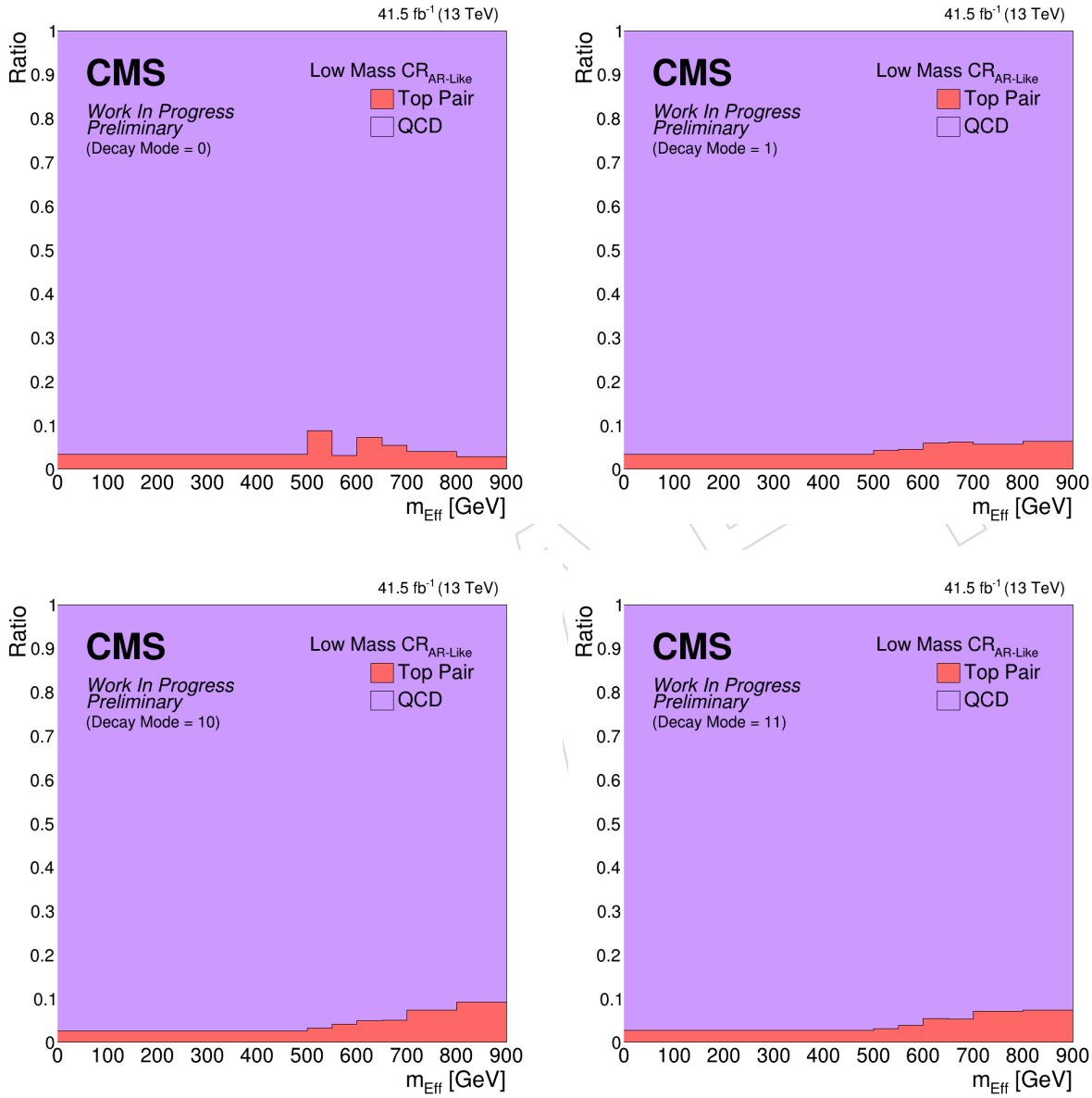

Figure 80: Fractions of the hadronic tau misidentification backgrounds in the low mass CR application region as a function of m_{Eff}, divided by the hadronic tau decay modes used in this analysis in the Run2 UL 2018 era.

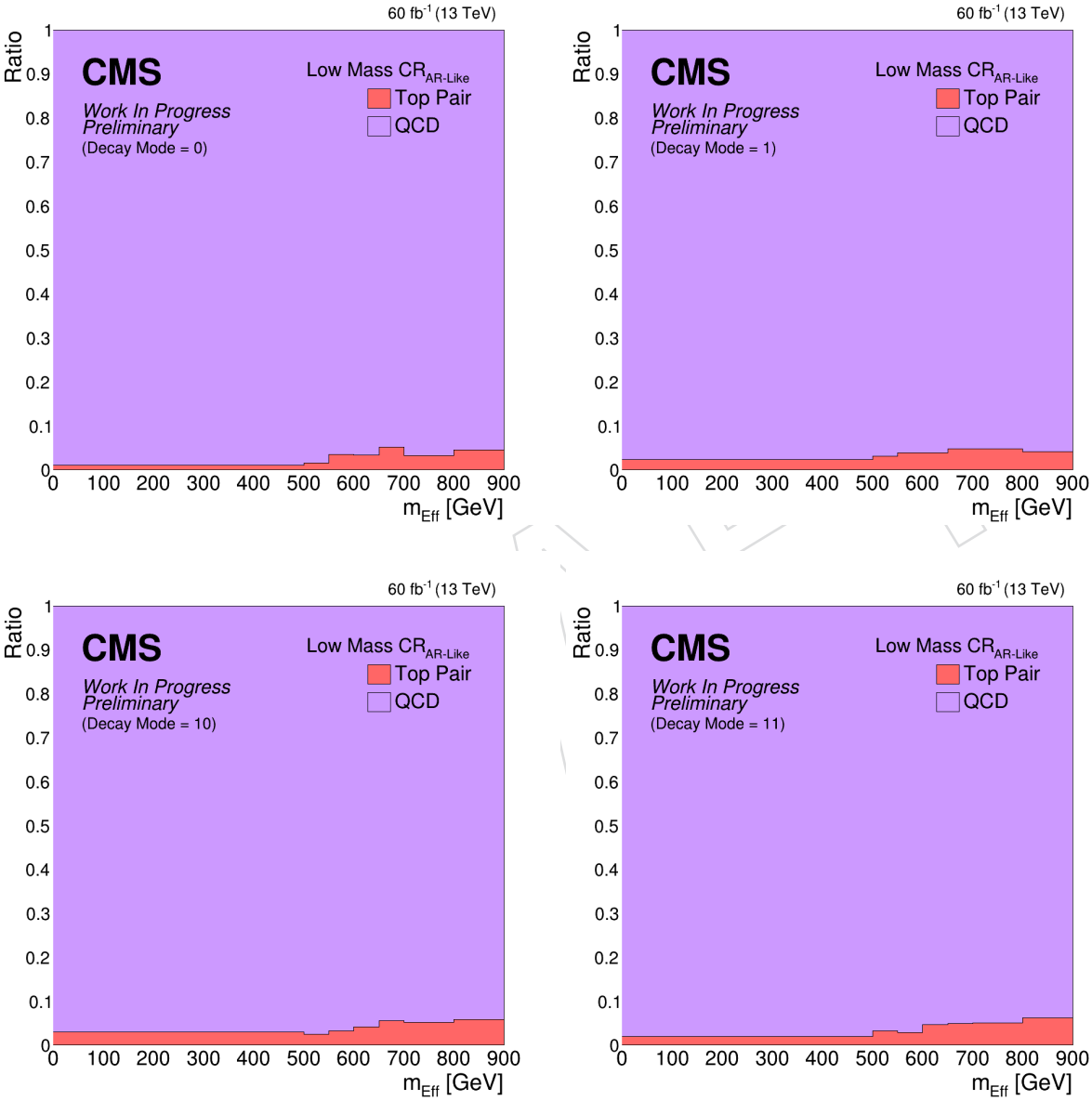

Figure 81: Fractions of the hadronic tau misidentification backgrounds in the low mass CR application region as a function of m_{Eff}, divided by the hadronic tau decay modes used in this analysis in the Run2 UL 2018 era.

References

[1] J. C. Pati and A. Salam, "Lepton number as the fourth "color"", *Physical Review D* **10** (July, 1974) 275–289, doi:10.1103/physrevd.10.275.

[2] R. N. Mohapatra and J. C. Pati, ""Natural" left-right symmetry", *Physical Review D* **11** (May, 1975) 2558–2561, doi:10.1103/physrevd.11.2558.

[3] G. Senjanovic and R. N. Mohapatra, "Exact left-right symmetry and spontaneous violation of parity", *Physical Review D* **12** (September, 1975) 1502–1505, doi:10.1103/physrevd.12.1502.

[4] W.-Y. Keung and G. Senjanović, "Majorana neutrinos and the production of the right-handed charged gauge boson", *Physical Review Letters* **50** (May, 1983) 1427–1430, doi:10.1103/physrevlett.50.1427.

[5] CMS Collaboration, "Search for heavy neutrinos and third-generation leptoquarks in hadronic states of two τ leptons and two jets in proton-proton collisions at $\sqrt{s} = 13$TeV ", *J. High Energy Phys.* **2019** no. 3,.

[6] J. Alwall et al., "The automated computation of tree-level and next-to-leading order differential cross sections, and their matching to parton shower simulations", doi:10.1007/JHEP07(2014)079, arXiv:1405.0301.

[7] O. Mattelaer, M. Mitra, and R. Ruiz, "Automated neutrino jet and top jet predictions at next-to-leading-order with parton shower matching in effective left-right symmetric models", 2016.

[8] T. Sjöstrand et al., "An Introduction to PYTHIA 8.2", doi:10.1016/j.cpc.2015.01.024, arXiv:1410.3012.

[9] CMS Collaboration, "Extraction and validation of a new set of CMS pythia8 tunes from underlying-event measurements", *Eur. Phys. J. C Part. Fields* doi:doi:10.1140/epjc/s10052-019-7499-4.

[10] R. D. Ball et al., "Unbiased global determination of parton distributions and their uncertainties at nnlo and at lo", *Nuclear Physics B* **855** (February, 2012) 153–221, doi:10.1016/j.nuclphysb.2011.09.024.

[11] R. D. Ball et al., "Parton distributions with qed corrections", *Nuclear Physics B* **877** (December, 2013) 290–320, doi:10.1016/j.nuclphysb.2013.10.010.

[12] R. D. Ball et al., "Parton distributions from high-precision collider data: Nnpdf collaboration", *The European Physical Journal C* **77** (October, 2017) doi:10.1140/epjc/s10052-017-5199-5.

[13] S. Agostinelli et al., "Geant4—a simulation toolkit", *Nuclear Instruments and Methods in Physics Research Section A: Accelerators, Spectrometers, Detectors and Associated Equipment* **506** (July, 2003) 250–303, doi:10.1016/s0168-9002(03)01368-8.

[14] CMS Collaboration, "Particle-flow reconstruction and global event description with the cms detector", *Journal of Instrumentation* **12** (October, 2017) P10003–P10003, doi:10.1088/1748-0221/12/10/p10003.

[15] CMS Collaboration, "Performance of the CMS muon detector and muon reconstruction with proton-proton collisions at $\sqrt{s} = 13$TeV", *JINST* **13** (June, 2018) P06015–P06015, doi:10.1088/1748-0221/13/06/p06015.

[16] CMS Collaboration, "Performance of the reconstruction and identification of high-momentum muons in proton-proton collisions at $\sqrt{s} = 13$TeV", *JINST* **15** (February, 2020) P02027–P02027, doi:10.1088/1748-0221/15/02/p02027.

[17] A. Khukhunaishvili and A. Bodek, "Rochester Correction". Accessed on March 27th, 2023. https://twiki.cern.ch/twiki/bin/viewauth/CMS/RochcorMuon.

[18] CMS Collaboration, MuonPOG, "High-p_T Muon References for Run-II". Accessed on March 27th, 2023. https://twiki.cern.ch/twiki/bin/viewauth/CMS/HighPtMuonReferenceRun2.

[19] CMS Collaboration, MuonPOG, "Muon Reference Selecion and Calibrations for Run-II". Accessed on March 27th, 2023. https://twiki.cern.ch/twiki/bin/viewauth/CMS/MuonReferenceSelectionAndCalibrationsRun2.

[20] CMS Collaboration, "EGamma POG Run 2 UL Recommendations". https://twiki.cern.ch/twiki/bin/view/CMS/EgammaUL2016To2018, 2024. [Online; accessed 9-September-2024].

[21] CMS Collaboration, "Cut Based Electron Identification Run2". https://twiki.cern.ch/twiki/bin/view/CMS/CutBasedElectronIdentificationRun2, 2024. [Online; accessed 9-September-2024].

[22] CMS Collaboration, "Reconstruction and identification of τ lepton decays to hadrons and ν_τ at CMS", *JINST* **11** (January, 2016) P01019–P01019, doi:10.1088/1748-0221/11/01/p01019.

[23] CMS Collaboration, "Identification of hadronic tau lepton decays using a deep neural network", *Journal of Instrumentation* **17** (July, 2022) P07023, doi:10.1088/1748-0221/17/07/p07023.

[24] M. Cacciari, G. P. Salam, and G. Soyez, "The anti-k_{T} jet clustering algorithm", *JHEP* **04** (2008) 063, doi:10.1088/1126-6708/2008/04/063, arXiv:0802.1189.

[25] CMS Collaboration, "Pileup mitigation at CMS in 13 TeV data", *JINST* **15** (September, 2020) P09018–P09018, doi:10.1088/1748-0221/15/09/p09018.

[26] C. Brust et al., "Identifying boosted new physics with non-isolated leptons", *Journal of High Energy Physics* **2015** (April, 2015) doi:10.1007/jhep04(2015)079.

[27] D. Bertolini, P. Harris, M. Low, and N. Tran, "Pileup per particle identification", *Journal of High Energy Physics* **2014** (October, 2014) doi:10.1007/jhep10(2014)059.

[28] CMS Collaboration, "HEEP ID Scale Factor for UL". https://twiki.cern.ch/twiki/bin/view/CMS/EgammaUL2016To2018, 2024. [Online; accessed 19-September-2024].

[29] CMS Collaboration, "Tau Trigger". https://twiki.cern.ch/twiki/bin/view/CMS/TauTrigger, 2024. [Online; accessed 9-September-2024].

[30] CMS Collaboration, "Recommended Jet Energy Corrections and Uncertainties For Data and MC". https://twiki.cern.ch/twiki/bin/view/CMS/JECDataMC, 2024. [Online; accessed 19-September-2024].

[31] J. Butterworth et al., "PDF4LHC recommendations for LHC Run II", *Journal of Physics G: Nuclear and Particle Physics* **43** (January, 2016) 023001, doi:10.1088/0954-3899/43/2/023001.

[32] CMS Collaboration, "The CMS statistical analysis and combination tool: COMBINE", 2024. arXiv:2404.06614. Submitted to *Comput. Softw. Big Sci.*